Hybrid Precast Wall Systems for Seismic Regions

June 2012

Brian J. Smith, Yahya C. Kurama, and Michael J. McGinnis

Report #NDSE-2012-01

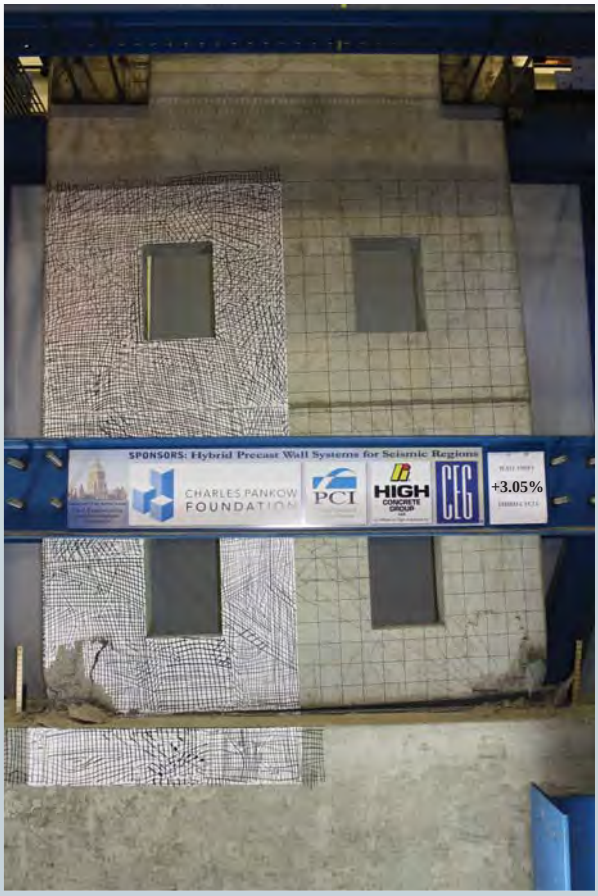

Specimen HW4

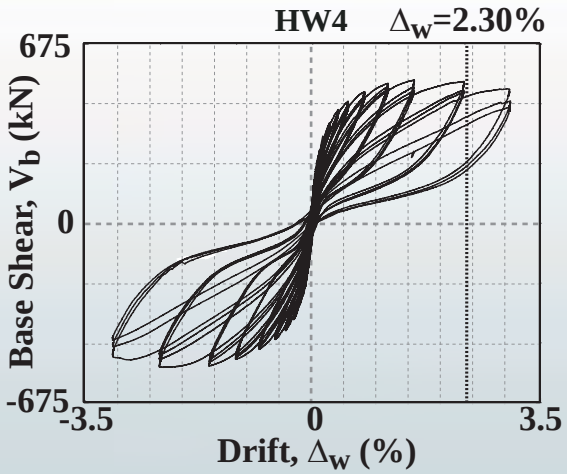

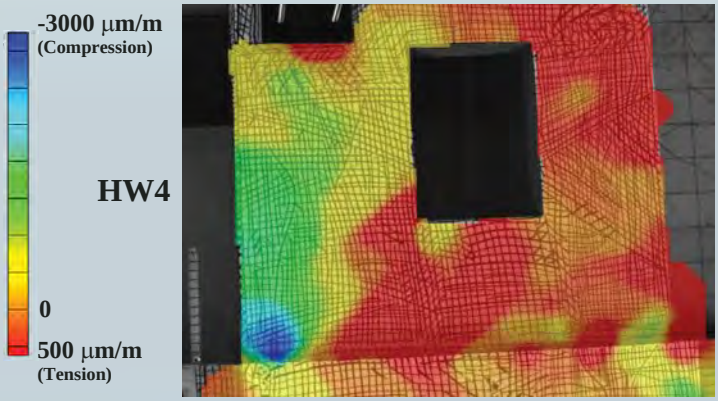

Structural Engineering Research Report

Department of Civil Engineering and Geological Sciences
University of Notre Dame
Notre Dame, Indiana

This page intentionally left blank.

Hybrid Precast Wall Systems for Seismic Regions

June 2012 Report #NDSE-2012-01

by

Brian J. Smith
Graduate Research Assistant
Yahya C. Kurama
Professor
University of Notre Dame

Michael J. McGinnis
Assistant Professor
University of Texas at Tyler

Structural Engineering Research Report

Department of Civil Engineering and Geological Sciences
University of Notre Dame
Notre Dame, Indiana

This page intentionally left blank.

TABLE OF CONTENTS

NOTATIONS

a_d = length of ACI 318 (2011) equivalent rectangular concrete compression stress block at Δ_{wd}

a_m = length of ACI ITG-5.2 (2009) equivalent rectangular concrete compression stress block at Δ_{wm}

A_{gross} = gross area of wall cross section (taken at section with perforations in case of perforated walls)

A_p = total post-tensioning (PT) steel area

A_s = total energy dissipating (E.D.) steel area

$A_{s,c}$ = area of horizontal or vertical chord reinforcement around panel perforations

A_{sh} = effective shear area of wall cross section

c = neutral axis length (i.e., contact length)

c_d = neutral axis length at base joint at Δ_{wd}

c_m = neutral axis length at base joint at Δ_{wm}

C_d = ASCE-7 (2010) deflection amplification factor

$\bar{C}_d$ = concrete compressive stress resultant at base joint at Δ_{wd}

$\bar{C}_m$ = concrete compressive stress resultant at base joint at Δ_{wm}

C_s = ASCE-7 (2010) seismic response coefficient

d_s = diameter of E.D. bar

e_p = distance of individual PT tendon from wall centerline

e_s = distance of individual E.D. bar from wall centerline

E_c = Young's modulus of unconfined concrete

$E_{c,td}$ = secant stiffness of unconfined concrete or grout at day of wall testing

E_w = measured secant stiffness of wall per ACI ITG-5.1 (2007)

E_{wi} = measured initial secant stiffness of wall at $0.75V_{wd}$ per ACI ITG-5.1 (2007)

$f_{c,u}$ = maximum concrete compression stress at upper panel joint at Δ_{wm}

f'_c = design compression strength of unconfined panel concrete

f'_{cc} = design compression strength of confined concrete at toes of base panel

$f'_{c,td}$ = maximum (peak) strength of unconfined concrete or grout at day of wall testing

$f'_{c,28d}$ = maximum (peak) strength of unconfined concrete or grout at 28 days

f_{hy} = yield strength of confinement hoop steel

f_{hu} = ultimate (maximum) strength of confinement hoop steel

$f_{p,loss}$ = PT stress loss in compression-side tendon due to nonlinear material behavior associated with repeated loading of wall to $\pm\Delta_{wm}$

f_{pd} = PT steel stress at Δ_{wd}

f_{pi} = initial stress of PT steel after all short-term and long-term losses (but before any lateral displacements of wall)

f_{pm} = PT steel stress at Δ_{wm}

f_{py} = yield strength of PT steel

f_{pu} = design ultimate strength of PT steel [1862-MPa (270-ksi)]

$f_{p@0.01}$ = stress in PT strand at 0.01-cm/cm [0.01-in./in.] strain based on monotonic material testing

f_{sd} = E.D. steel stress at Δ_{wd}
f_{sm} = E.D. steel stress at Δ_{wm}
f_{su} = ultimate (maximum) strength of E.D. (or mild) steel
f_{sy} = yield strength of E.D. (or mild) steel
h_{cr} = height at wall base over which tension strength of concrete fibers is taken as zero within fiber element model
h_{gap} = height used to determine rotation of wall due to gap opening in linear-elastic effective stiffness model
h_p = plastic hinge height over which plastic curvature is assumed to be uniformly distributed at wall base
H_{bp} = base panel height to top of foundation
H_w = wall height to top of foundation
I_e = reduced linear-elastic effective moment of inertia of wall cross section
I_{gap} = moment of inertia of wall base cross section in compression (i.e., contact region at base joint) in linear-elastic effective stiffness model
I_{gross} = moment of inertia of gross wall cross section (taken at section with perforations in case of perforated walls)
l_h = confined region length at wall toes (center-to-center of bar)
l_{hoop} = length of individual confinement hoop (center-to-center of bar)
l_{pu} = unbonded length of PT steel strand
l_{su} = total unbonded length of E.D. steel (i.e., wrapped length plus additional debonded length expected under cyclic loading of wall)
L_w = wall length
M_{wd} = wall design base moment at Δ_{wd}
M_{wm} = probable base moment strength of wall at Δ_{wm}
M_{wn} = contribution of wall gravity axial force, N_w to satisfy M_{wd}
M_{wp} = contribution of total PT steel force to satisfy M_{wd}
M_{ws} = contribution of total E.D. steel force to satisfy M_{wd}
N_{DL} = self-weight plus dead loads acting on wall [ACI ITG-5.2 (2009)]
N_w = design gravity axial force at wall base
R = response modification factor from ASCE-7 (2010)
s_{bot} = first confinement hoop distance from bottom of base panel (to center of bar)
s_h = confinement hoop spacing (center-to-center of bar)
t_w = wall thickness
T_c = total horizontal or vertical design tensile force in chord around panel perforations
V_b = measured base shear force
V_{bd} = measured base shear force at Δ_{wd}
V_{bm} = measured base shear force at Δ_{wm}
V_{wd} = design base shear force corresponding to M_{wd} at Δ_{wd}
V_{wm} = maximum base shear force corresponding to M_{wm} at Δ_{wm}
w_{hoop} = width of individual confinement hoop (center-to-center of bar)
z_d = distance between tension and compression stress resultants at base joint at Δ_{wd}
z_m = distance between tension and compression stress resultants at base joint at Δ_{wm}
α_s = ACI ITG-5.2 (2009) coefficient to estimate additional E.D. bar debonding that is expected to occur during reversed-cyclic lateral displacements of wall

β = relative energy dissipation ratio per ACI ITG-5.1 (2007)

β_1 = ACI 318 (2011) factor that relates c_d to length, a_d of equivalent rectangular concrete compression stress block at Δ_{wd}

β_m = ACI ITG-5.2 (2009) factor that relates c_m to length, a_m of equivalent rectangular concrete compression stress block at Δ_{wm}

δ_p = elongation of PT strand due to lateral displacement of wall

δ_s = elongation of E.D. bar due to lateral displacement of wall

δ_{we} = component of $\delta_{w,flex}$ due to linear-elastic flexural deformations over wall height

$\delta_{w,flex}$ = wall displacement due to flexural deformations in linear-elastic effective stiffness model

$\delta_{w,gap}$ = component of $\delta_{w,flex}$ due to gap opening at wall base

Δ_{bp} = base panel drift, defined as lateral displacement at top of base panel divided by height to top of foundation

Δ_w = wall drift, defined as lateral displacement at wall top divided by height to top of foundation

Δ_{wc} = typical minimum drift capacity of special unbonded post-tensioned precast concrete shear walls based on ACI ITG-5.1 (2007)

Δ_{wd} = design-level wall drift corresponding to Design-Basis Earthquake (DBE)

Δ_{we} = linear-elastic wall drift

Δ_{wm} = maximum-level wall drift corresponding to Maximum-Considered Earthquake (MCE)

$\varepsilon_{h,fr}$ = fracture strain of confinement hoop steel at $0.85f_{hu}$

ε_{hu} = strain of confinement hoop steel at f_{hu}

ε_{hy} = yield strain of confinement hoop steel at f_{hy}

$\varepsilon_{p,fr}$ = fracture strain of PT steel

ε_{pm} = strain in PT steel at Δ_{wm}

ε_{py} = yield strain of PT steel

ε_{sa} = allowable strain in E.D. steel at Δ_{wm}

ε_{sd} = strain in E.D. steel at Δ_{wd}

$\varepsilon_{s,fr}$ = fracture strain of E.D. steel at $0.85f_{su}$

ε_{sm} = strain in E.D. steel at Δ_{wm}

ε_{su} = strain of E.D. steel at f_{su}

ε_{sy} = yield strain of E.D. (or mild) steel at f_{sy}

γ = shear distortion angle of base panel

γ_m = ACI ITG-5.2 (2009) factor that relates stress of rectangular confined concrete compression block at toe of base panel to confined concrete strength, f'_{cc}

κ_d = E.D. steel moment ratio, defining relative amounts of energy dissipating resistance (from $A_s f_{sd}$) and restoring resistance (from $A_p f_{pd}$ and N_w) at wall base

ϕ = capacity reduction factor

$\phi_{f,u}$ = capacity reduction factor for axial-flexural design of upper panel-to-panel joints

ϕ_r = capacity reduction factor against loss of restoring

ϕ_s = capacity reduction factor for shear design

θ_{gap} = rotation of wall due to gap opening at base in linear-elastic effective stiffness model

μ_{ss} = coefficient of friction at horizontal joints

This page intentionally left blank.

ACKNOWLEDGEMENTS

This project was funded by the Charles Pankow Foundation and the Precast/Prestressed Concrete Institute (PCI). Additional technical and financial support was provided by the High Concrete Group, LLC, the Consulting Engineers Group, Inc., and the University of Notre Dame. The authors thank these organizations for supporting the project.

The authors gratefully acknowledge the guidance of the Project Advisory Panel in the conduct of the research. The members of this panel, who include Walt Korkosz (chair) - CEO of the Consulting Engineers Group, Inc., Ken Baur - former Director of Research and Development for the High Concrete Group, LLC, Dave Dieter - President of Mid-State Precast, LP, S.K. Ghosh - President of S.K. Ghosh Associates, Inc., and Neil Hawkins - Professor Emeritus at the University of Illinois at Urbana-Champaign, actively participated in the research and provided relevant recommendations for the successful completion of the project.

The authors would like to thank Robert Tener - Executive Director of the Charles Pankow Foundation, and Dean Browning - Project Director, for their guidance and direction. The authors also acknowledge the support of the PCI Research and Development (R&D) Committee, the PCI R&D Committee Chair, Harry Gleich, and the PCI Managing Director of Research and Development, Roger Becker.

The authors thank Phil Wiedemann - Executive Director of the PCI Central Region, and Wes Dees - former Midwest Regional Sales Manager of the High Concrete Group, LLC. This project would not have been possible without them.

Additionally, the authors thank Michael Lisk, undergraduate student at the University of Texas at Tyler, for monitoring the response of the precast concrete wall test specimens using three dimensional digital image correlation (3D-DIC). The 3D-DIC data provided unprecedented

full-field information on the behavior of the walls near the horizontal joints, compression toe regions, and around the perforations, thus supporting the code validation of the hybrid wall system.

Additional assistance and material donations were provided by Jenny Bass - President of Essve Tech Inc., Randy Ernest - Sales Associate at Prestress Supply Inc., Randy Draginis - Manager of Hayes Industries, Ltd., Rod Fuss - Manager of the Bourbonnais, IL plant for Ambassador Steel Corporation, Norris Hayes - President and CEO of Hayes Industries, Ltd., Chris Lagaden - Commercial Estimator for Ecco Manufacturing, Stan Landry - Product Manager for Enerpac Precision SURE-LOCK, Richard Lutz - Owner of Summit Engineered Products, Shane Whitacre - Area Sales Director for Dayton Superior Corporation, and Steve Yoshida - Chief Engineer for Sumiden Wire Products Corporation. The authors thank these companies and individuals for supporting this project.

Any opinions, findings, conclusions, and/or recommendations expressed in this document are those of the authors and do not necessarily represent the views of the individuals or organizations acknowledged above.

ABSTRACT

This document contains the final report for a research project entitled "*Hybrid Precast Wall Systems for Seismic Regions*" funded by the Charles Pankow Foundation and the Precast/Prestressed Concrete Institute. The report discusses the measured, analytical, and design behaviors of precast concrete panelized shear walls that use a combination of mild (i.e., U.S. Grade 60) steel and high-strength unbonded post-tensioning (PT) steel for lateral resistance across horizontal joints. During a large earthquake, gap opening at the base joint allows this new type of structural system to undergo large lateral displacements with reduced damage. Upon unloading, the PT steel provides a restoring force to close the gap and pull the wall back towards its undisplaced position, reducing the permanent lateral displacements. The mild steel crossing the base joint is designed to yield and provide energy dissipation. Both the PT steel and the mild steel [which is referred to as the "energy dissipating (E.D.)" steel in this document] contribute to the lateral strength of the wall, resulting in an efficient structure.

The most pressing U.S. market need related to hybrid precast walls is code validation subject to the requirements of the American Concrete Institute (ACI). In accordance with this need, the primary goal of this project was to develop the required experimental validation and the associated design and analytical studies for the classification of the hybrid system as "special" reinforced concrete shear walls for use in moderate and high seismic regions of the U.S. The project aimed to develop a structure with improved performance while utilizing practical construction details through the active guidance of a relevant industry advisory panel. The behavior from six 0.40-scale wall test specimens subjected to service-level gravity loads combined with reversed-cyclic lateral loading was investigated, including walls featuring multiple panels (i.e., multiple horizontal joints) and panel perforations, both common features in

practical building construction. The behavior of the specimens was measured using conventional data acquisition techniques as well as full-field 3D digital image correlation (a non-contact optical technique) of the wall panels and horizontal joints, providing unprecedented information on the wall performance and the effect of the perforations on the panel deformations.

The primary experimental variables included the placement and detailing of the E.D. steel bars crossing the base joint, relative areas of the E.D. and PT steel, concrete confinement details, and presence of perforations within the wall panels. The measured behaviors of the test specimens were compared against design predictions as well as analytical simulations created with a simple “design office” philosophy, focusing specifically on the ACI validation criteria. Ultimately, the results from this project demonstrate that the hybrid precast wall system can satisfy all the requirements for special reinforced concrete shear walls in seismic regions with improved performance, while also revealing important design, detailing, and analysis considerations to prevent undesirable failure mechanisms. A key deliverable from the project is a validated Design Procedure Document (Smith and Kurama 2012a) containing detailed seismic design guidelines and analysis tools for practicing engineers and precast concrete producers involved in the design of ACI-compliant hybrid shear walls with predictable and reliable behavior under earthquakes.

CHAPTER 1

INTRODUCTION

1.1 HYBRID PRECAST WALL SYSTEM

The hybrid precast concrete shear wall system investigated in this project, shown in Figure 1.1, is constructed by stacking rectangular precast wall panels along horizontal joints above the foundation and at the floor levels. Fiber-reinforced non-shrink dry-pack grout is used at these joints for the alignment/bearing of the wall panels and to allow for construction tolerances during erection. The term “hybrid” reflects that a combination of mild (i.e., U.S. Grade 60) reinforcing steel and high-strength unbonded post-tensioning (PT) steel is used for lateral resistance across the joints. The PT force is provided by multi-strand tendons placed inside ungrouted ducts (to prevent bond between the steel and concrete) through the wall panels and the foundation. Thus, the PT tendons are connected to the structure only at the end anchorages. The PT force, in combination with the gravity loads acting on the wall, provides the system with self-centering capability (i.e., the wall returns essentially to its undisplaced position after a large earthquake) while the mild steel bars crossing the base joint are designed to yield and dissipate energy, thus creating an efficient structure. To prevent significant gap opening at the upper panel-to-panel joints, a small amount of mild steel reinforcing bars, designed to remain linear-elastic with short unbonded lengths, are placed at the panel ends as shown in Figure 1.1.

Under the application of lateral loads into the nonlinear range, the primary mode of displacement in a well-designed hybrid precast shear wall occurs through gap opening at the horizontal joint between the base panel and the foundation (i.e., the base joint or base-panel-to-foundation joint). In comparison, the flexural and shear deformations of the wall panels do not contribute significantly to the lateral displacements of the structure. In other words, the wall

essentially behaves as a rigid body rotating above its foundation. This behavior results in reduced damage in the hybrid shear wall system than the damage that would be expected in a conventional monolithic cast-in-place reinforced concrete wall system at a similar lateral displacement.

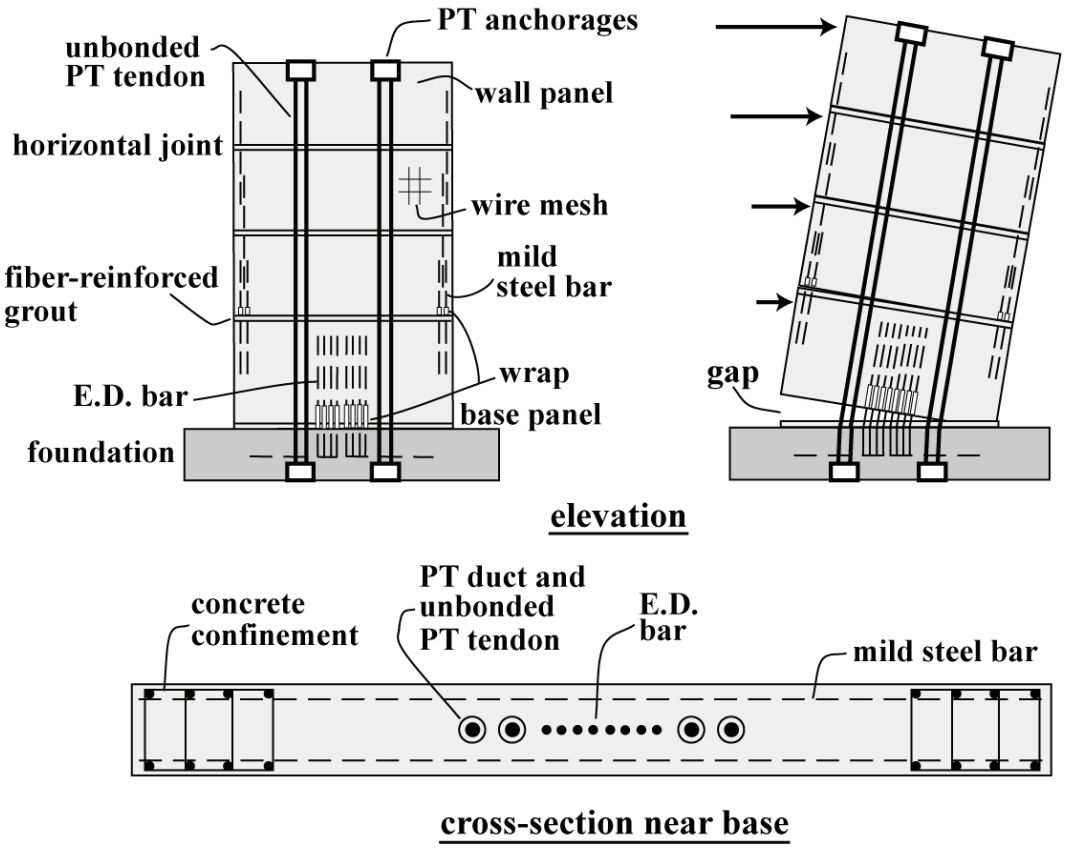

Figure 1.1 Elevation, Exaggerated Displaced Position, and Cross-Section of Hybrid Wall System

Upon unloading, the PT steel provides a vertical restoring force (in addition to the gravity loads acting on the wall) to close the gap at the base joint, thus significantly reducing the residual (i.e., permanent) lateral displacements of the structure after a large earthquake. The use of unbonded PT tendons reduces the strand strains as well as the tensile stresses transferred to the concrete as the tendons elongate under lateral loading (thus, preventing or delaying the yielding of the strands and reducing the cracking of the concrete in the wall panels). Further, the tendons

are placed near the centerline (i.e., mid-length) of the wall to minimize the strand elongations and to keep the tendons outside of the critical confined concrete regions at the wall toes.

The mild steel bars crossing the base joint, referred to as the energy dissipating (E.D.) steel in this document, are designed to yield in tension and compression, and provide energy dissipation through the gap opening/closing behavior of the wall under reversed-cyclic lateral loading. A pre-determined length of these bars is unbonded at the base joint (by wrapping the bars with plastic sleeves) to limit the steel strains and prevent low-cycle fatigue fracture. The E.D. bars should be designed and detailed to develop the maximum steel stresses and strains (including strain hardening) that are expected to occur during a large earthquake.

While the gap opening behavior designed at the base joint of hybrid precast walls leads to less concrete cracking than would occur in a conventional monolithic cast-in-place reinforced concrete shear wall, localized compression damage should be expected at the toes of the base panel (about which the wall rotates at the base). Under a large ground motion, the cover concrete at the wall toes will be damaged and possibly spall. This damage is deemed acceptable and should be repairable if necessary. However, excessive deterioration of the concrete is undesirable, and accordingly, confinement reinforcement in the form of closed hoops should be placed at the ends of the base panel to prevent compression failure of the core concrete. The grout placed at the base joint should also be made ductile by utilizing fibers within the grout mix design.

1.2 PROBLEM STATEMENT

Hybrid precast wall structures offer high quality production, relatively simple construction, and excellent seismic characteristics by providing self-centering to restore the building towards its original undisplaced position as well as energy dissipation to control the

lateral displacements during an earthquake. However, for seismic regions, Chapter 21 of ACI 318 (2011) specifies that "*a reinforced concrete structural system not satisfying the requirements of this chapter shall be permitted if it is demonstrated by experimental evidence and analysis that the proposed system will have strength and toughness equal to or exceeding those provided by a comparable monolithic reinforced concrete structure satisfying this chapter*." The hybrid wall system investigated in this research falls into this category of "non-emulative" structures that require experimental validation (i.e., it does not emulate the behavior of monolithic cast-in-place reinforced concrete structures); and thus, its use in practice has been severely limited.

The required ACI 318 code validation is the single most pressing market need for the adoption of hybrid precast concrete shear walls as primary lateral load resisting systems in the U.S. Overcoming this limitation would lift a major road-block and provide a major advance for building construction, with broad applicability in moderate and high seismic regions. The minimum experimental evidence that governs the code validation for hybrid walls as "special" reinforced concrete shear walls is specified in ACI ITG-5.1 (2007). Among the subjects covered in ACI ITG-5.1 are requirements for the design of the test specimens and their configurations, as well as requirements for testing, assessing, and reporting satisfactory performance.

While limited prior research (described in Chapter 2) has demonstrated the excellent behavior that can be obtained from hybrid shear wall structures, the previous tests were not necessarily conducted according to the validation guidelines in ACI ITG-5.1 and were for solid wall configurations using a single panel (i.e., single horizontal joint at the base-panel-to-foundation interface). Different from these previous studies, this project provides new information in accordance with and directly addressing the ACI ITG-5.1 validation requirements as well as information regarding the behavior and design of hybrid precast walls featuring

multiple wall panels (i.e., multiple horizontal joints) and panel perforations, both common features in practical building construction.

1.3 RESEARCH OBJECTIVES

The primary purpose of this project is to advance innovation in building design and construction by conducting the required experimental validation and the associated design and analytical studies for the code approval of hybrid precast concrete wall structures as special reinforced concrete shear walls according to the acceptance criteria in ACI ITG-5.1 (2007) and ACI 318 (2011). The project seeks to give practicing engineers and precast producers the background, knowledge, and tools needed to apply hybrid walls in seismic regions of the U.S. without the need to carry out additional approval studies. The specific project objectives are to develop:

(1) a high-performance precast concrete seismic shear wall system with practical construction details;

(2) a validated, practical seismic design procedure for the new system described in a Design Procedure Document (Smith and Kurama 2012a);

(3) validated, practical analytical models and design tools that can accurately predict performance;

(4) sufficient experimental and analytical evidence demonstrating the classification of the structure as a “special” reinforced concrete shear wall system per ACI 318; and

(5) practical seismic application and detailing guidelines and recommendations.

1.4 PROJECT SCOPE

This project specifically focused on the requirements for the validation of hybrid precast walls as special reinforced concrete shear walls per ACI 318 (2011). The primary objective was to experimentally and analytically validate hybrid wall structures with practical details according to the guidelines, prerequisites, and requirements in ACI ITG-5.1 (2007). In accordance with this objective, six 0.40-scale wall specimens were tested under quasi-static reversed cyclic lateral loading combined with gravity loads. The measured behavior of the walls, which featured multiple horizontal joints and walls with panel perforations, provided new information about the hybrid wall system and demonstrated the use of these structures as special reinforced concrete shear walls in high seismic regions. The research results also revealed important design and detailing considerations and validated the application guidelines outlined in this document. The study included pre-test and post-test analytical studies, resulting in the validation of the analytical models and tools as well.

The use of multiple precast wall panels in the test specimens allowed for the behavior at both the critical base-panel-to-foundation joint as well as the upper panel-to-panel joint to be assessed. The research sought a superior wall system that can not only provide an adequate amount of strength, ductility, stiffness, and energy dissipation under lateral loads, but one that can also provide self-centering to the structure and resist seismic loading with a reduced amount of damage. To provide a point of comparison for the performance of the hybrid walls, one of the test specimens was a precast structure designed to emulate monolithic cast-in-place reinforced concrete shear walls by utilizing only mild steel reinforcement across the horizontal joints.

Within the general guidance of the applicable specifications in ACI ITG-5.2 (2009), a seismic design procedure was developed for the hybrid wall system (Smith and Kurama 2012a). To validate this methodology, important design and detailing parameters were varied among the

six test specimens, including: (1) relative amounts of energy dissipating (E.D.) mild steel and PT steel reinforcement; (2) detailing of the E.D. steel reinforcement at the wall base; (3) concrete confinement detailing at the wall toes; and (4) presence of perforations within the wall panels. The behavior of the specimens was measured using conventional data acquisition techniques as well as full-field 3D digital image correlation (a non-contact optical technique) of the wall panels and horizontal joints, providing unprecedented information on the wall performance and the effect of the perforations on the panel deformations.

As required by ACI ITG-5.1, a pre-test analytical study was conducted to evaluate the design and expected performance of the test specimens based on nonlinear lateral load analyses. Two types of analytical models were constructed, one using fiber elements and the other with finite elements to represent the wall panels. These models also formed the basis for the post-test analyses of the specimens. Comparisons between the predicted and measured behaviors were used to validate and refine (as necessary) the analytical models after each test. In addition, the analyses of the test specimens provided information beyond what could be measured in the laboratory.

The experimental and analytical results were ultimately used to develop a validated Design Procedure Document (Smith and Kurama 2012a), which is a key deliverable from this project. The Design Procedure Document contains practical design and analysis guidelines and recommendations to be used by practicing engineers and precast concrete producers involved in the seismic design of hybrid walls. The recommendations include a performance-based design methodology as well as a prescriptive methodology applicable for both moderate and high seismic regions. Specific steps are provided to determine the PT and E.D. steel areas and strains, the confined concrete detailing at the wall toes, and the behavior at the base-panel-to-foundation and upper panel-to-panel joints (note that only the base joint is allowed to have significant gap

opening). Further, detailing specifications are given to ensure that the hybrid system can achieve the required lateral drift capacity and provide a sufficient amount of energy dissipation and self-centering capability while preventing undesirable failure mechanisms. The Design Procedure Document also presents three analytical models (a linear-elastic effective stiffness model, a simplified finite element model, and a detailed fiber element model) as validated tools for engineers to design hybrid walls with predictable and reliable behavior under earthquakes.

More information on the results from this project can be found in the following documents that have been published to date: McGinnis et al. 2012; Smith and Kurama 2009, 2010a,b, 2012a,b; and Smith et al. 2010, 2011a,b,c, 2012a,b,c.

1.5 RESEARCH SIGNIFICANCE

Concrete shear walls make up a large percentage of the lateral load resisting systems in building construction. This project provides research results for the required seismic validation of hybrid precast concrete shear walls with multiple panels as well as walls with panel perforations, which are both common features in U.S. building practice. The measured behavior of the test specimens provides new information since hybrid walls with multiple panels or with panel perforations have not been previously studied. These results facilitate the adoption of a superior precast concrete wall system by practicing engineers and precast producers as special reinforced concrete shear walls in moderate and high seismic regions of the U.S., with no need for additional code-approval studies, while also presenting important design, detailing, and analysis considerations to prevent undesirable failure mechanisms.

CHAPTER 2

BACKGROUND

This chapter presents background information relevant to this research project. First, an overview on the emergence of precast concrete structures for seismic regions is given and previous research on hybrid precast shear walls is described. Then, a summary of the current ACI requirements that govern the seismic validation of hybrid walls is provided.

2.1 EMERGENCE OF SEISMIC PRECAST CONCRETE STRUCTURAL SYSTEMS

Precast concrete buildings are comprised of prefabricated structural members that are joined or assembled together to create gravity and lateral load resisting systems. Precast construction techniques result in cost-effective structures that provide high quality production and rapid erection. Despite these advantages, as compared with monolithic cast-in-place reinforced concrete structural systems, the use of precast concrete shear walls and moment-resisting frames for lateral resistance in seismic regions of the U.S. has been limited. This is primarily due to the uncertainty about the performance of precast structures under earthquake loading, as well as a relatively small amount of research to support precast concrete seismic design and construction practices.

Since the early 1990s, researchers have been investigating the behavior and design of precast concrete structures subjected to seismic loading. Two distinct construction concepts have been studied, namely “emulative” and “non-emulative” precast structures. Emulative precast systems are designed and detailed such that their behavior under lateral loading is similar to the behavior of conventional monolithic cast-in-place reinforced concrete structures. Unlike these systems, the behavior of non-emulative precast concrete structures under lateral loads is

governed by the opening and closing of gaps at the joints between the precast members, resulting in distinctly different characteristics.

The hybrid shear wall system investigated in this research is a type of non-emulative precast structure. Earlier studies focused on fully post-tensioned walls with no E.D. steel reinforcement crossing the horizontal joints (Kurama et al. 1999a,b, 2002; Rahman and Restrepo 2000; Perez et al. 2003, 2007; Restrepo 2003). The biggest limitation for the use of fully post-tensioned walls in seismic regions is that the energy dissipation of these structures is very small; and thus, their lateral displacements during an earthquake can be considerably larger than the displacements of a comparable monolithic cast-in-place wall with the same lateral strength and stiffness. Therefore, a number of researchers have investigated the use of supplemental energy dissipaters, such as friction dampers, fluid dampers, and yielding dampers, to reduce the seismic displacements of fully post-tensioned precast walls (Perez et al. 2004a,b; Priestley et al. 1999; Kurama 2000, 2001; Ajrab et al. 2004).

Previous research on precast concrete shear walls featuring panel perforations is extremely limited. Mackertich and Aswad (1997) developed a linear-elastic finite element analytical model for precast walls with rectangular panel perforations. Using a nonlinear finite element model, Allen and Kurama (2002) investigated the design of rectangular perforations in fully post-tensioned walls under combined gravity and lateral loads. The research identified the critical regions of the wall panels around the perforations and proposed a methodology to design the reinforcement in these regions so that the perforations would not affect the seismic performance of the wall.

2.2 PREVIOUS RESEARCH ON HYBRID PRECAST CONCRETE SHEAR WALLS

As described in Chapter 1, in hybrid precast walls, energy dissipation is provided by the yielding of mild (E.D.) steel reinforcement crossing the wall-to-foundation joint. Previous experimental research on this type of wall includes three hybrid walls tested under quasi-static reversed-cyclic lateral loading in New Zealand as follows. Rahman and Restrepo (2000) tested two identical specimens, with the exception that gravity load was applied on one wall but not the other. An additional hybrid wall, which used steel-fiber reinforced concrete and carbon fiber PT tendons, was tested by Holden et al. (2001, 2003). This specimen had a faulty construction detail near the critical joint at the base and did not produce desirable results. However, one of the walls tested by Rahman and Restrepo (2000) showed excellent behavior, sustaining drifts in excess of ±3.0% while maintaining its lateral strength, energy dissipation, and ability to self-center. The observed damage after the test was limited to cover concrete spalling at the toes of the wall. The study concluded that hybrid precast walls can resist lateral loads with minimal structural damage during a major earthquake, with adequate energy dissipation and the absence of significant post-earthquake residual drifts.

The previous experimental studies on hybrid precast walls featured configurations using a single panel over the entire height of the structure; and therefore, the tests focused on the behavior at the base joint and did not explore the behavior at potential upper panel-to-panel joints in multi-panel systems. The specimens were solid walls and did not include any perforations within the panels, which are a common feature for utility and/or security purposes in U.S. building practice (e.g., in the case of a parking garage). Also, ACI code validation was not an objective of the previous experiments; and thus, the wall specimens were not necessarily designed and tested to satisfy the validation requirements prescribed in ACI ITG-5.1 (2007).

Additional experimental studies on building structures with solid hybrid precast shear walls are described in Fleischman et al. (2005a,b) and Nagae et al. (2011). The project described by Fleischman et al. (2005a,b) focused on the development of a seismic design methodology for precast concrete floor diaphragms. The research combined finite element analyses of diaphragms, full-scale component experiments, and shake-table tests of a half-scale three-story structure that featured hybrid walls with a single joint at the base. Nagae et al. (2011) tested two full-scale, four-story buildings on the NIED E-Defense shake table in Japan. One specimen utilized a conventional cast-in-place reinforced concrete structural system with shear walls and moment frames, and the other specimen utilized solid hybrid precast concrete shear walls (featuring multiple wall panels post-tensioned together across horizontal joints) and precast frames. The goal of the project was to develop comparative shake table data on the response of conventional and precast concrete structures over a spectrum of earthquake intensities, including near-collapse. While the experimental portions of both of these major research projects have been completed, detailed results from the studies have not yet been published.

The analytical study conducted as part of the project described in this document built upon previous research by Kurama (2002), which developed a model with fiber elements to represent the precast wall panels. The unbonded PT steel and the unbonded lengths of the E.D. bars were modeled with truss elements. Using this model, Kurama (2002) conducted a parametric study to investigate the seismic behavior of hybrid walls with varying amounts of E.D. and PT steel reinforcement. Based on nonlinear dynamic time-history analyses, it was shown that the yielding of the E.D. reinforcement results in a considerable reduction in the lateral displacements of the walls, with no significant effect on the self-centering capability. A subsequent study (Kurama 2005) proposed a seismic design approach for the hybrid wall system based on the analyses of two prototype walls designed for different seismic performance

objectives. Overall, these previous analytical studies revealed several important advantages of hybrid precast walls subjected to earthquake loading as compared to fully post-tensioned walls with no E.D. steel reinforcement.

2.3 REQUIRED DESIGN AND VALIDATION CRITERIA

Current U.S. building design codes and provisions permit only certain structural systems to be used in seismic regions. Specifically, Chapter 21 of ACI 318 (2011) states that "*a reinforced concrete structural system not satisfying the requirements of this chapter shall be permitted if it is demonstrated by experimental evidence and analysis that the proposed system will have strength and toughness equal to or exceeding those provided by a comparable monolithic reinforced concrete structure satisfying this chapter*." The hybrid precast concrete wall system investigated in this research does not fall within the "emulative" category, thus requiring experimental validation and analysis prior to its use in practice. The roadmap for the experimental testing and performance assessment of these types of structures is provided by ACI ITG-5.1 (2007), which lays out the minimum evidence needed for the classification of post-tensioned precast walls as special reinforced concrete shear walls based on ACI 318 and provides specific requirements regarding the design, testing, and performance acceptance of the specimens to be used in the validation.

With regards to seismic design, ACI ITG-5.1 requires the development of a pre-test design procedure for the walls prior to experimental testing. This design procedure shall account for the effects of material nonlinearity, deformations of members and connections, and the effects of reversed-cyclic loading. Furthermore, the procedure shall include a methodology to predict the wall lateral strength and stiffness as well as cover topics such as wall shear (i.e., diagonal tension) strength, shear slip strength at the horizontal joints, concrete confinement

detailing, and reinforcement strain limits. The design of the walls shall provide detailing specifications to ensure that the system can achieve the required lateral drift capacity and provide a sufficient amount of energy dissipation and self-centering capability while ensuring against undesirable failure mechanisms, which include the buckling of the reinforcement, failure of the confined boundary regions at the wall toes, excessive joint opening, excessive shear slip along the joints, panel shear failure, and other local or global instabilities.

In addition, the design procedure shall conform to the applicable recommendations and requirements of ACI ITG-5.2 (2009), which provides specific design guidelines with regards to: (1) nominal and probable flexural strength calculations, including calculations for the neutral axis length and the design of the confined concrete regions of the wall; (2) minimum allowable forces provided by the PT and E.D. steel reinforcement; (3) limiting values for the PT and E.D. steel strains, including calculations for the debonded length of the E.D. bars; (4) diagonal tension and horizontal shear slip strength calculations; and (5) limiting values for the wall lateral displacements used in design.

ACI ITG-5.1 also provides requirements for the design of the test setup and the global features of the test specimens. A few key requirements for the specimens include: (1) a minimum of two wall panels (in order to model a representative upper panel-to-panel joint as well as the base-panel-to-foundation joint) unless the prototype structure uses a single panel for the full height of the wall; (2) a minimum specimen length scale of one-third; (3) a minimum wall height-to-length aspect ratio of 0.5; and (4) the use of similar reinforcement details and representative building materials in the test specimens as in the full-scale prototype structure.

Requirements regarding the specimen loading procedure per ACI ITG-5.1 include the following: (1) each test specimen shall be subjected to a sequence of displacement-controlled loading cycles representative of the lateral drifts expected under an earthquake; (2) three fully-

reversed cycles shall be applied at each drift ratio; (3) the initial drift ratio applied shall be within the essentially linear-elastic response range for the specimen; and (4) testing shall continue with gradually increasing drift ratios (between 1.25 and 1.5 times the preceding set of cycles) until the drift ratio equals or exceeds the "validation-level" drift defined as:

$$\Delta_{wc} = 0.9\% \leq \left(\frac{H_w}{L_w}\right) 0.8\% + 0.5\% \leq 3.0\% \tag{2.1}$$

where, H_w is the height to the top of the wall and L_w is the length of the wall. The wall drift, Δ_w is defined as the lateral displacement at the top of the wall divided by the wall height, as shown in Figure 2.1. Note that while only the gap opening rotation at the wall base and the flexural deformations of the wall panels are shown in Figure 2.1, ACI ITG-5.1 requires that all lateral deformations and rotations of the specimen due to flexure, shear, and horizontal shear slip are included in the calculation for Δ_w.

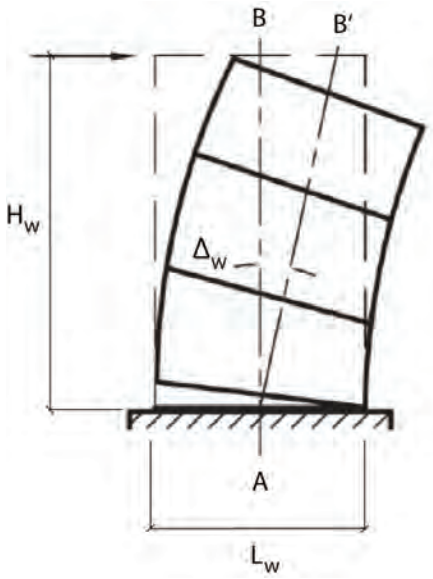

Figure 2.1 Definition of Wall Drift Angle, Δ_w (adopted from ACI ITG-5.1)

According to ACI ITG-5.1, the test specimen shall be considered to have performed satisfactorily when all of the following criteria are met for both directions of loading (i.e., positive and negative drift directions):

(1) The measured peak lateral strength is at least 0.90 times and not more than 1.20 times the predicted peak lateral strength using the pre-test design procedure.

(2) At a displacement of one-half the validation-level drift, the force in any PT tendon shall not exceed 0.90 times the measured PT tendon strength at 1% elongation.

(3) In cycling to the validation-level drift, for any sequence of three loading cycles to a peak drift angle greater than that achieved at the measured overall peak lateral strength of the structure, the measured peak lateral resistance for any of those three cycles shall not be less than 0.80 times the overall peak lateral strength in that particular loading direction (i.e., no more than 20% loss in peak lateral resistance during each set of three loading cycles beyond the overall peak lateral strength).

(4) For cycling at the validation-level drift, the relative energy dissipation ratio, β, for the 3rd drift cycle shall not be less than 0.125.

(5) For cycling at the validation-level drift, the secant stiffness between -1/10 and +1/10 times the maximum applied drift shall be not less than 0.10 times the initial lateral stiffness of the structure in each direction of loading.

(6) For cycling at the validation-level drift, the maximum relative horizontal slip (i.e., shear slip) across any horizontal joint of the wall shall not exceed 0.15-cm (0.06-in.).

More information on these requirements can be found in ACI ITG-5.1. As shown in Figure 2.2, ACI ITG-5.1 defines the relative energy dissipation ratio, β, as "*the ratio of the measured energy dissipated by the test module during reversing cyclic displacements between given measured drift angles to the maximum theoretical energy that can be dissipated for the same drift angles*." Some of the parameters related to the acceptance and unacceptable hysteric behavior of the structure are shown in Figures 2.3 and 2.4.

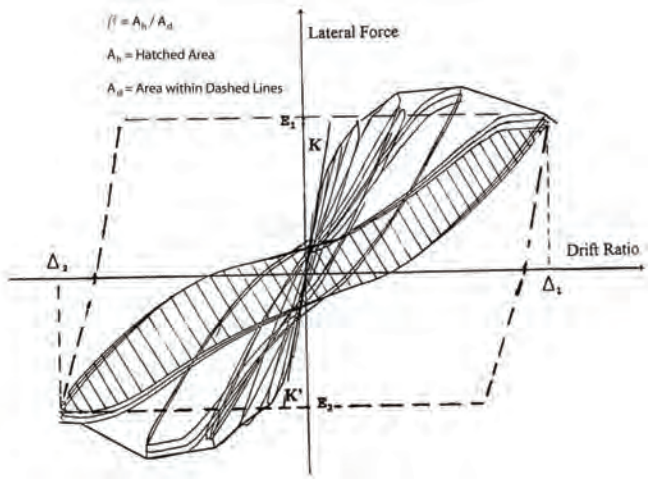

Figure 2.2 Relative Energy Dissipation Ratio, β (adopted from ACI ITG-5.1)

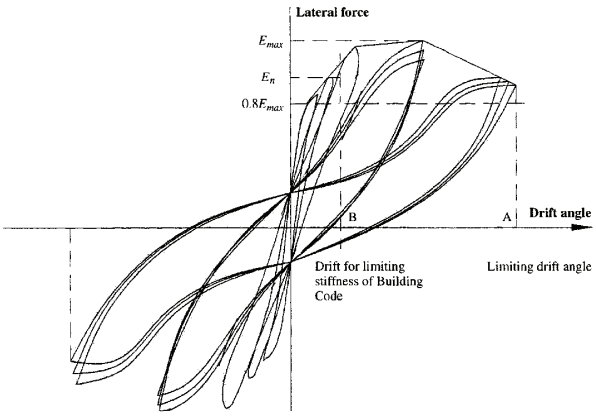

Figure 2.3 Acceptable Hysteretic Behavior (adopted from ACI ITG-5.1)

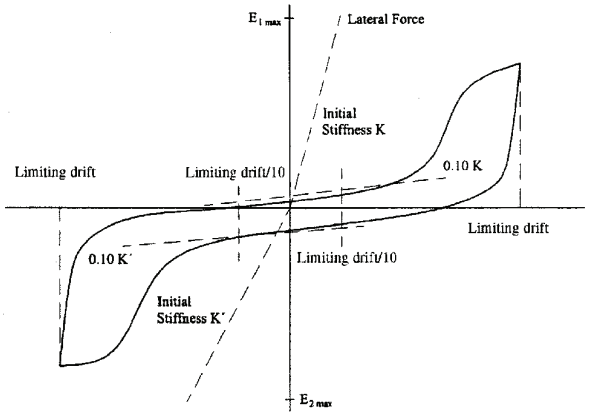

Figure 2.4 Unacceptable Hysteretic Behavior (adopted from ACI ITG-5.1)

This page intentionally left blank.

CHAPTER 3

DESIGN OF TEST SPECIMENS

This chapter provides an overview of the seismic design of the wall specimens tested in this research. Full details of the design, which conforms to both ACI 318 (2011) and ACI ITG-5.2 (2009), can be found in the Design Procedure Document (Smith and Kurama 2012a).

3.1 PROTOTYPE WALL AND TEST SPECIMEN DESIGN

The properties of the wall test specimens were determined based on a full-scale prototype structure designed in collaboration with the Consulting Engineers Group (CEG), Texas following the basic guidelines in ACI ITG-5.2 and ACI 318. The prototype building is a four-story regularly-shaped precast concrete parking garage [see Figure 3.1(a)] with an approximate footprint area of 3,770-m^2 (40,600-ft^2). The lateral load resistance of the building in the north-south direction is provided by seven hybrid precast concrete shear walls. Each wall is comprised of four precast wall panels over the four-story structure height (i.e., one wall panel for each story of the structure). One of the objectives of this research was to base the design of the test specimens on conventional methods to facilitate the rapid practical adoption of the hybrid system. In accordance with this objective, the equivalent lateral force procedure in ASCE 7 (2010) was used to determine the design base shear and moment demands for the walls.

From the prototype building plan, the hybrid walls located at the ends of the building were selected as the prototype wall [see Figure 3.1(b)] since these walls had the largest lateral force demand (due to accidental torsion) while also having a significant tributary gravity load (due to the off-center placement of the adjacent gravity column). Using the equivalent lateral force procedure (per ASCE 7), the full-scale design base moment demand for the exterior walls

was determined as M_{wd}=27,120-kN-m (20,000-kip-ft). In this calculation, the structure was designed for a site in Los Angeles, California, where the seismic response coefficient for the building was determined to be C_s=0.182. A response modification factor of R=6.0 for special reinforced concrete shear walls within a building frame system (as defined by ASCE 7) was used in determining M_{wd}.

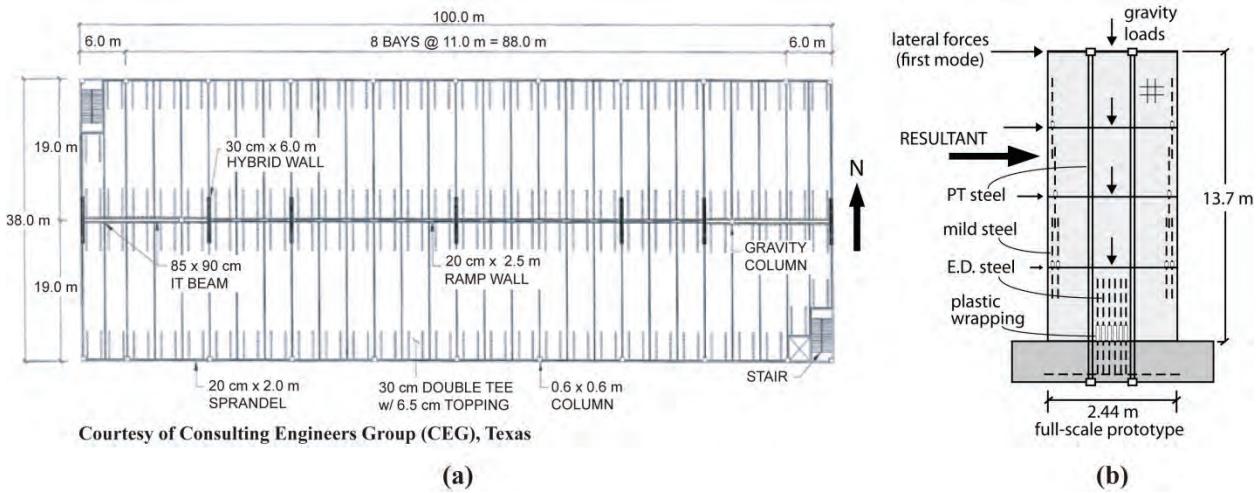

Figure 3.1 Full-Scale Prototype Structure: (a) Building Plan; (b) Wall Elevation

Applicable ACI ITG-5.2 guidelines were used in the design of the prototype hybrid wall. For axial-flexural behavior, the structure was intentionally designed not to have any significant over-capacity (neither in force nor displacement) beyond the minimum requirements of ACI ITG-5.2 and ACI 318. This decision was made in an effort to determine if the procedures and requirements used in the design of the wall were overly conservative, not conservative enough, or reasonable. Accordingly, no capacity reduction factor (i.e., ϕ factor) was used in the axial-flexural design of the critical wall base to test the limits of the design procedure.

3.1.1 Lateral Drift Demands

As shown in Figure 2.1, the wall drift, Δ_w is defined as the lateral displacement at the top of the wall divided by the wall height, H_w. All lateral deformations and rotations of the structure due to flexure, shear, horizontal shear slip, and gap opening (including any gap opening at the upper panel-to-panel joints) are included in Δ_w. However, since the design of a hybrid wall includes provisions to prevent significant shear slip across the horizontal joints and gap opening across the upper joints, these displacement components were taken as zero in the design of the prototype wall.

The design was conducted at two levels of drift: (1) the design-level drift, Δ_{wd}; and (2) the maximum-level drift, Δ_{wm}. The design-level drift was determined based on ASCE 7 as Δ_{wd}=0.62% for the solid walls. In the calculation of Δ_{wd}, a displacement amplification factor of C_d=5.0 for special reinforced concrete shear walls was applied to the linear-elastic drift of the walls, Δ_{we}=0.12% (flexural plus shear displacements corresponding to M_{wd}). As described in Section 5.1, an assumed effective shear area of A_{sh}=0.8A_{gross} and an assumed effective moment of inertia of I_e=0.5I_{gross} (with the 0.5 factor representing the reduction in the flexural stiffness of the wall due to gap opening over approximately 82.5% of the wall length at the base) were used in the estimation of Δ_{we} for the solid walls. The calculation of A_{sh} and I_e for the perforated walls is also described in Section 5.1. Note that when using the measured concrete strength, f_c', of the test specimens (as opposed to the design strength), the linear-elastic and design-level drifts changed slightly because of changes in the concrete Young's modulus, E_c.

The maximum-level wall drift, Δ_{wm} used in design was taken equal to the validation-level drift, Δ_{wc} (i.e., the drift level at which validation is sought per ACI ITG-5.1) using Eqn. 2.1. For the selected full-scale wall dimensions of L_w=6.1-m (20-ft) and H_w=13.7-m (45-ft),

where the 1st story height was 3.66-m (12-ft) and the upper story heights were 3.35-m (11-ft) each, the resulting wall height-to-length aspect ratio was 2.25. Therefore, the validation-level drift from Eqn. 2.1 was Δ_{wc}=2.30%; and thus, Δ_{wm}=2.30%.

3.1.2 Design of Test Specimens

The procedure used to design the test specimens included specific steps to determine the PT and E.D. steel areas and strains, the confined concrete detailing at the wall toes, and the behavior at the base-panel-to-foundation and upper panel-to-panel joints (note that only the base joint was allowed to have significant gap opening). Full details of this procedure as well as a full-scale design example can be found in the Design Procedure Document (Smith and Kurama 2012a); and thus, only an overview is provided herein.

The design of the test specimens was conducted at 0.40-scale using the measured steel material properties (to reduce over-strength in the structures). The PT and E.D. steel areas were determined to satisfy the wall design base moment demand, M_{wd}, at the design-level drift, Δ_{wd}. To determine the required steel areas, the "E.D. steel moment ratio," κ_d was selected. This ratio is defined as:

$$\kappa_d = \frac{M_{ws}}{M_{wp} + M_{wn}} \tag{3.1}$$

where, M_{ws}, M_{wp}, and M_{wn} represent the contributions of the E.D. steel, PT steel, and wall factored design gravity axial load, N_w, respectively, to satisfy the design base moment demand, M_{wd}. As described in Kurama (2005), the κ_d ratio measures the relative amounts of the energy dissipating force (from the E.D. steel reinforcement) and the vertical restoring (i.e., self-centering) force (from the PT steel reinforcement and the gravity axial load) in the wall. If κ_d is too small, the energy dissipation of the wall may be very small. Conversely, if κ_d is too large, the

self-centering capability of the wall may not be sufficient to yield the tensile E.D. bars back in compression and close the gap at the base joint upon unloading. The κ_d ratios used in the design of the test specimens in this project ranged from 0.50 to 0.85, with the actual κ_d ratios for the as-tested structures (using the provided steel areas) ranging from 0.50 to 0.90. Based on the measured performance of the walls, the Design Procedure Document provides a recommendation for selecting the design κ_d ratio between 0.50 and 0.80. Note the recommended lower limit of κ_d=0.50 was based on the performance of a perforated test specimen. As discussed in Section 8.2.1, it may be possible to use a reduced value for the lower κ_d limit of solid hybrid walls; however, this was not investigated in the project.

After selecting the design κ_d ratio, the required E.D. steel area, A_s, and PT steel area, A_p, as well as the neutral axis length, c_d, at Δ_{wd} were determined using equilibrium [as shown in Figure 3.2(a)]. As described in the Design Procedure Document, this process required iteration by assuming an initial value for the neutral axis length, c_d, to determine the E.D. steel and PT steel strains and stresses, ε_{sd}, f_{sd}, ε_{pd}, and f_{pd} using kinematics (described later), measured steel stress-strain relationships, and selected unbonded lengths. An initial value of c_d=0.175L_w was used as the starting point for the iteration. Note that for simplicity, Figure 3.2 shows equal PT steel stresses and equal E.D. steel stresses on the "compression-side" and "tension-side" of the wall centerline; however, the different stresses in the individual tendons and bars were incorporated in the design of each structure. The iteration was completed when the calculated c_d from equilibrium was sufficiently close to the value used at the beginning of the step. No capacity reduction factor was used in the determination of A_s and A_p. The concrete in compression was represented by the equivalent rectangular stress block from ACI 318.

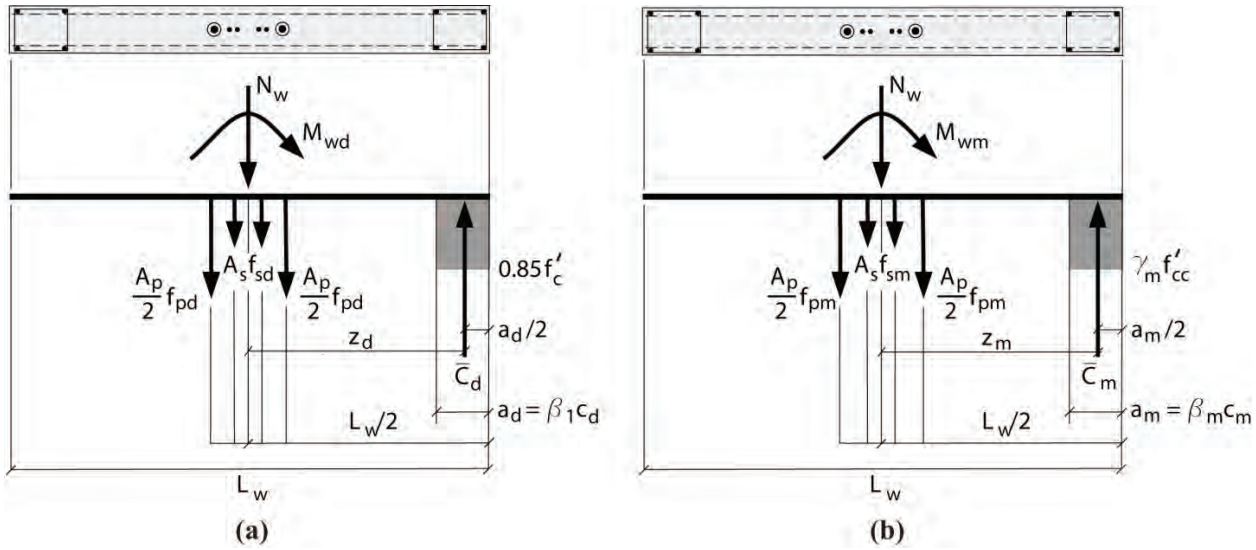

Figure 3.2 Simplified Force Diagram at Base-Panel-to-Foundation Joint: (a) at Δ_{wd}; (b) at Δ_{wm}

Upon determining A_p and A_s, the probable base moment strength of the wall, M_{wm}, was calculated using equilibrium considering material strain hardening at the maximum-level drift, Δ_{wm} [see Figure 3.2(b)]. As described in the Design Procedure Document, this process also required iterative steps with an assumed neutral axis length, c_m at Δ_{wm}, and the resulting confined concrete, E.D. steel, and PT steel strains and stresses, f'_{cc}, ε_{sm}, f_{sm}, ε_{pm}, and f_{pm}. As a starting point for the iteration, c_m=0.9c_d was selected and the process was repeated until the calculated c_m from the axial force equilibrium at the wall base was sufficiently close to the assumed c_m value. The confined concrete in compression was represented by a modified rectangular stress block per ACI ITG-5.2, with the confinement steel placed at the ends of the base panel to prevent premature crushing and failure of the concrete prior to Δ_{wm}. The confined concrete detailing was also designed according to ACI ITG-5.2. While other details such as external armor plates or fiber reinforced concrete at the wall toes may be possible, conventional closed steel hoops were used in the design to minimize the differences of the test specimens from typical construction. The expected base shear versus roof drift behavior of a wall designed using this process is shown in Figure 3.3.

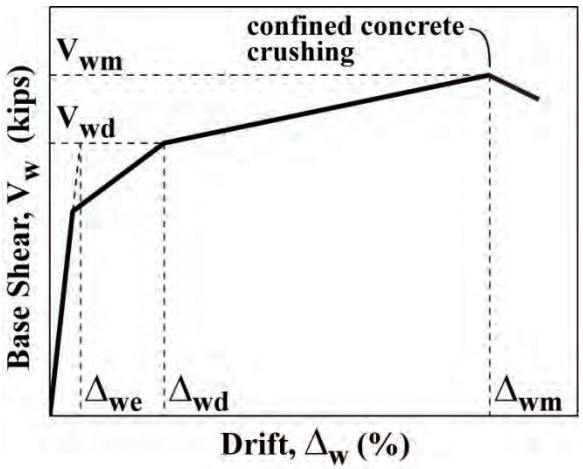

Figure 3.3 Expected Base Shear versus Roof Drift Behavior of a Hybrid Wall

The design steps above to determine the PT steel area, E.D. steel area, neutral axis lengths, and confinement steel detailing involve iterative procedures that require the determination of the PT and E.D. steel strains at Δ_{wd} and Δ_{wm}. As shown in Figure 3.4, the elongations, δ_s of the E.D. steel bars were found by lumping all of the lateral displacements of the wall at Δ_w to the gap opening rotation at the base. Note that this process tends to overestimate the steel strains since it ignores the flexural and shear deformations of the wall panels over the height of the structure. Initial selections were made for the unbonded length, l_{su} of the bars. Then, the steel strains, ε_{sd} and ε_{sm}, were determined by uniformly distributing the bar elongations at Δ_{wd} and Δ_{wm}, respectively, over l_{su}. The strain increases in the PT strands due to gap opening were also found in a similar manner, and the strain increase for each strand was added to the initial strain from prestress to determine the total strains, ε_{pd} and ε_{pm} at Δ_{wd} and Δ_{wm}, respectively. The unbonded length, l_{pu} for the PT steel was taken as the total tendon length between the anchorages.

Per ACI ITG-5.2, the E.D. reinforcement satisfied the material specifications for ASTM A706 steel. ACI ITG-5.2 also requires that the maximum strains of the E.D. steel do not exceed

$0.85\varepsilon_{su}$ (where, ε_{su} is the monotonic strain capacity of the steel at peak strength) to prevent low-cycle fatigue fracture. The unbonded lengths of the E.D. bars, l_{su}, were designed to limit the steel strains at Δ_{wm} to an allowable strain, ε_{sa}. Strain limits of up to ε_{sa}=$0.85\varepsilon_{su}$ (i.e., the ACI ITG-5.2 limit) were used in the design of the test specimens, with no low-cycle fatigue fracture observed during the experiments. Note that an additional debonded length of the E.D. bars is expected to develop during the reversed-cyclic lateral displacements of the structure. This debonded length, which is defined as $\alpha_s d_s$ per ACI ITG-5.2 (where, α_s=debonding coefficient, and d_s=bar diameter), was added to the wrapped length of each bar to determine the total unbonded length, l_{su}. In this research, the coefficients used to estimate the additional debonded length of the E.D. bars were taken as α_s=0 and α_s=2.0 at Δ_{wd} and Δ_{wm}, respectively.

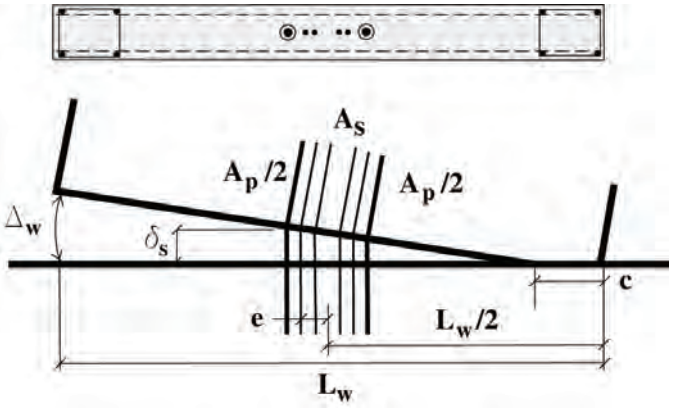

Figure 3.4 Gap Opening at Base-Panel-to-Foundation Joint

The E.D. bars crossing the base joint do not continue into the upper panel-to-panel joints, resulting in a significant reduction in the lateral strength of the wall at these locations. The philosophy behind the flexural design of the upper joints was to prevent significant gap opening and nonlinear behavior of the material through Δ_{wm}. Thus, the design of the upper joints was conducted for the maximum joint moment demands corresponding to the probable base moment strength, M_{wm} of the wall. To prevent significant gap opening at the upper joints, mild steel bars

were designed at the panel ends based on the principles of equilibrium, linear material models, and a linear strain distribution, including a capacity reduction factor, $\phi_{f,u}$ of 0.90 for flexural design. The design required that the tension steel stress was limited to f_{sy} (to limit gap opening) and the maximum concrete compressive stress was limited to $0.5f_c'$ (to keep the concrete linear-elastic), where f_{sy}=yield strength of the mild steel, and f_c'=compression strength of the unconfined panel concrete. To prevent strain concentrations in the steel, a short prescribed length of the bars [7.5-cm (3-in.)] was unbonded at the joint.

Shear slip across the horizontal joints was prevented following the design guidelines in ACI ITG-5.2. The joint shear forces were calculated from the maximum base shear force, V_{wm}, corresponding to M_{wm} at Δ_{wm}. The nominal shear friction strength at the base joint was calculated as the friction coefficient, μ_{ss}=0.5 multiplied by the compressive force in the contact region at the wall toe. For the upper joints, μ_{ss} was taken as 0.6 and the shear friction strength from the axial force due to the PT steel and the gravity load was combined with the shear friction strength from the yielding of the mild steel bars crossing the joint at both ends. As recommended by ACI ITG-5.2, the larger μ_{ss} for the upper joints as compared with the base joint is because deterioration to the grout and concrete at the base joint could lead to reduced slip strength. The design shear slip strength was calculated as the nominal strength times a capacity reduction factor, ϕ_s of 0.75.

Other steel reinforcement that was designed for the walls included: (1) distributed vertical and horizontal panel reinforcement, which was designed based on the shear (i.e., diagonal tension) requirements in ACI 318; and (2) the panel edge reinforcement, designed according to ACI ITG-5.2 to control concrete cracking initiating from the panel perimeter, particularly from the bottom of the base panel as shown in Allen and Kurama (2002). The shear design for the base panel was governed by the minimum distributed reinforcement requirements in Chapter 21

of ACI 318. Note that neither the distributed panel reinforcement nor the edge reinforcement continued across the horizontal joints; and thus, this reinforcement did not contribute to the lateral strength of the wall. More information on the design and detailing of the panel reinforcement as well as additional design checks to ensure satisfactory wall behavior through Δ_{wm} can be found in the Design Procedure Document (Smith and Kurama 2012a).

3.1.3 Design of Perforated Wall Panels

The general design philosophy for the panel perforations was to provide an adequate amount of mild steel reinforcement in the vertical and horizontal chords around each perforation such that the presence of the perforations did not negatively affect the performance of the wall through Δ_{wm}. The design approach was based on a simplified finite element model of the wall subjected to monotonic pushover analysis. As described in Section 5.2, "hard-contact" surfaces were used at the horizontal joints of the model to allow for gap opening, with linear-elastic tension properties used for the panel concrete ignoring any cracking. The resulting concrete stresses were then used to design the horizontal and vertical steel reinforcement as well as the shear reinforcement in the chords around the panel perforations (see Figure 3.5).

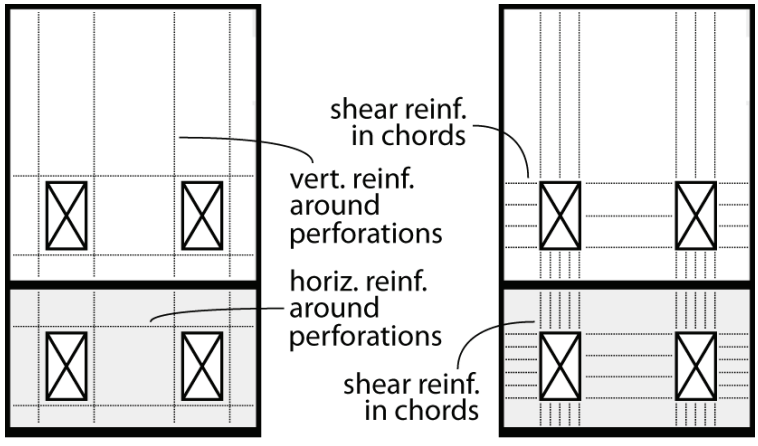

Figure 3.5 Bonded Panel Reinforcement Around Perforations: (a) Horizontal and Vertical Reinforcement; (b) Shear Reinforcement

As an example, Figure 3.6 shows the *x*-direction (i.e., horizontal) stresses, *y*-direction (i.e., vertical) stresses, and shear stresses from the pushover analysis to Δ_{wm} of one of the perforated walls (Specimen HW4) tested as part of this project. For clarity, only the critical regions of the wall where tensile *x*-direction and *y*-direction stresses and positive shear stresses develop in the concrete are displayed in color, with the other regions colored in black. As shown in Figures 3.6(a) and 3.6(b) for the *x* and *y*-directions, respectively, the required area, $A_{s,c}$ of the horizontal and vertical reinforcement around each perforation was designed by summing the tensile stresses along a cutline (or critical path) to determine the total tensile force, T_c. The required steel area in each region was then determined by dividing the total tensile force by the yield strength of the steel. This process was also applied to the design of the horizontal edge reinforcement along the bottom edge of the base panel.

Similar to the solid wall panels, the perforated wall panels were intentionally designed not to have any significant over-capacity beyond the design requirements. This decision was made in an effort to determine if the procedures used to design the required chord steel areas were overly conservative, not conservative enough, or reasonable. Accordingly, no capacity reduction factor was used in the design of the panel reinforcement and the provided steel areas were similar to the required areas where practical (note that in some regions of the panel, practical constraints pertaining to the area and number of standard bar sizes resulted in the use of a greater steel area than required).

A similar procedure was followed to calculate the critical shear forces in the horizontal and vertical chords around the perforations [see Figure 3.6(c)]. Once the maximum chord shear forces were determined, the required shear reinforcement areas were calculated following the applicable guidelines in Section 21.9 of ACI 318 (2011), but without a capacity reduction factor for shear. Note that the requirements for coupling beams in Section 21.9.7 of ACI 318 do not

apply to the reinforcement around the perforations since the bars placed around the perforations are designed not to yield.

In order to satisfy the maximum limit for the shear strength of a horizontal wall segment (Section 21.9.4.5 of ACI 318), the two adjacent horizontal chords located above the base panel perforation and below the upper panel perforation were combined into one deep chord. This is acceptable since the upper panel-to-panel joint is designed to be closed between these two chords (i.e., the panels are in contact). This is shown in Figure 3.6(c), where the structure has been laterally displaced to the left (note the gap opening at the base joint on the right side of the wall) and the upper panel-to-panel joint between the critical perforations on the left side of the wall remains closed, resulting in a flow of shear stresses across the joint. While the depths of the two horizontal chords were combined to satisfy the maximum shear strength limit in ACI 318, each chord was still designed and reinforced as a separate component (i.e., using the individual chord depth and shear stresses in that chord).

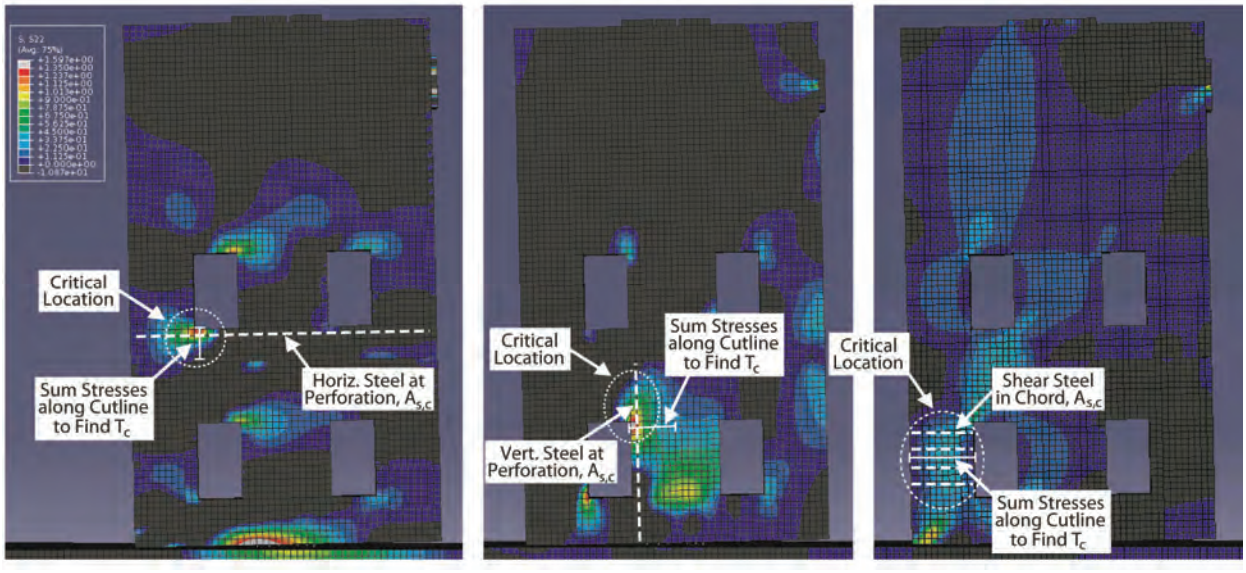

(a) **(b)** **(c)**

Figure 3.6 Representative Finite Element Analytical Results:
(a) *X*-Direction Tensile Stresses; (b) *Y*-Direction Tensile Stresses; (c) Shear Stresses

3.2 DESIGN PROCEDURE DOCUMENT

The Design Procedure Document in Smith and Kurama (2012a) contains detailed seismic design guidelines and analysis tools for hybrid precast concrete shear walls based on the experimental and analytical results from this research project. A full-scale design example demonstrating step-by-step application of the design process is also included. Both a performance-based design procedure and a prescriptive design procedure are provided. The document presents specific design recommendations, material assumptions, and critical steel reinforcement details to ensure that the system can achieve the required lateral strength, stiffness, displacement capacity, energy dissipation, and self-centering without undergoing undesirable failure mechanisms under seismic loads. The design of rectangular perforations within the wall panels is also addressed. Where appropriate, ACI 318 (2011) requirements for special monolithic cast-in-place reinforced concrete shear wall structures are utilized to help in the adoption of the hybrid wall design procedure by practicing engineers. Applicable references and suggested modifications/additions to the design recommendations and requirements in ACI ITG-5.2 (2009) are also included.

The design and analysis guidelines outlined in the Design Procedure Document have been validated through the measured and predicted behaviors of the six wall specimens tested as part of this project. The analytical modeling guidelines and recommendations include a linear-elastic effective stiffness model as well as a basic finite element model for nonlinear monotonic pushover analysis as an aid to design hybrid walls with predictable and reliable behavior. The finite element model is especially needed for the design of panel perforations. The analytical modeling recommendations intentionally incorporate several simplifying assumptions appropriate for the design office. The document also describes a detailed fiber element model

that can be used to conduct reversed cyclic and dynamic analyses of hybrid walls; however, this model is not a necessary tool for seismic design.

CHAPTER 4

EXPERIMENTAL PROGRAM

The experimental program featured six large-scale precast wall test specimens designed, constructed, and tested according to the requirements of ACI ITG-5.1 (2007). The main objective of these tests was to validate the hybrid precast wall system as a type of "special" reinforced concrete shear wall per ACI 318 (2011). ACI code validation was not an objective of the small amount of research previously conducted on hybrid walls. The current study aimed to fill this gap to provide the necessary experimental, analytical, and design evidence for practical application in the U.S.

The main specimen parameters that were investigated include: (1) relative amounts of E.D. steel and PT steel crossing the base-panel-to-foundation joint; (2) detailing of the E.D. steel reinforcement at the wall base; (3) concrete confinement detailing; and (4) presence of perforations within the wall panels. Unlike previous experimental research on hybrid walls, the current study used two panels in each specimen, allowing for the behavior at both the base-panel-to-foundation joint and the upper panel-to-panel joint to be assessed. In addition, the specimens with panel perforations, a common design feature in practice, provided unique insight on the effect of the perforations on the design and behavior of the structures.

4.1 EXPERIMENTAL TEST SETUP

Schematic drawings of the wall test specimens and photographs of two representative walls are shown in Figure 4.1. Specimens HW1, HW2, and HW3 were solid hybrid walls while Specimens HW4 and HW5 were perforated hybrid walls. Specimen EW was an emulative precast concrete structure that was tested as a baseline comparison with the hybrid walls.

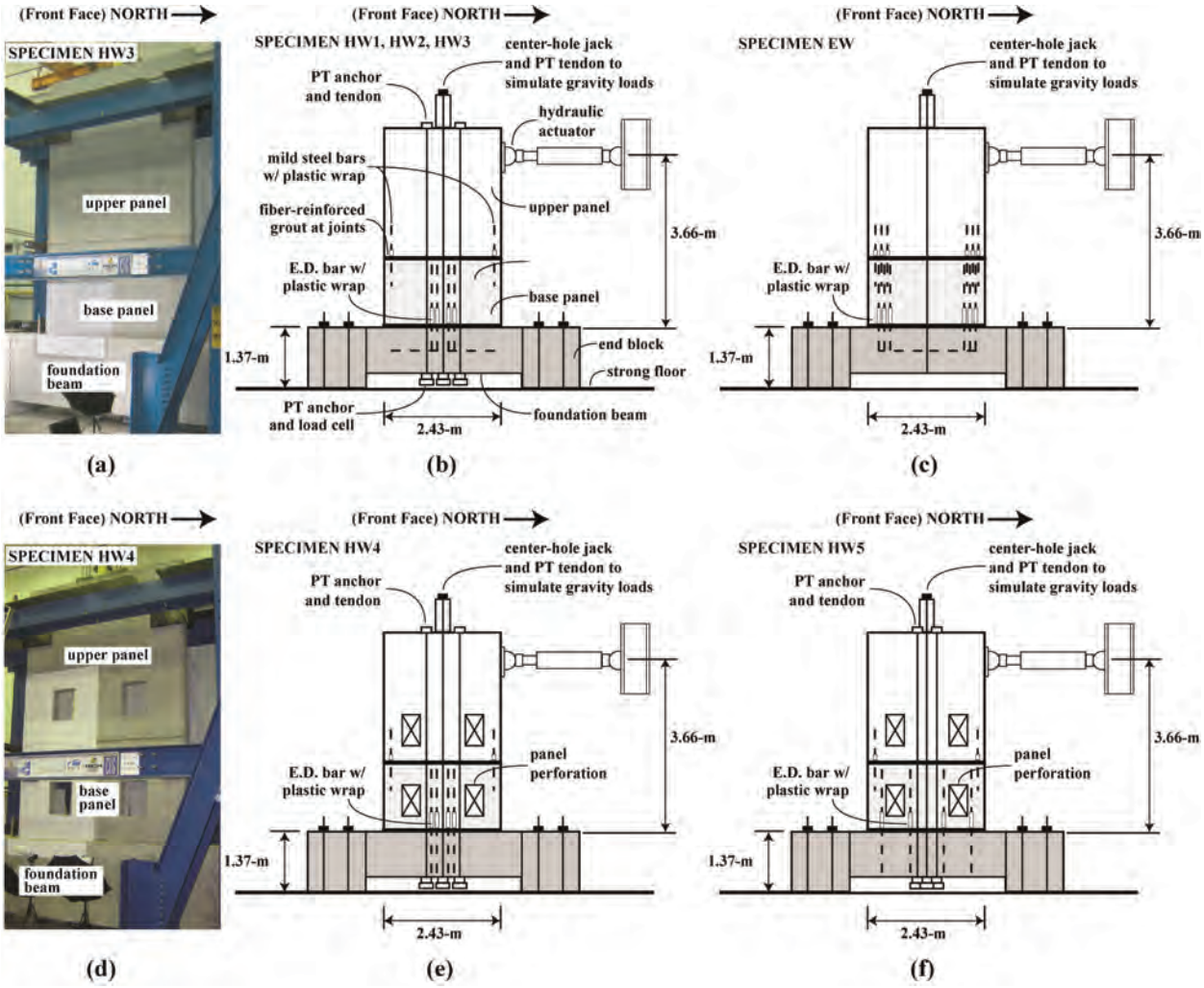

Figure 4.1 Test Configuration: (a) Photograph of Solid Specimen HW3; (b) Schematic of Solid Specimens HW1, HW2 and HW3; (c) Schematic of Solid Specimen EW; (d) Photograph of Perforated Specimen HW4; (e) Schematic of Perforated Specimen HW4; (f) Schematic of Perforated Specimen HW5

Each test was conducted at 0.40-scale, which satisfies the minimum scaling limit of ACI ITG-5.1. The specimens featured two wall panels: the base panel representing the 1st story of the prototype structure described in Chapter 3 and the upper panel representing the 2nd through 4th stories, thereby satisfying the ACI ITG-5.1 requirement for testing multi-panel walls (such that the base-panel-to-foundation joint as well as an upper panel-to-panel joint are evaluated). It was possible to model the upper story panels of the prototype wall as a single panel since the joints between these panels were designed to have no nonlinear behavior and no gap opening. The wall

panels were supported by a three piece reinforced concrete foundation fixture consisting of a foundation beam and two end blocks. The foundation beam provided the anchorages for the PT and E.D. steel reinforcement and resisted the compressive forces from the base panel of the test specimens. The end blocks provided the connections of the entire test assembly to the laboratory strong floor. The three foundation fixture pieces were post-tensioned in the horizontal direction using eighteen 1.27-cm (0.5-in.) diameter strands. The end blocks remained mostly undamaged after each test; and thus, were reused during the experimental program while the foundation beam was recast several times to accommodate the different test specimens.

The properties of each wall specimen were determined from the prototype wall structure. The 0.40-scale wall length, L_w, was 243-cm (96-in.), base panel height, H_{bp}, was 145-cm (57.5-in.), and wall thickness, t_w, was 15.9-cm (6.25-in.). The lateral load was applied 3.66-m (12-ft) from the wall base (near the resultant location of the 1st mode inertial forces), resulting in a relatively low wall base moment to shear ratio of M_{wd}/V_{wd}=1.5L_w. An external downward axial force was applied [534-kN (120-kips) for Specimen HW5 and 325-kN (73-kips) for all other specimens] at the center of the top of each specimen to simulate the service-level tributary gravity loads acting on the prototype structure during an earthquake. The total gravity load was calculated as 1.0 times the service dead load (including wall self weight) plus 0.25 times the unreduced service live load. The larger external axial load in Specimen HW5 was due to an alternate gravity column configuration for the prototype building, resulting in a larger tributary area and corresponding gravity load for the prototype wall.

4.2 TEST SPECIMEN PROPERTIES

The critical base panel reinforcement details for the six specimens are depicted in Figures 4.2 - 4.7 (shop drawings courtesy of the Consulting Engineers Group, Inc., Texas, USA)

and the important design features of the walls are listed in Table 4.1. The main differences between the specimens were:

- The area and location of the PT steel tendons.
- The area and location of the E.D. steel bars.
- The wrapped (unbonded) length of the E.D. steel bars, which influences the maximum bar strains and energy dissipation.
- The continuity detail of the E.D. bars across the base joint, which featured either Type II mechanical splice connections (as permitted by Section 21.1.6 of ACI 318 and Section 5.4.2 of ACI ITG-5.2) or continuous reinforcement grouted into the foundation (i.e., the development length of the E.D. bars projected beyond the bottom of the base panel and were grouted into corrugated metal ducts cast into the foundation).
- The detailing of the confinement steel reinforcement at the wall toes (i.e., confined region length, confinement hoop dimensions/configuration and spacing, and distance of the first hoop from the bottom of the base panel).
- The size and spacing of the distributed panel reinforcement using welded wire fabric or deformed reinforcing bars, as well as the end details of the horizontal distributed reinforcement at the wall base.
- The presence of rectangular perforations in the wall panels, which were placed in a symmetrical layout with respect to the wall centerline. The perforations in the upper panel represented those in the 2nd story of the prototype wall. The perforations in the 3rd and 4th stories of the prototype wall were not modeled since they would be less critical than the lower story perforations.

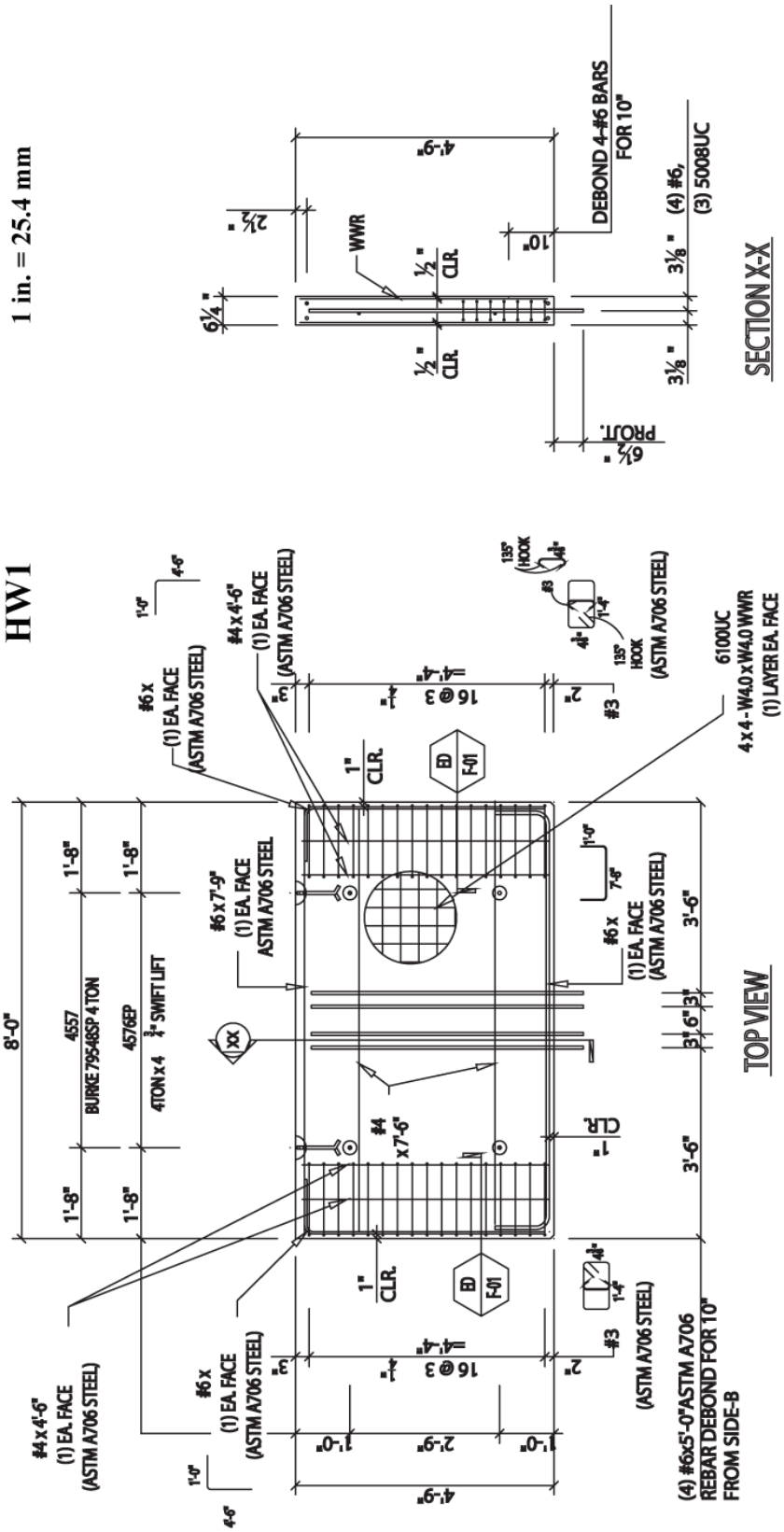

Figure 4.2 Base Panel Details for Specimen HW1 (Elevation View, Courtesy of the Consulting Engineers Group, Inc., Texas, USA)

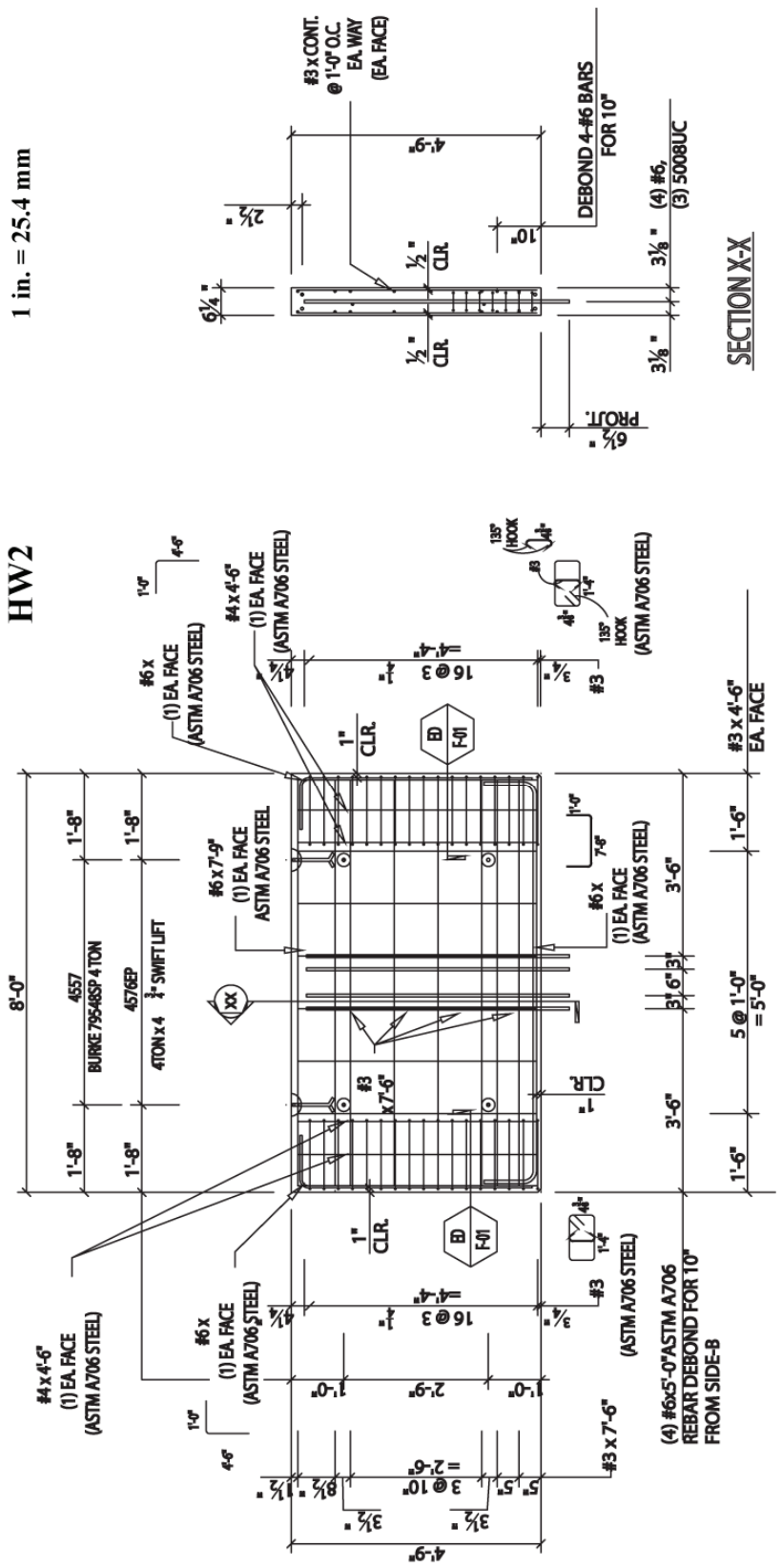

Figure 4.3 Base Panel Details for Specimen HW2 (Elevation View, Courtesy of the Consulting Engineers Group, Inc., Texas, USA)

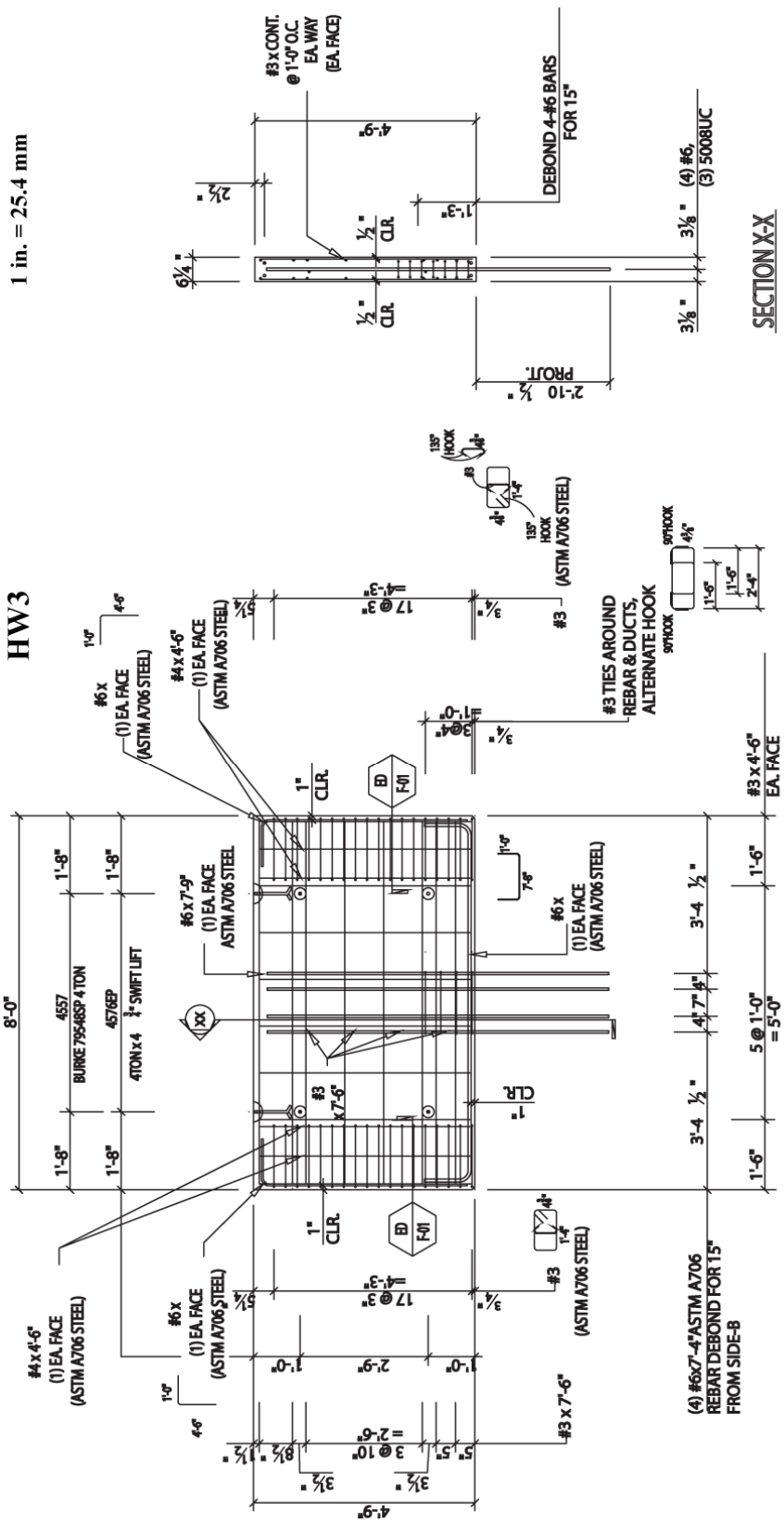

Figure 4.4 Base Panel Details for Specimen HW3 (Elevation View, Courtesy of the Consulting Engineers Group, Inc., Texas, USA)

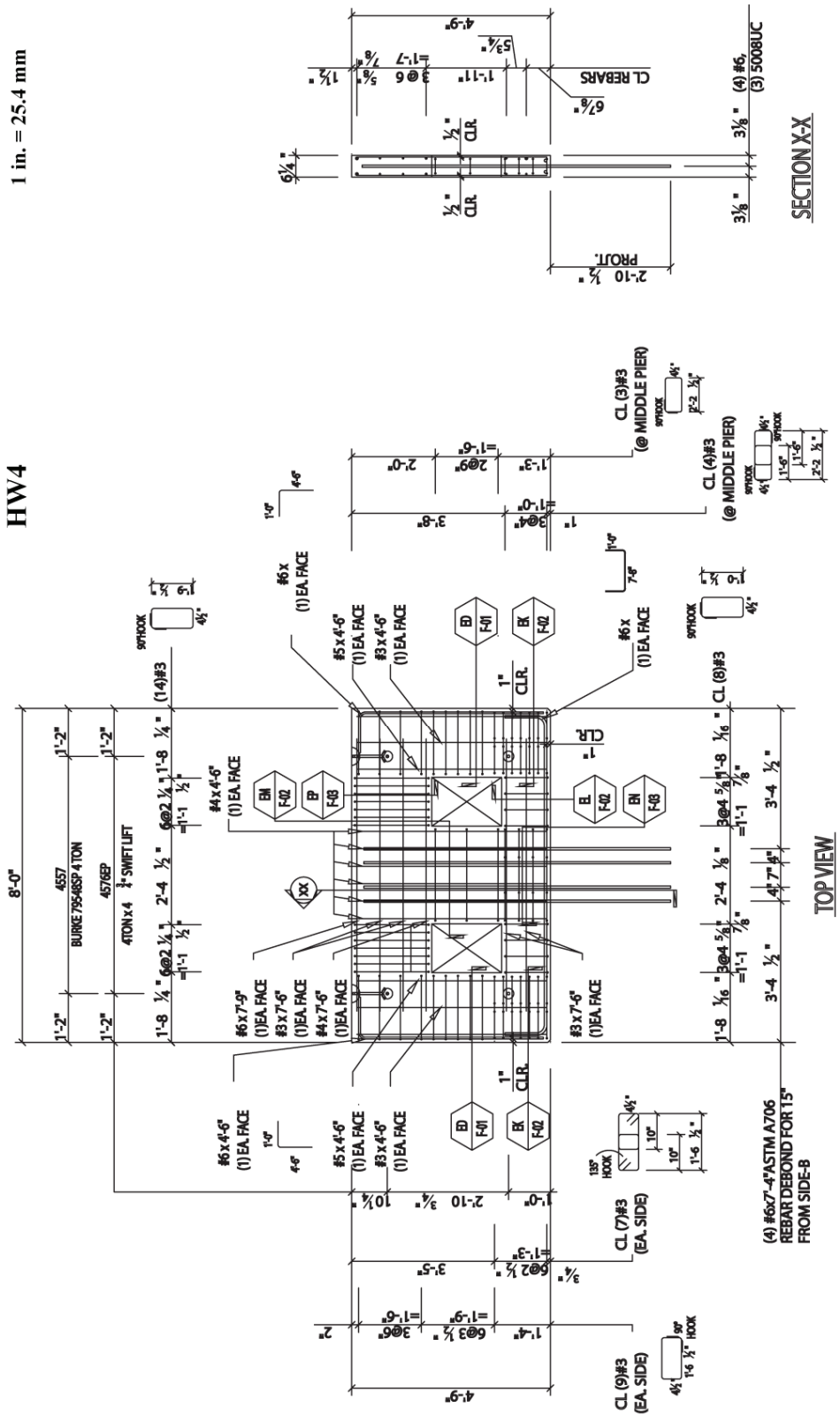

Figure 4.5 Base Panel Details for Specimen HW4 (Elevation View, Courtesy of the Consulting Engineers Group, Inc., Texas, USA)

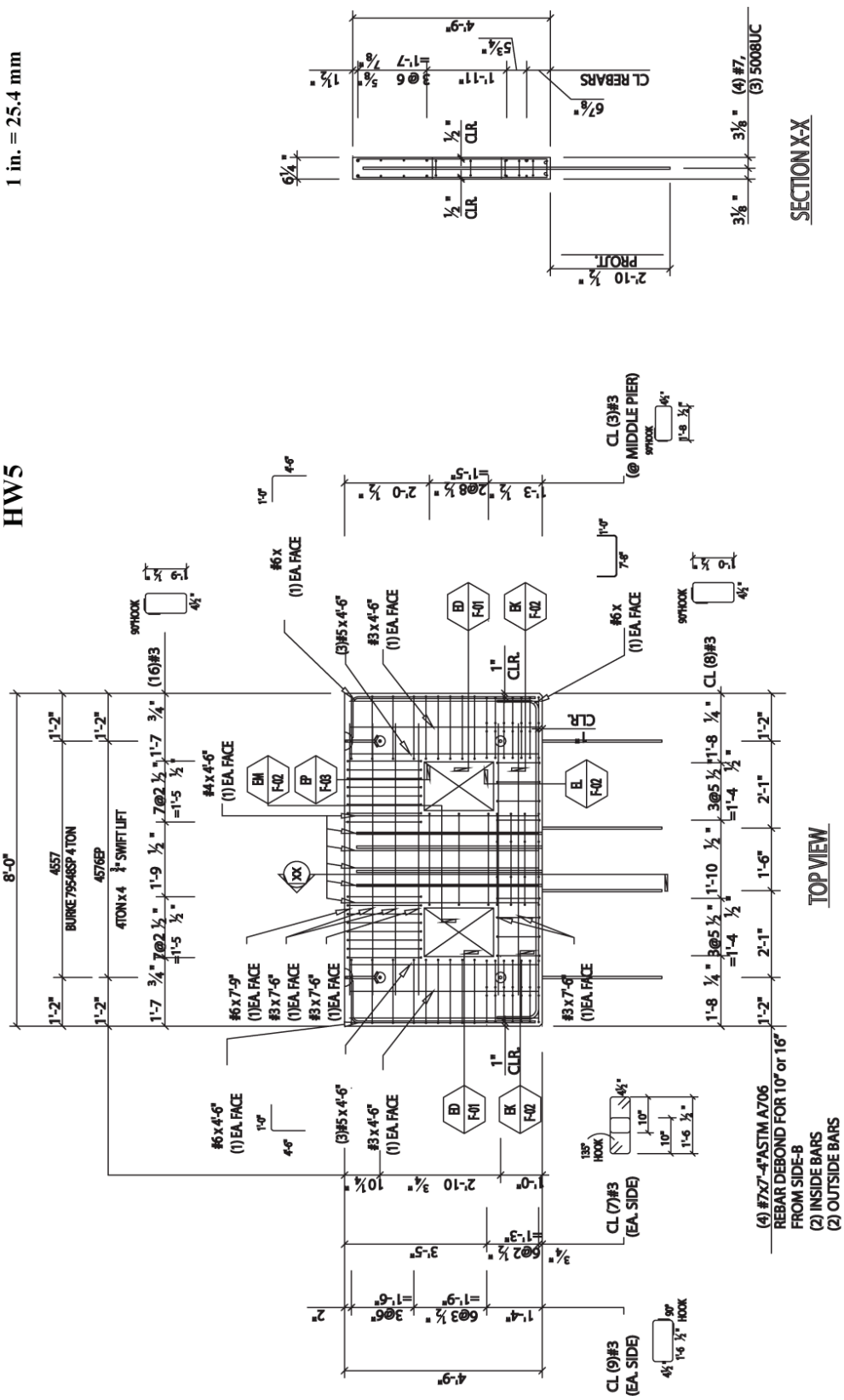

Figure 4.6 Base Panel Details for Specimen HW5 (Elevation View, Courtesy of the Consulting Engineers Group, Inc., Texas, USA)

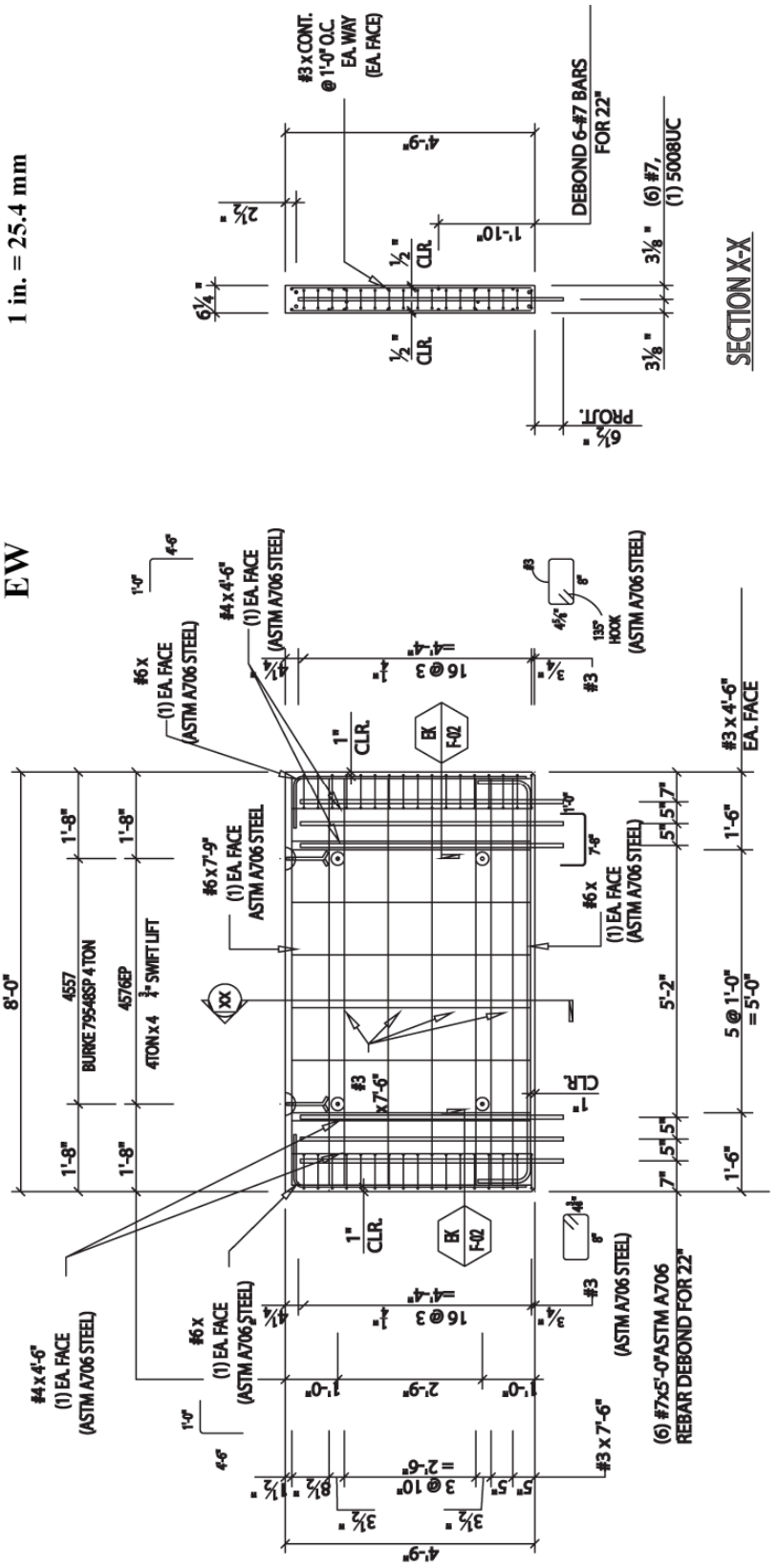

Figure 4.7 Base Panel Details for Specimen EW (Elevation View, Courtesy of the Consulting Engineers Group, Inc., Texas, USA)

For each specimen, the PT steel was grouped in two tendons near the wall centerline to reduce the strand elongations due to gap opening and keep the PT ducts away from the critical base panel ends. The E.D. steel crossing the base joint was also typically located near the wall centerline to reduce the bar elongations and the associated required unbonded lengths. As compared with a distributed bar arrangement, the lumped reinforcement detail may provide ease of placement during the precast concrete erection process. Exceptions were made in Specimen HW5, where the E.D. steel was distributed along the length of the wall, and in Specimen EW, where the E.D. steel was lumped near the ends of the wall. The unbonded lengths of the bars were located within the base panel for ease of construction during the experimental program (if desired, the unbonded lengths may also be placed within the foundation without affecting the performance of the structure). The mild steel bars designed to limit gap opening across the upper panel-to-panel joint were located at the wall ends and a short prescribed length [7.6-cm (3.0-in.)] of the bars were unbonded within the bottom of the upper panel to prevent strain concentrations. Uniformly spaced No. 10 (U.S. No. 3) mild steel bars were typically used as the distributed panel reinforcement, except in Specimen HW1 where welded-wire fabric was used. Figure 4.8 shows the panel layout for Specimens HW3 and HW4 prior to concrete casting.

Table 4.1 Specimen Properties

Spec. No.	Panel Perf. (cm)	κ_d		PT Tendons			E.D. Bars					Confined Region		
		Design	Actual	No. of strands and diameter	[1]f_{pi}/f_{pu}	Eccentricity [2]e_p (cm)	Size	Eccentricity [2]e_s (cm)	Wrapped Length (cm)	[3]$\varepsilon_{sm}/\varepsilon_{su}$	Continuity at Base	[4]l_h (cm)	[5]s_h (cm)	[6]s_{bot} (cm)
HW1	-	0.50	0.53	3 – 1.27-cm	0.54	±23	No. 19	±7.5, 15	25	0.64	Spliced	40	8.3	5.0
HW2	-	0.50	0.53	3 – 1.27-cm	0.54	±23	No. 19	±7.5, 15	25	0.61	Spliced	40	8.3	1.9
HW3	-	0.50	0.50	3 – 1.27-cm	0.54	±28	No. 19	±8.9, 19	38	0.48	Cont.	40	7.6	1.9
HW4	36x51	0.50	0.54	3 – 1.27-cm	0.54	±28	No. 19	±8.9, 19	38	0.49	Cont.	47	6.4	1.9
HW5	43x51	0.85	0.90	2 – 1.27-cm	0.54	±14	No. 22	±23, 86	25, 40	0.85	Cont.	47	6.4	1.9
EW	-	-	-	-	-	-	No. 22	±79, 91, 104	56	0.73	Spliced	20	8.3	1.9

[1]f_{pi}=average initial strand stress; f_{pu}=design ultimate strength of strand [1862-MPa (270-ksi)]; [2]measured from wall centerline; [3]ε_{sm}=maximum expected (design) E.D. bar strain at Δ_{wm}=2.30%; ε_{su}=strain at maximum (peak) strength of E.D. steel from monotonic material testing; [4]confined region length at wall toes (center-to-center of bar); [5]confinement hoop spacing (center-to-center of bar); [6]first hoop distance from bottom of base panel (to center of bar)

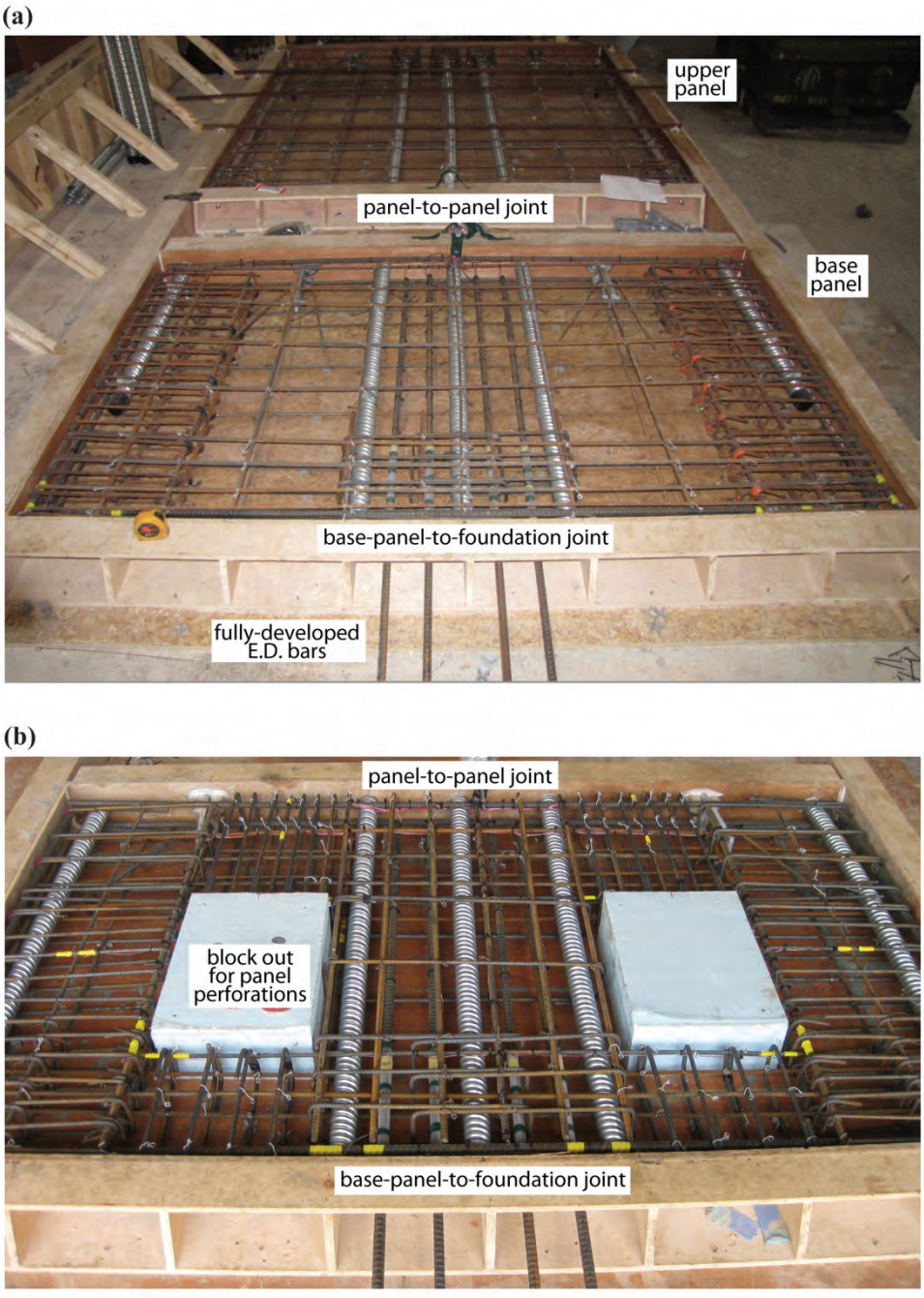

Figure 4.8 Reinforcement Layout: (a) Base Panel and Upper Panel for Specimen HW3; (b) Base Panel for Specimen HW4

Figure 4.9(a) shows the four E.D. bars at the base of Specimen HW3 prior to the placement of the concrete and Figure 4.9(b) shows the three bars crossing the base joint at the south end of Specimen EW. The plastic-wrapped unbonded lengths of the bars (shown in the

photographs) were used to limit the tensile steel strains and thus, prevent low-cycle fatigue fracture, while also allowing significant yielding of the bars as the walls were displaced.

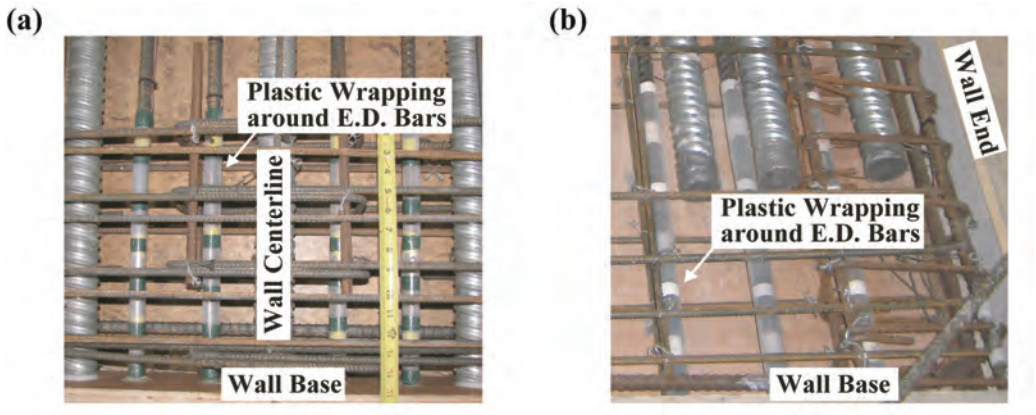

Figure 4.9 E.D. Steel: (a) Bar Placement in Specimen HW3; (b) Bar Placement in Specimen EW

4.3 MATERIAL PROPERTIES

The measured stress-strain behavior of the ASTM A416 PT strand [with a design ultimate strength of 1862-MPa (270-ksi)] used in the hybrid wall specimens can be seen in Figure 4.10(a). The strand was tested using sand-grip anchors as described in Walsh and Kurama (2010). The "yield" stress of 1620-MPa (235-ksi) was determined by using the measured proportionality limit in the strand stress-strain relationship. Similarly, Figure 4.10(b) depicts the measured behavior of the ASTM A706 Grade 400 (U.S. Grade 60) E.D. steel, which crossed the base joint of the walls. The E.D. bars for Specimens HW1 and HW2 were from the same material heat; and thus, they had the same stress-strain properties. Note that the measured stress-strain relationship of the E.D. bars in Specimens HW5 and EW did not have a distinct yield plateau. For these bars, the yield strength was taken as the stress corresponding to a strain of 0.0035-cm/cm. Figure 4.10(c) shows the measured stress-strain behavior of the ASTM A615 Grade 400 (U.S. Grade 60) confinement steel at the wall toes. The confinement steel for Specimens HW1, HW2, HW3, and EW were all from the same material heat, while the

confinement steel for Specimens HW4 and HW5 were from another material heat. Some of the important measured properties for the PT steel, E.D. steel, and confinement steel are listed in Table 4.2. The other mild steel reinforcement used in the wall specimens [ASTM A615 Grade 400 (U.S. Grade 60)] was not designed to yield, and thus, their measured behavior is not shown for brevity. The PT and mild steel strains were measured using an MTS® Model 634.25E-24 extensometer with 5.1-cm (2.0-in) gauge length. The extensometer was removed prior to fracture, with the remaining strains calculated from the relative displacements of the testing machine crossheads.

The design unconfined concrete compressive strength for the walls was f_c'=41-MPa (6.0-ksi), with the actual 28-day strength of the concrete limited to a maximum of 59-MPa (8.5-ksi) so as not to result in an overly strong material as compared to the design properties. The design confined concrete strength (at the toes of the base panel) ranged from 62-MPa (9.0-ksi) to 65-MPa (9.5-ksi) depending on the confinement detailing (see Table 4.1). The measured 28-day and test-day strengths [from 10x20-cm (3x6-in.) cylinders] as well as the secant stiffnesses (determined from two points on the measured stress-strain relationship, one point at a strain of 0.00005 and the other at a stress of 0.40 times the measured peak stress) for the unconfined base panel concrete are listed in Table 4.2. The concrete strains were measured using an Epsilon® 3542RA rock averaging extensometer with 5.1-cm (2.0-in) gauge length. It can be seen that the actual unconfined concrete strength in Specimen HW1 was considerably smaller than the concrete strength in the other specimens. This is because the concrete in Specimen HW1 did not reach the specified design strength, which contributed to the premature deterioration of this wall as discussed in more detail in Section 6.2.

The non-shrink, dry-pack grout placed at the base-panel-to-foundation and upper panel-to-panel joints was a very important component in the design and construction of the wall. The grout was reinforced with polypropylene microfilament fibers (at 0.065% by volume per

manufacturer's recommendations) to ensure sufficient ductility and toughness. The design 28-day compressive strength of the grout was specified to be within ±20% of the design 28-day unconfined concrete strength of the base panel to provide a matching bearing bed for the panel concrete at the joints. The measured 28-day and test-day strengths [from 5x5-cm (2x2-in.) grout cubes] as well as the secant stiffnesses [from 10x20-cm (3x6-in.) grout cylinders with strains measured using the Epsilon® 3542RA rock averaging extensometer] for the base joint grout are listed in Table 4.2. Note that the placement of the grout at each joint was completed in a single application to ensure proper integrity of the grout pad. The grout was packed directly in between the concrete surfaces at each joint, with no bond breaker or other material applied on the concrete. The PT strands were isolated from the grout by placing a short length of duct around each tendon across the joint, thereby ensuring that the deformations of the steel did not deteriorate the integrity of the grout pad. For Specimens HW3, HW4, and HW5, the E.D. bars were also isolated from the grout by extending the unbonded (i.e., wrapped) length of the bars. This was not done for Specimens HW1, HW2, and EW, resulting in localized splitting of the grout pad around some of the E.D. bars.

The measured 28-day and test-day strengths [from 5.1x5.1-cm (2.0x2.0-in) cubes] for the grout used inside the E.D. bar splices and ducts are also listed in Table 4.2. The grout used in the Type II mechanical splice connections for Specimens HW1, HW2, and EW was a product directly supplied by the splice manufacturer. A standard bagged grout mix was used in the continuous E.D. bar anchorage detail for Specimens HW3, HW4, and HW5 (where the development length of each E.D. bar projecting beyond the bottom of the base panel was grouted into a corrugated metal duct cast into the foundation).

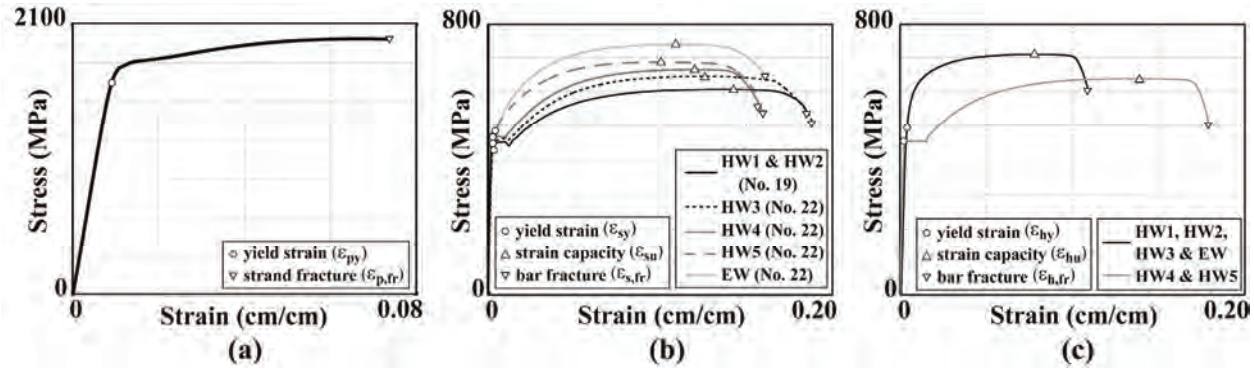

Figure 4.10 Material Behavior: (a) PT Strand; (b) E.D. Steel; (c) Confinement Steel

Table 4.2 Material Properties

Spec. No.	PT Strand		E.D. Steel					Confinement Hoop Steel					Base Panel Concrete			Base Joint Grout			E.D. Bar Grout	
	[1]f_{py} (MPa)	[2]ε_{py} (%)	[1]f_{sy} (MPa)	[2]ε_{sy} (%)	[3]f_{su} (MPa)	[4]ε_{su} (%)	[5]$\varepsilon_{s,fr}$ (%)	[1]f_{hy} (MPa)	[2]ε_{hy} (%)	[3]f_{hu} (MPa)	[4]ε_{hu} (%)	[5]$\varepsilon_{h,fr}$ (%)	[6]$f'_{c,28d}$ (MPa)	[7]$f'_{c,td}$ (MPa)	[8]$E_{c,td}$ (MPa)	[6]$f'_{c,28d}$ (MPa)	[7]$f'_{c,td}$ (MPa)	[8]$E_{c,td}$ (MPa)	[6]$f'_{c,28d}$ (MPa)	[7]$f'_{c,td}$ (MPa)
HW1	1620	0.83	448	0.21	608	13.7	18.5	494	0.35	712	7.85	10.8	30.3	32.4	-	29.6	31.0	-	59.3	60.0
HW2	1620	0.83	448	0.21	608	13.7	18.5	494	0.35	712	7.85	10.8	48.3	44.8	-	40.7	40.0	-	58.6	59.3
HW3	1620	0.83	462	0.23	647	12.4	18.8	494	0.35	712	7.85	10.8	53.1	55.2	29040	45.5	57.9	31343	49.6	51.7
HW4	1620	0.83	465	0.28	667	12.0	16.0	456	0.23	639	12.9	17.9	47.0	47.9	23420	50.9	58.0	30298	51.0	47.2
HW5	1620	0.83	471	0.35	688	10.0	15.7	456	0.23	639	12.9	17.9	46.4	45.1	24382	46.8	50.2	30779	40.9	41.7
EW	-	-	419	0.35	741	10.8	16.1	494	0.35	712	7.85	10.8	47.6	45.5	-	42.1	38.6	-	82.7	95.1

Notes: Results are averages from 3 material samples each. [1]f_{py},f_{sy},f_{hy}=yield strength; [2]ε_{py},ε_{sy},ε_{hy}=strain at f_{py},f_{sy},f_{hy} [○ markers in Figures 4.10(a), (b), and (c)]; [3]f_{su},f_{hu}=ultimate (maximum) strength; [4]ε_{su},ε_{hu}=strain at f_{su},f_{hu} [Δ markers in Figures 4.10(b) and (c)]; [5]$\varepsilon_{s,fr}$,$\varepsilon_{h,fr}$=fracture strain at 0.85f_{su},0.85f_{hu} [∇ markers in Figures 4.10(b) and (c)]; [6]$f'_{c,28d}$=maximum (peak) strength of unconfined concrete or grout at 28 days; [7]$f'_{c,td}$=maximum (peak) strength of unconfined concrete or grout at day of wall testing; [8]$E_{c,td}$=secant stiffness of unconfined concrete or grout at day of wall testing.

4.4 RESPONSE MEASUREMENT SYSTEMS

Two different measurement systems were used to monitor the behavior of the test specimens: (1) a conventional system featuring displacement sensors, rotation sensors, load cells, and strain gauges; and (2) a three-dimensional digital image correlation (3D-DIC) system using a non-contact optical technique. As partially shown in Figure 4.11, the conventional system included up to 89 channels of data with up to 27 displacement sensors, 5 rotation sensors, 9 load cells, and 48 strain gauges. The displacement sensors, consisting of string potentiometers and linear variable displacement transducers (LVDTs), were used to measure the in-plane displacements of the wall panels and the foundation beam, gap/contact behavior and horizontal

slip across the base-panel-to-foundation and upper panel-to-panel joints, shear deformations of the base panel, and extent of the crushing zone at the wall toes. The rotation sensors were used to record the in-plane rotations of the base panel, upper panel, and foundation beam. The load cells were used to measure the applied lateral force, the vertical force simulating service-level gravity loads on the wall, and the forces in the individual PT strands. Finally, the strain gauges were used to measure the strains in the mild steel bars across the base panel and upper panel joints, the compression strains of steel bars embedded vertically inside the confined concrete cores at the wall toes, and the tensile strains in the horizontal edge reinforcement at the bottom of the base panel as well as the horizontal, vertical, and shear reinforcement placed around the panel perforations.

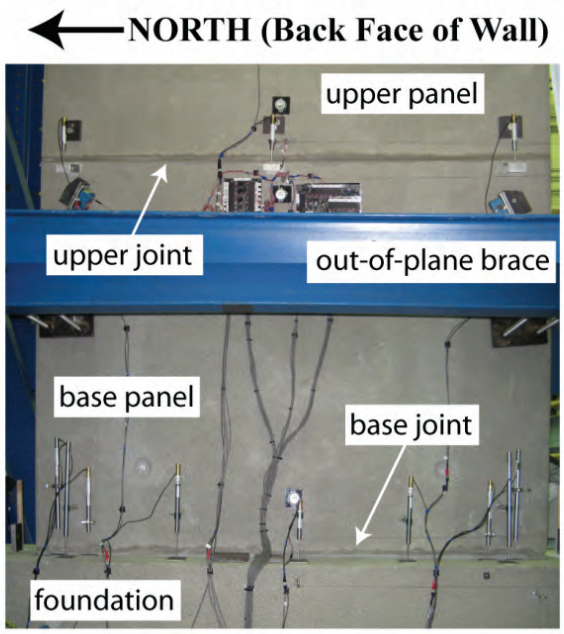

Figure 4.11 Conventional Measurement System

The 3D-DIC monitoring of the test specimens was carried out by Professor Michael McGinnis and his student, Michael Lisk, of the University of Texas at Tyler. As shown in Figure 4.12(a), each 3D-DIC system consisted of two cameras measuring the in-plane and out-of-plane displacements of the wall surface within the "field of view" [i.e., white-painted regions in

Figures 4.12(b) and 4.12(c)]. 3D-DIC has been previously used to monitor deformations in civil engineering applications (Orteu 2009; McGinnis et al. 2005; Corr et al. 2007). In this method, a random pattern is applied to the surface of the test specimen and stereo pairs of photographs of this pattern are captured during the loading of the structure. The captured digital images are divided into regions that are several pixels across, called facets. These facets are tracked through an image series using pattern recognition and photogrammetric triangulation principles, thus yielding essentially full-field, 3D surface displacements and strains of the specimen within the field of view.

The field of view for the solid walls (Specimens HW1, HW2, HW3, and EW) consisted of the south end of the base panel over a region of approximately one half the panel length and one half the panel height at the bottom, as well as a portion of the foundation beam [white-painted region in Figure 4.12(b)]. For the perforated walls (Specimens HW4 and HW5), two separate 3D-DIC systems were used. As a result, the field of view was expanded [white-painted regions in Figure 4.12(c)] to include the entire height of the base panel, the perforated portion of the upper panel, as well as the base-panel-to-foundation and upper panel-to-panel joints over half the wall length at the south end. The accuracy of 3D-DIC scales somewhat linearly with the field of view. For the field of view of the test specimens in this research, the in-plane accuracy for displacements was better than ±50 microns for the solid walls and ±65 microns for the perforated walls. The use of 3D-DIC provided unprecedented information on the behavior of the test specimens near the base joint and around the perforations. Advantages of the technique include ease of set-up and the full-field, 3D results. Disadvantages include inability to capture deformations beyond the cover spalling point or inside the specimen.

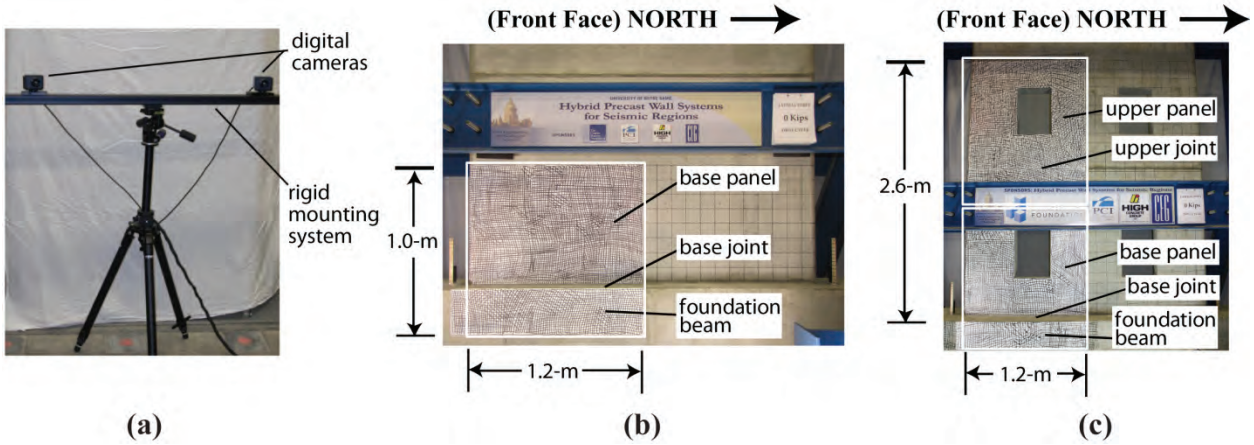

Figure 4.12 3D-DIC Measurement System: (a) Camera Setup; (b) Field of View for Solid Walls; (c) Field of View for Perforated Walls

This page intentionally left blank.

CHAPTER 5

ANALYTICAL PROGRAM

Three different analytical models were developed for the seismic design and analysis of the wall test specimens in this project: (1) a linear-elastic effective stiffness model; (2) a simplified finite element model; and (3) a detailed fiber element model. The linear-elastic effective stiffness model was used as part of the equivalent lateral force procedure in ASCE 7 (2010) and the finite element model was used for the design of panel perforations. The fiber element model was created to conduct reversed cyclic and dynamic analyses of the specimens, and was not used as a design tool.

The analytical models intentionally incorporated several simplifying assumptions appropriate for the design office and have been validated based on the results from the experimental program. Measured material and geometrical properties were used in the modeling of the test specimens. The finite element and fiber element models were developed using the ABAQUS (Hibbitt et al. 2009) and DRAIN-2DX (Prakash et al. 1993) programs, respectively. As a result, some of the modeling terminology may be specific to these programs. However, the assumptions, guidelines, and philosophies used in the creation of these models could be successfully applied to other analysis platforms as well, such as SAP2000 (CSI 2008), OpenSees (Mazzoni et al. 2007), and ANSYS (ANSYS Inc. 2009).

5.1 LINEAR-ELASTIC EFFECTIVE STIFFNESS MODEL

The lateral displacements of a hybrid precast concrete shear wall after the initiation of gap opening but prior to the significant nonlinear behavior of the concrete at the wall toes and significant yielding of the E.D. reinforcement crossing the base joint can be modeled using a

reduced, linear-elastic, effective stiffness model. The total roof displacement of the wall can be calculated as the summation of the wall displacements due to flexural and shear effects.

The flexural displacements of the test specimens were modeled using an effective moment of inertia, I_e of the wall cross section that accounts for the gap opening at the base. An expression for I_e was developed using the model in Figure 5.1, where the lateral displacements of the wall due to gap opening were represented by a rotational spring. The total flexural displacement at the roof, $\delta_{w,flex}$, was calculated as the summation of the displacement, δ_{we}, due to the linear-elastic deformations of the wall over its height and the displacement, $\delta_{w,gap}$, due to the gap opening rotation, θ_{gap}, at the base. As described in detail in the Design Procedure Document (Smith and Kurama 2012a), an effective moment of inertia of I_e=0.5I_{gross} was used for design purposes, where I_{gross} is the gross moment of inertia of the wall cross-section and the 0.5 factor represents a reduction in the flexural stiffness of the wall due to gap opening over approximately 82.5% of the wall length at the base (i.e., neutral axis length of c=0.175L_w). The gross moment of inertia, I_{gross}, of the perforated walls was calculated based on the cross-section of the wall at the location of the panel perforations.

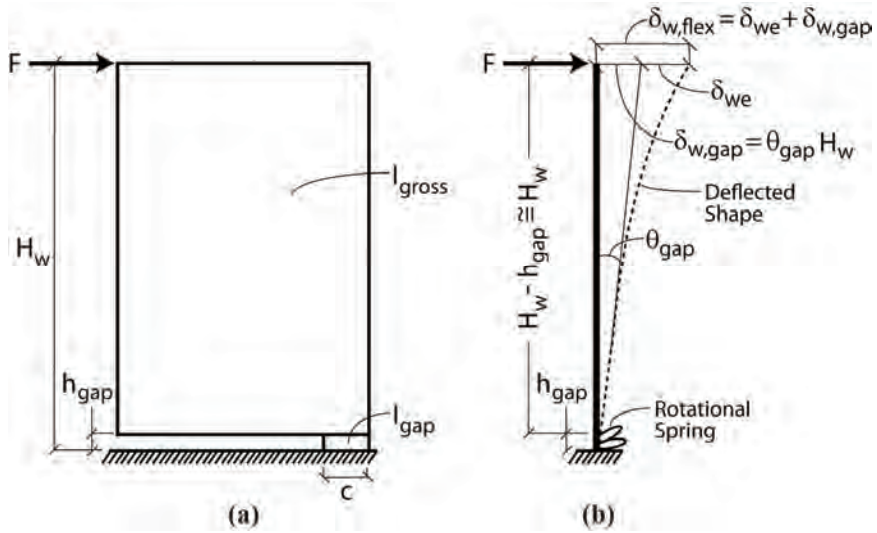

Figure 5.1 Linear-Elastic Effective Stiffness Model:
(a) Elevation View of Idealized Wall; and (b) Idealized Deflected Shape

The shear deformations of a hybrid precast concrete wall are typically considerably less than the flexural deformations. However, shear displacements should still be accounted for within the linear-elastic effective stiffness model, especially for walls with aspect ratios, H_w/L_w less than 4.0 as well as for walls with panel perforations. For design purposes, the shear displacements of the solid specimens were calculated using an effective cross-sectional shear area of A_{sh}=0.8A_{gross}, where A_{gross} is the gross area of the wall cross-section. For the perforated specimens, the effective shear area was taken as the gross cross-sectional area of only the exterior vertical chord on the compression side of the base panel (i.e., the compression vertical chord located outside of the perforations) without the 0.8 factor. The other vertical chords located on the tension side of the wall and in between the perforations do not contribute significantly to the shear stiffness; and thus, they were not included in the effective shear area. This is because the exterior vertical chord on the tension side of the wall carries only a small portion of the total wall shear force and the central chord in between the perforations undergoes extensive shear cracking, as observed from the response of the perforated specimens (shown and discussed in Chapter 6). Most of the shear stiffness of a perforated wall is provided by the compression vertical chord, which sustains relatively little cracking during the lateral displacements of the structure.

5.2 SIMPLIFIED FINITE ELEMENT MODEL

The overall modeling philosophy for the nonlinear finite element model was to create a basic analysis tool that incorporated simplifying assumptions appropriate for the design office. More information on this model, which was created using ABAQUS (Hibbitt et al. 2009) to conduct nonlinear pushover analyses of the test specimens under lateral loading combined with gravity loads, can be found in the Design Procedure Document (Smith and Kurama 2012a). As

an example, Figure 5.2 shows the exaggerated lateral displaced shape of the model for the perforated Specimen HW4. The model utilized the following features:

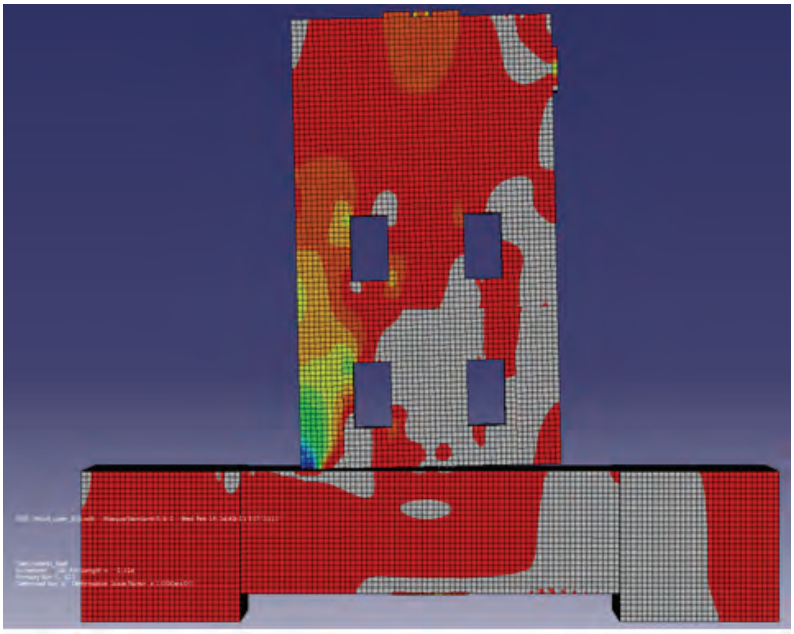

Figure 5.2 Finite Element Model of Perforated Specimen HW4

- Three-dimensional eight-node stress/displacement solid elements (type C3D8R in ABAQUS) were used for the concrete in the wall panels and the foundation.
- Three-dimensional stress/displacement truss elements (type C3D8R in ABAQUS) were used for the PT steel. The anchored ends of the PT tendons were embedded within the solid elements for the wall and foundation concrete. The initial stresses in the PT steel after all short-term and long-term losses (but before lateral displacements of the wall), f_{pi} were simulated by placing an initial tension force in the truss elements.
- Three-dimensional stress/displacement truss elements were used for the E.D. bars crossing the base joint as well as the mild steel bars crossing the upper joints. These truss elements were partitioned into bonded and unbonded regions. The bonded regions were embedded within the solid elements for the wall and foundation concrete while the

unbonded regions were not constrained, thereby allowing a uniform strain distribution to form over the unbonded length of the steel.

- "Hard contact" surfaces were used at the horizontal joints to allow for gap opening. These surfaces were defined with "rough" friction, which prevented shear slip when the surfaces were in contact.

A major simplification adopted in the model was that the bonded mild steel reinforcement contained within the wall panels and the foundation (except for the bonded regions of the reinforcement crossing the horizontal joints) was not modeled explicitly. Instead, the effect of the bonded steel reinforcement inside each wall component was captured using linear-elastic tension properties for the concrete. It was assumed (and ensured through design) that the wall panels and the foundation were reinforced with a sufficient amount of bonded mild steel to limit the size of the cracks and that this reinforcement did not yield. Note that as a result of using linear-elastic tension properties for the concrete, the redistribution of stresses due to cracking could not be modeled. However, in a properly designed and detailed hybrid precast wall with sufficient and well-distributed reinforcement, the concrete cracks remain small and do not significantly affect the global behavior of the structure. The largest "crack" in a hybrid wall is the gap that forms at the base joint, which was appropriately included in the model by using hard contact surfaces at this joint.

Additional assumptions and approximations incorporated into the finite element wall model were:

- The total unbonded length modeled for the E.D. bars included an additional length of "debonding," which was assumed to occur during a large earthquake. This increased unbonded length was assumed to remain constant from the beginning to the end of the analysis using a debonding coefficient of α_s=2.0 as described in Section 3.1.2.

- The nonlinear material properties for the concrete in compression and steel were modeled using multiple-point approximations of the measured monotonic stress-strain behaviors (utilizing both “elastic” and “plastic” regions as defined in ABAQUS).
- For the confined concrete regions at the wall toes, the confinement reinforcement was not modeled explicitly but rather represented by incorporating the effect of the confinement on the uniaxial stress-strain relationship of the concrete in compression based on Mander et al. (1988). The effects of the multi-axial stresses that developed in the three-dimensional solid elements for the concrete were ignored.
- The grout pads at the horizontal joints were not modeled explicitly. Instead, the grout thickness was modeled as part of the wall panels assuming that the grout and panel concrete behaved similarly.

5.3 DETAILED FIBER ELEMENT MODEL

The fiber element model described in this section is a research tool to conduct nonlinear reverse-cyclic and dynamic response history analyses of hybrid walls under seismic loading. The model was developed based on a previous study by Kurama (2002, 2005), where more information can be found. The goal was to accurately reproduce the hysteretic behavior of the test specimens including gap opening/closing at the horizontal joints and hysteretic stress-strain behaviors for the materials. As an example, Figure 5.3 shows a schematic of the fiber element model for one of the solid specimens. The analysis of walls with perforations followed a similar approach by removing the concrete fibers from the perforated regions of the wall panels; however, it should be noted that unlike the finite element model described in Section 5.2, the fiber element model was not capable of capturing the local behavior around the perforations. The model, created using DRAIN-2DX (Prakash et al. 1993), utilized the following features:

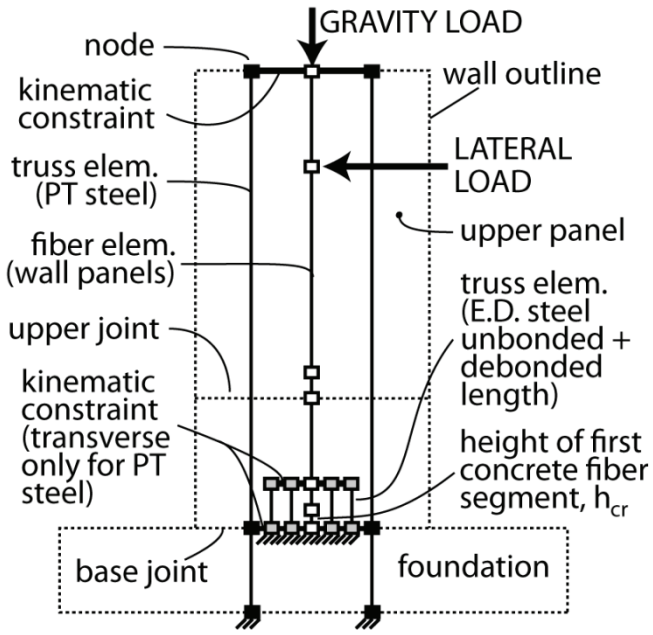

Figure 5.3 Fiber Element Model of a Hybrid Wall

- Fiber beam-column elements were used to represent the axial-flexural behavior of the precast wall panels. The shear stiffness of the panels was assumed to remain constant at the effective stiffness given by the linear-elastic effective stiffness model described in Section 5.1.
- The foundation was assumed to be fixed. To simulate the effect of gap opening at the base joint, the tension strength of the concrete fibers at the bottom of the base panel was set to zero over a height, h_{cr}, which was taken as the confined concrete thickness of the wall. Outside these regions, the wall concrete was assumed to be linear-elastic in tension (i.e., similar to the finite element model, the cracking of the concrete was ignored and the bonded mild steel reinforcement contained within each wall panel was not modeled explicitly).
- Truss elements were used for the unbonded PT steel. The PT anchors were modeled by kinematically constraining the ends of the truss elements to corresponding fiber element

nodes for the wall panels at the same elevation. The initial PT stresses were simulated by placing an initial tension force in the truss elements.

- The unbonded regions of the E.D. bars were also modeled using truss elements so as to capture the uniform strains over the unbonded length of the steel. Similar to the finite element model, an additional debonding length was incorporated into the total unbonded length modeled for the E.D. bars. This increased unbonded length was assumed to remain constant throughout the analysis. The bonded regions of the bars were modeled by kinematically constraining the end nodes of the truss elements to corresponding fiber element nodes for the wall panels at the same elevation (the actual bonded lengths of the E.D. bars were not modeled).
- Similar to the base joint, the effect of any gap opening at the upper panel-to-panel joints (albeit small) was modeled by using "compression-only" material properties for the concrete fibers (i.e., the tension strength of the concrete was taken as zero) over a short height at the bottom of each upper wall panel. The compression-only concrete fibers above each panel-to-panel joint extended over a height equal to the unbonded length of the mild steel bars crossing the upper joints. Even though these mild steel bars were not bonded to the concrete, they were modeled as part of the fiber cross section representation of these regions. Concrete with linear-elastic tension properties was used to model the remaining height of each wall panel.

The concrete under compression was modeled using a multiple-point approximation of the measured uniaxial stress-strain behavior. For the confined concrete regions at the wall toes, the confinement reinforcement was not modeled explicitly, but was represented by incorporating the effect of the confinement on the concrete compression stress-strain relationship based on Mander et al. (1988). The grout pads at the horizontal joints were also not modeled explicitly.

Instead, the grout thickness was modeled as part of the wall panel concrete assuming that the grout and the panel concrete behaved similarly.

The behavior of the steel reinforcement crossing the horizontal joints was also modeled using a multiple-point approximation of the measured stress-strain behavior. For the E.D. bars at the base, a nonlinear material model up to the largest expected strain, ε_{sm}, at Δ_{wm} was used. As an example, Figure 5.4(a) shows the cyclic E.D. steel stress-strain relationship used in the modeling of Specimen HW1. The mild steel bars across the upper panel-to-panel joints can be modeled as linear-elastic; however, the resulting steel strains should be checked to ensure that the yield strain is not exceeded. The nonlinear behavior of the PT steel was modeled up to the largest expected strain, ε_{pm}, at Δ_{wm} so as to capture the nonlinear stresses as well as the cyclic prestress losses in the tendons. The strand stiffnesses from the measured material stress-strain relationship in Figure 4.10 were reduced to account for the localized concrete and anchorage deformations at the tendon ends, since these local deformations could not be captured by the fiber elements modeling the wall panels. As shown in Figure 5.4(b), this was done by reducing the initial strand stiffness in the linear-elastic range by a factor of 0.75 and by reducing the stress at ε_{pm} by a factor of 0.85.

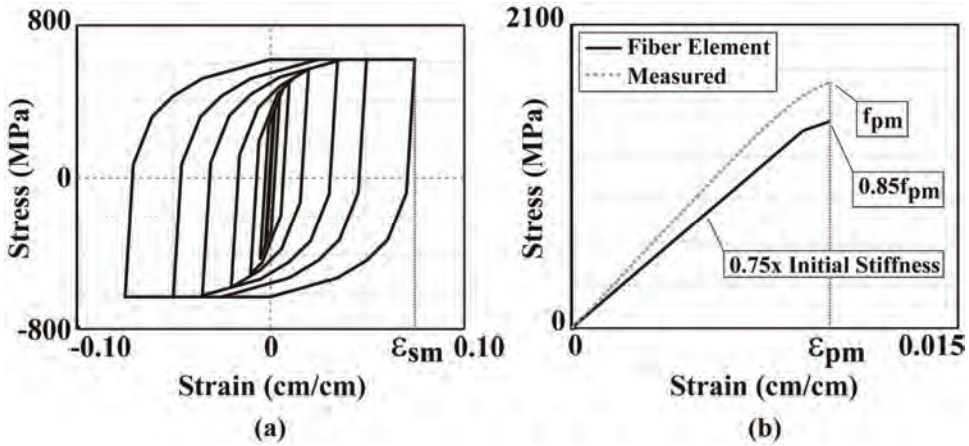

Figure 5.4 Material Stress-Strain Models: (a) E.D. Steel; (b) PT Steel

This page intentionally left blank.

CHAPTER 6

OVERALL BEHAVIOR OF TEST SPECIMENS

This chapter summarizes the measured overall behavior of the six wall specimens tested in this project, specifically the base shear force versus wall drift behavior (both measured and analytical responses), observed damage, and failure mechanism. More information on the results from the tests can be found in Chapter 7.

6.1 OVERVIEW OF SPECIMEN PERFORMANCE

Figure 6.1 shows the reversed-cyclic lateral displacement history applied in the testing of the wall specimens, with three repeated cycles at each displacement increment. The wall drift, Δ_w (positive with the wall displaced southward), was measured as the relative lateral displacement of the wall between the lateral load location and the top of the foundation divided by the height to the lateral load. For the given wall dimensions, the prescribed validation-level drift per ACI ITG-5.1 for each specimen was Δ_{wc}=2.30% from Eqn. 2.1, which was also used as the maximum-level drift, Δ_{wm} in design.

From Figure 6.1, it can be seen that Specimens HW1 and EW failed to reach the validation-level drift. While Specimens HW2 and HW5 reached the validation-level drift, neither specimen was able to sustain three loading cycles without losing excessive strength (as described in Section 2.3, ACI ITG-5.1 prescribes no more than 20% loss in peak lateral resistance during each set of three loading cycles beyond the overall peak lateral strength). In comparison, Specimens HW3 and HW4 satisfied the entire required drift history. Specimen HW3 was able to sustain two cycles at the validation-level drift followed by a greater drift cycle of Δ_w=±2.95%.

Specimen HW4 was able to sustain three cycles at the validation-level drift followed by an additional set of three cycles at Δ_w=±3.05%.

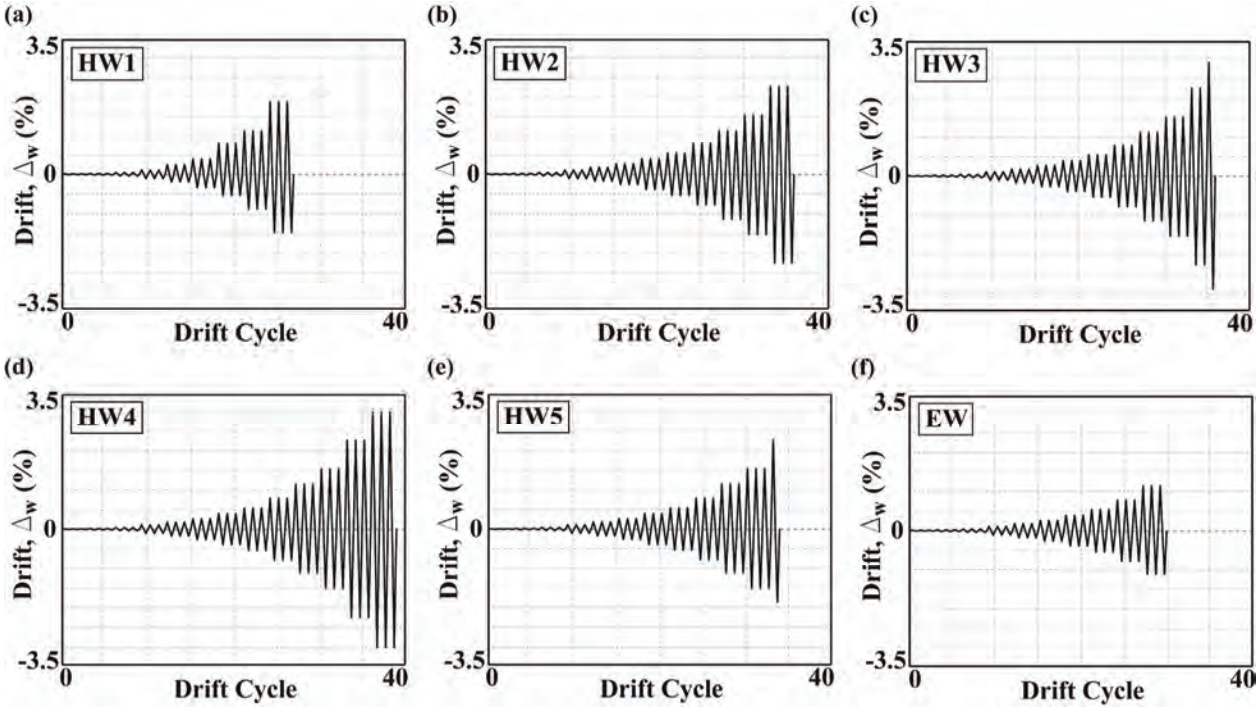

Figure 6.1 Applied Wall Drift History: (a) Specimen HW1; (b) Specimen HW2; (c) Specimen HW3; (d) Specimen HW4; (e) Specimen HW5; and (f) Specimen EW

Each specimen was tested until failure was either imminent (Specimens HW3 and HW4) or had occurred (Specimens HW1, HW2, HW5, and EW). Figure 6.2 shows photographs of the specimens during the final positive loading cycle of the displacement history (note the gap opening along the base joint at the north end of each wall). Figure 6.3 shows the measured base shear force, V_b versus wall drift, Δ_w behavior of each specimen while Figure 6.4 shows the corresponding analytical V_b-Δ_w behaviors predicted by the fiber element and finite element models. Note that while fiber element models were created to study the behavior of all six specimens, finite element models were created only for Specimens HW3, HW4, and HW5, primarily for monotonic analysis up to the validation-level drift, Δ_{wc} during the design of the walls. The fiber element models were subjected to the reversed-cyclic lateral displacement

histories in Figure 6.1, except only one cycle was applied at each drift level. The overall performance and failure mechanism of each wall are discussed below in more detail. More information comparing specific measured behaviors of the specimens can be found in Chapter 7.

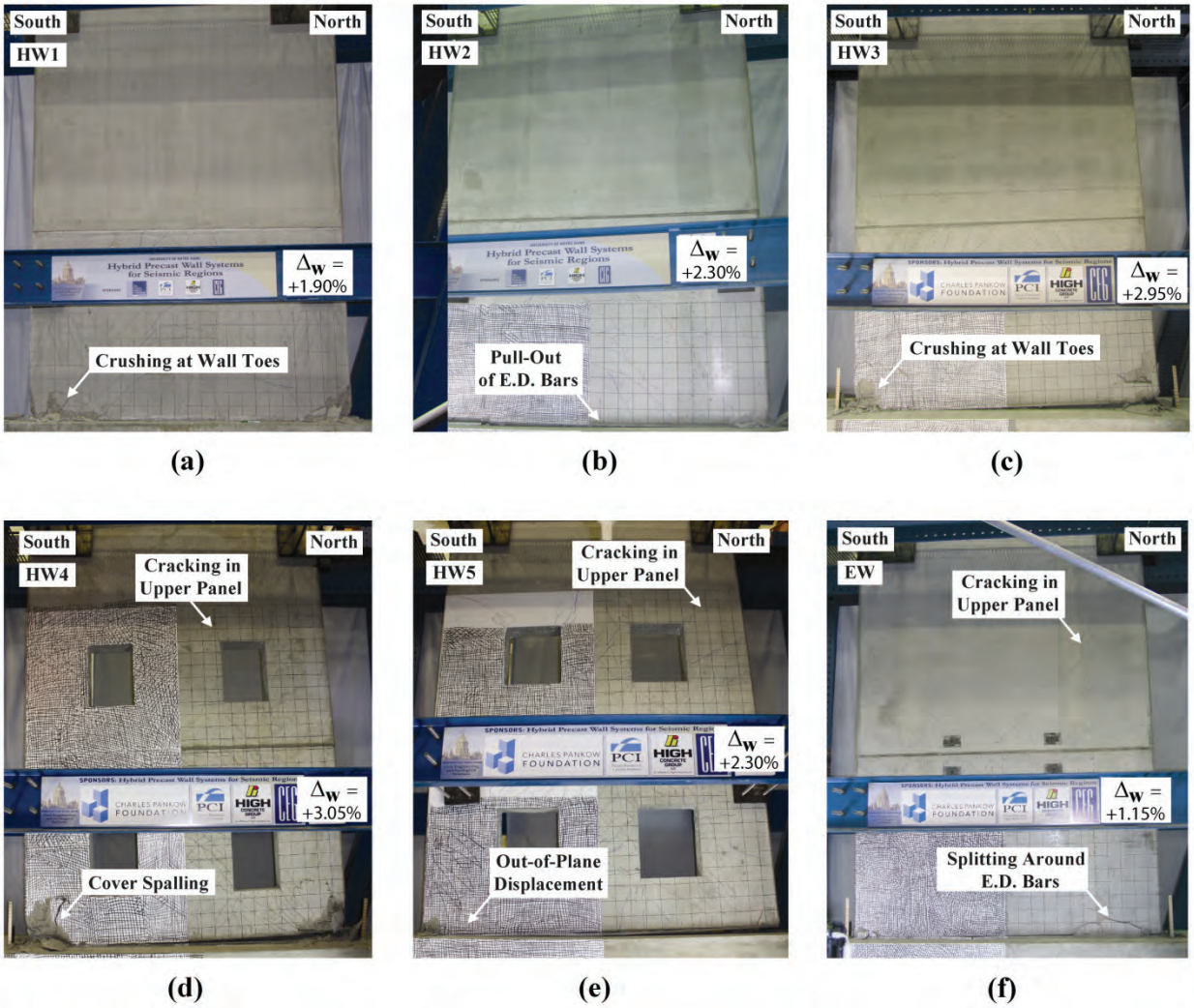

Figure 6.2 Observed Damage: (a) Specimen HW1 at 3rd Cycle of Δ_w=+1.90%; (b) Specimen HW2 at 3rd Cycle of Δ_w=+2.30%; (c) Specimen HW3 at 1st Cycle of Δ_w=+2.95%; (d) Specimen HW4 at 3rd Cycle of Δ_w=+3.05%; (e) Specimen HW5 at 1st Cycle of Δ_w=+2.30%; (f) Specimen EW at 3rd Cycle of Δ_w=+1.15%

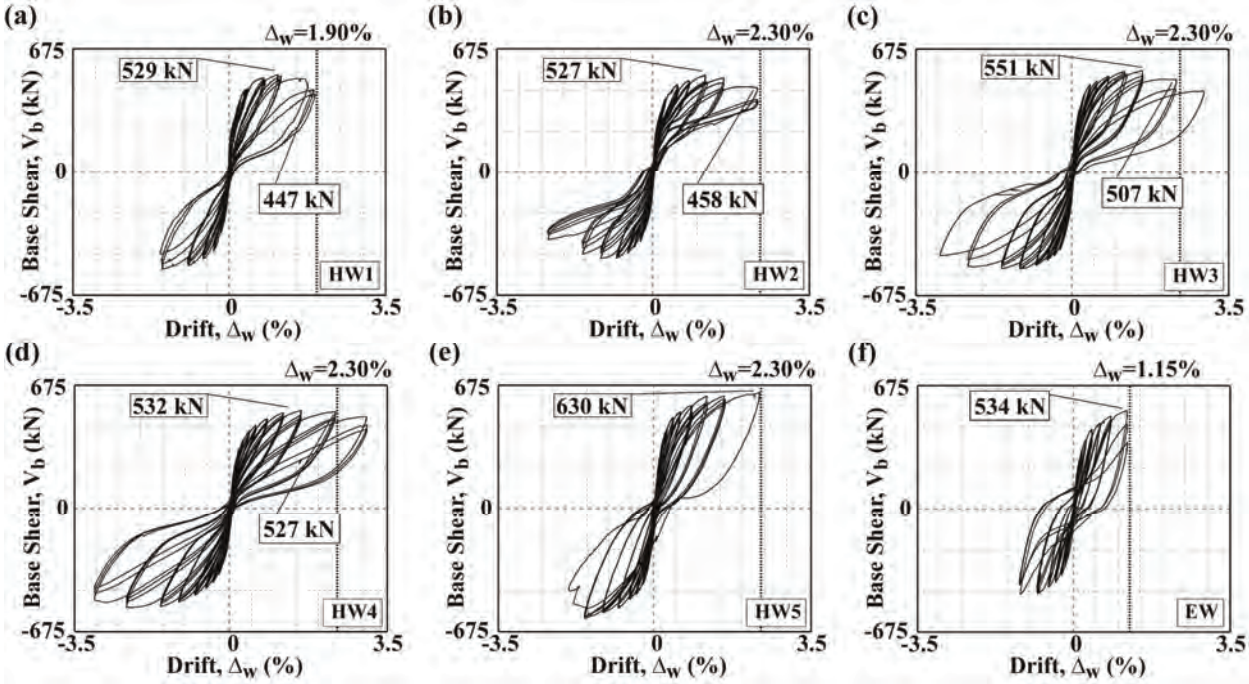

Figure 6.3 Measured Base Shear Force versus Wall Drift Behavior: (a) Specimen HW1; (b) Specimen HW2; (c) Specimen HW3; (d) Specimen HW4; (e) Specimen HW5; (f) Specimen EW

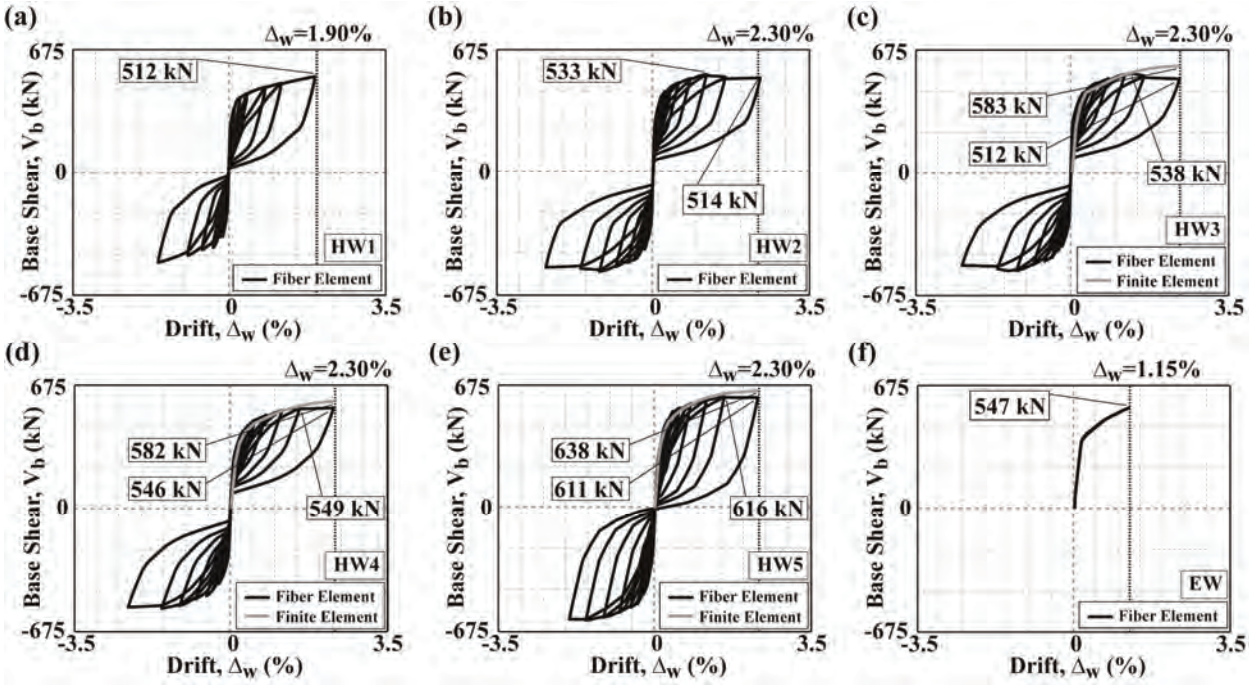

Figure 6.4 Fiber Element and Finite Element Analytical Base Shear Force versus Wall Drift Behaviors: (a) Specimen HW1; (b) Specimen HW2; (c) Specimen HW3; (d) Specimen HW4; (e) Specimen HW5; (f) Specimen EW

6.2 SPECIMEN HW1: SOLID HYBRID WALL

Specimen HW1 was able to sustain three cycles at a maximum positive wall drift of Δ_w=+1.90% and a maximum negative drift of Δ_w=-1.55% prior to failure due to the crushing of the confined concrete at the toes [see Figure 6.2(a)]. The compressive strength of the concrete used in the base panel of this wall did not achieve the specified design strength [33-MPa (4.8-ksi) test-day strength compared to the specified design strength of 41-MPa (6.0-ksi)]. Furthermore, during the casting of the specimen, the first confinement hoop was placed at a significant angle with the bottom edge of the base panel, resulting in a large region of unconfined concrete at the bottom of wall [at the east face of the south end of the panel, the first hoop was located 11.4-cm (4.5-in.) from the bottom rather than the design location of 5.0-cm (2.0-in.)]. While not as extreme as the south toe, the hoop placement at the north toe was also misaligned. This misalignment of the confinement hoops, combined with the low unconfined concrete strength of the critical base panel, resulted in the failure of the wall at a lower drift than the validation-level drift of ±2.30% that the wall was designed to achieve.

The fabrication and construction of the confinement steel cages for Specimen HW1 were done in a precast production plant in order to replicate realistic casting conditions. However, the relatively small dimensions for the 0.40-scale confinement hoops posed difficulty in achieving accurate dimensions during the fabrication of the wall panels, causing the misalignment of the hoops. As a result, the confinement hoops and the associated confinement cages for Specimens HW2-HW5 and Specimen EW were constructed in the laboratory at Notre Dame in advance of the casting, resulting in superior quality control.

The initiation of cover concrete spalling in Specimen HW1 occurred during the Δ_w=±0.80% drift cycles [see the south toe of the wall in Figure 6.2(a)], after the design-level drift of Δ_{wd}=±0.70% was exceeded. Significant crushing of the confined concrete at the wall

toes was not present until about Δ_w=+1.75% (final drift series), after which strength degradation was evident as reflected by the V_b-Δ_w behavior during the 2nd and 3rd cycles at Δ_w=+1.90% in Figure 6.3(a). Note that the specimen was loaded in a slightly unsymmetrical manner due to the movement of the foundation beam during the test; however, all data has been corrected to isolate the wall response from this foundation movement. The failure of the wall can be seen in the hysteretic behavior, as the specimen sustained a 20% strength loss in the positive direction during the Δ_w=+1.90% drift cycles. While the design clear cover was 1.3-cm (0.50-in.) for the welded wire fabric placed on each face of the wall, the actual clear cover was as little as 0.38-cm (0.15-in.) near the south end of the base panel. This resulted in the delamination of the wire fabric and the adjacent concrete cover near the end of the test. The damage to the wall was limited to the base panel, with no concrete cracking or crushing in the upper panel and no significant gap opening or horizontal shear slip in the upper panel-to-panel joint.

As shown in Figure 6.4(a), the fiber element model yielded a similar load displacement behavior as the measured behavior in Figure 6.3(a), with comparable peak forces at both the early and late cycles. The analytical model estimated slightly lower base shear forces than the measured forces during the early cycles. This may be explained by the fluctuating increases [between 14-MPa (2-kips) and 55-MPa (8-kips)] that occurred in the externally applied wall gravity load during these cycles. In the analytical model, the wall gravity load was held constant throughout the analysis, resulting in slightly lower base shear forces as compared with the test specimen. The fluctuations in the applied gravity load were prevented during the later cycles of the test. It can also be seen in Figure 6.4(a) that the analytical model was considerably stiffer than the measured behavior during the unloading of the wall. This occurred due to the discrepancies in the modeling of the Bauschinger effect during the unloading of the E.D. steel reinforcement at the wall base [see Figure 5.4(a)].

6.2.1 Damage Progression in Specimen HW1

Figure 6.5 shows front face photographs of the south end of the wall at Δ_w=+0.25% (3rd cycle), +0.40% (1st cycle), and +0.80% (1st cycle) along with the corresponding vertical (i.e., axial) strains from the 3D-DIC data measured at the back face. Data drops in the strain plots (i.e., white regions of the plots) are locations where conventional sensors were mounted to the wall, obstructing the field of view of the 3D-DIC cameras placed at the back of the specimen in this test. Compression strains of -1525 micro-strain are evident at the toe of the wall at Δ_w=+0.25%. Clearly visible in these images are increased axial strains (-1960 micro-strain; a value associated with yield in mild steel reinforcement) and diagonal cracks terminating in the plastic hinge region of the base panel as the wall is pushed to Δ_w=+0.80%.

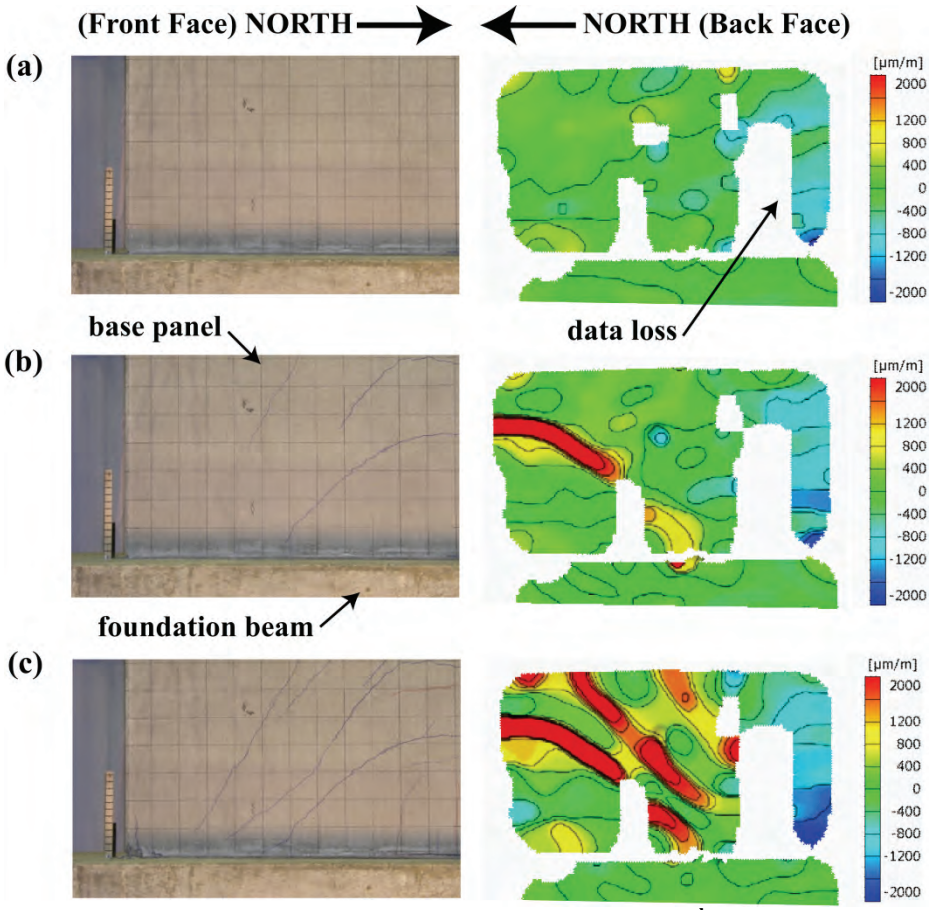

Figure 6.5 Progression of Damage in Specimen HW1: (a) 3rd Cycle at Δ_w=+0.25%; (b) 1st Cycle at Δ_w=+0.40%; (c) 1st Cycle at Δ_w=+0.80%

As shown by both the photographs and the strain plots, cracking initiated during the 1st cycle to Δ_w=+0.40%. The 3D-DIC system was able to capture the initiation and location of the cracks with excellent accuracy. Note that the dark (red) shaded regions in the strain plots are not indicative of the crack widths, which remained small throughout the test (the cracks visible in the photographs were highlighted with markers during the test for enhanced viewing). Further, any small differences between the crack patterns in the photographs and those in the strain plots can be explained by differences in the crack locations between the front and back faces of the wall.

6.3 SPECIMEN HW2: SOLID HYBRID WALL

Modifications to the concrete mix as well as the fabrication and placement of the confinement cages were implemented in Specimen HW2 based on the observed performance of Specimen HW1. Specimen HW2 was ultimately subjected to three fully-reversed displacement cycles at the ±2.30% validation-level drift; however, the strength and energy dissipation of the structure during the three cycles at this displacement did not satisfy ACI ITG-5.1. Failure of the specimen occurred prior to the validation-level drift, during the Δ_w=±1.55% cycles, when the E.D. bars pulled out from the ACI 318 Type II mechanical splice connectors (permitted by ACI ITG-5.2) placed inside the foundation due to failure of the grout within the connectors. These connectors provided ease of erection; however, pullout of the E.D. bars caused the steel elongations and strains to be smaller than designed, resulting in smaller lateral strength and energy dissipation of the wall.

The loss of energy dissipation (but not the restoring capability) in Figure 6.3(b) is evidence of the failure of the E.D. bars. Using the measured PT steel stresses, applied gravity load, and neutral axis length (together with the ACI 318 and ACI ITG-5.2 concrete stress blocks) at the final drift cycle of Δ_w=+2.30%, the lateral strength of the wall ignoring the contribution of

the mild steel was estimated to range from 358-kN (80.5-kips) to 371-kN (83.4-kips). Comparing this range with the measured strength of 385-kN (86.6-kips), it was confirmed that Specimen HW2 was essentially behaving as a fully post-tensioned wall by the end of the test. The predicted V_b-Δ_w behavior of Specimen HW2 using the fiber element analytical model is depicted in Figure 6.4(b). It can be seen that there are significant discrepancies, which occurred because the pullout of the E.D. bars was not modeled analytically.

It should be noted that the grout used in the E.D. bar splice connectors satisfied the splice manufacturer's specifications and the splice itself satisfied the performance requirements in ACI 318 (2011) and AC133 (ICC, 2010) for Type II mechanical connectors. The reason for the splice failure was therefore that the E.D. bars in the wall specimens were subjected to greater strains and over a significantly larger number of cycles than required to classify a Type II connection according to ACI 318 and AC133. The same mechanical connectors with similar splice grout strengths (see Table 4.2) were used in Specimen HW1 with no bar pullout. A possible reason that E.D. bar pullout did not occur in Specimen HW1 is the lower concrete strength of the base panel [33-MPa (4.8-ksi) on test day in Specimen HW1 versus 44-MPa (6.5-ksi) in Specimen HW2], which increased the neutral axis length at the base joint during the larger displacements of the wall (as described in Section 7.5), possibly resulting in decreased E.D. bar strains

As with Specimen HW1, the damage to Specimen HW2 was limited to the base panel, with no concrete cracking or crushing in the upper panel and no significant gap opening or horizontal shear slip in the upper panel-to-panel joint [see Figure 6.2(b)]. Cracking in the base panel initiated during the 3rd cycle to Δ_w=-0.27% and remained small throughout the test. This drift cycle is smaller than the drift cycle (Δ_w=+0.40%) during which cracking was observed in Specimen HW1. However, this does not necessarily mean that the initiation of cracking occurred earlier in Specimen HW2, since the foundation movement during the testing of Specimen HW1

resulted in different wall displacement histories between these two specimens [see Figures 6.1(a) and 6.1(b)]. The initiation of cover concrete spalling in Specimen HW2 occurred during the Δ_w=±0.80% drift cycles (compared to the Δ_w=±0.40% drift cycles in Specimen HW1). This improvement was related to the higher base panel concrete strength as well as the use of No. 10 (U.S. No. 3) bars instead of welded wire fabric for the panel distributed reinforcement (see Figures 4.2 and 4.3), which allowed for more consistent cover concrete thickness in Specimen HW2. Crushing of the confined concrete at the wall toes was not observed in Specimen HW2, which was another improvement compared to the performance of Specimen HW1, where confined concrete crushing initiated during the Δ_w=±1.15% drift cycles. The better performance of the confined concrete was related to: (1) closer placement of the first confinement hoop to the bottom of the base panel in Specimen HW2; (2) smaller compressive forces at the wall toes due to the pullout (i.e., smaller tension forces) of the E.D. bars; and (3) higher base panel concrete strength.

6.4 SPECIMEN HW3: SOLID HYBRID WALL

Based on the observed pullout failure in Specimen HW2, the E.D. bars in Specimen HW3 were designed using the full development length projecting beyond the bottom of the base panel (see Figure 4.4) and grouted into corrugated metal ducts cast within the foundation beam instead of Type II mechanical splice connectors. As a result, Specimen HW3 was able to sustain two fully-reversed drift cycles at Δ_w=±2.30% (i.e., the validation-level drift) followed by a greater drift cycle of Δ_w=±2.95%. The specimen behaved in a reasonably symmetrical manner in the positive and negative directions, while also exhibiting excellent re-centering and considerable energy dissipation [see Figure 6.3(c)]. While crushing of the confined concrete was observed at the wall toes [see Figure 6.2(c)], the total strength loss from the overall peak base shear strength

recorded during the test to the peak resistance during the final drift cycle at Δ_w=±2.95% was approximately 19.9% and 13.8% in the positive and negative directions, respectively, which are both within the 20% strength loss limit prescribed by ACI ITG-5.1. The measured stiffness losses were also within the prescribed limitations per ACI ITG-5.1.

Specimen HW3 was analyzed using both the fiber element and the finite element models. As shown in Figure 6.4(c), both models matched the measured behavior reasonably well. The monotonic analysis using the finite element model did not predict the measured strength loss of the specimen during the large displacements. This strength loss, which was primarily due to the damage that occurred in the confined concrete region of the wall, was captured by the fiber element model. A small discrepancy occurred in the unloading portion of the V_b-Δ_w behavior from the fiber element model, as the analysis predicted no residual displacement (i.e., displacement of the wall after the lateral load is removed) while some residual displacement was measured in the test specimen. This discrepancy was related to the PT stress losses that occurred during the test (as described in Section 7.3) due to a small amount of nonlinear straining in the strand-anchorage system. These losses were not fully captured by the analytical model. Note that despite the PT losses, the measured residual drift of the wall at the end of the test was still negligible.

Similar to Specimens HW1 and HW2, damage in Specimen HW3 was limited to the base panel. Cracking in the base panel initiated during the 1st cycle to Δ_w=+0.55% (the design-level drift for the wall), which is later than in Specimens HW1 and HW2. The initiation of cover concrete spalling in Specimen HW3 occurred during the Δ_w=±0.80% drift cycles. Significant crushing of the confined concrete at the wall toes was not present until about Δ_w=+2.30%, after which strength degradation was evident as reflected by the V_b-Δ_w behavior [see Figure 6.3(c)]. During the larger displacement cycles, the terminated ends of the distributed horizontal No. 10

(U.S. No 3) panel reinforcement started to delaminate from the wall at the base, accelerating the progression of concrete spalling along the wall length. Because of the relatively small thickness of the 0.40-scale specimen, these bars had a design clear cover of only 1.27-cm (0.5-in.) and were terminated outside the confinement cages on either face of the panel. Upon spalling of the concrete cover, the terminated ends of the horizontal bars at the wall toes became exposed, causing delamination.

Near the completion of the test, outward bowing of the longer, horizontal legs of the confinement hoops was observed at the wall toes (the hoops had a relatively large length-to-width ratio of l_{hoop}/w_{hoop}=3.56, as shown in Figure 4.5). While a crosstie was present within the confinement detailing, this tie did not directly engage the hoop. Rather, as permitted by ACI 318 (2011), each crosstie and hoop separately engaged the vertical bars within the confinement cage, making the tie ineffective to prevent the longitudinal legs of the hoop from bowing out.

6.5 SPECIMEN HW4: PERFORATED HYBRID WALL

Specimen HW4 was essentially identical to Specimen HW3, except for the perforations within the wall panels and modifications to the reinforcement at the toes of the base panel. As previously mentioned, the confinement reinforcement in Specimen HW3 consisted of a large rectangular hoop (where l_{hoop}/w_{hoop}=3.56) with an intermediate crosstie located at the mid-length of the hoop. Further, the horizontal distributed 10-mm (U.S. No. 3) deformed bars at each face of the base panel were placed outside of the confinement cages for ease of construction. In Specimen HW4, the confinement reinforcement consisted of two smaller hoops (where l_{hoop}/w_{hoop}=2.22 as shown in Figure 4.6) that were overlapped to create a larger overall confined region length. This modification was made primarily to reduce confined concrete damage (which was observed in Specimen HW3 in part due to the bowing-out of the longer legs of the bottom

hoops) and secondarily for ease of construction by matching the outside dimensions of the confinement cages to the dimensions of the shear hoops in the exterior vertical chords of the perforated base panel [see Figure 4.8(b)]. Additionally, the horizontal distributed 10-mm (U.S. No. 3) deformed bars were placed inside of the confinement cages in an attempt to limit the delamination of the bars upon spalling of the concrete cover.

As shown in Figure 6.3(d), the specimen sustained three cycles at the validation-level drift followed by an additional set of three cycles at a drift of Δ_w=±3.05%. As in Specimen HW3, the total strength loss in Specimen HW4 at the completion of the drift history was less than 20%, thus satisfying the ACI ITG-5.1 requirement for validation. The damage to the wall was mostly concentrated in the base panel [see Figure 6.2(d)], consisting of distributed cracks predominately in the horizontal chord members (both above and below the perforations) and in the center vertical chord (in between the perforations). Limited cracking in the upper panel was observed, concentrated at the corners of the perforations. Cover spalling was observed at both wall toes; however, crushing of the confined concrete was only beginning to develop during the last set of drift cycles at Δ_w=±3.05%. The improved performance of the confined concrete was related to the modifications made to the confinement steel detailing, specifically through the use of two shorter hoops instead of one long hoop and an intermediate tie. The reduction in the confinement hoop length-to-width ratio prevented the out-of-plane bowing of the longer hoop legs, thus maintaining the confining pressure. Further, terminating the distributed horizontal 10-mm (U.S. No. 3) bars inside the confinement cages prevented the delamination of these bars from the wall, and thus, limited the extent of the cover concrete spalling. No concrete crushing in the upper panel and no significant gap opening or slip in the upper panel-to-panel joint was observed during the test.

Specimen HW4 behaved in a reasonably symmetrical manner in the positive and negative directions, while also exhibiting excellent re-centering capability and considerable (but reduced) energy dissipation [see Figure 6.3(d)]. The total strength losses were approximately 18.9% and 18.7% in the positive and negative directions, respectively, and the measured stiffness losses were within the prescribed limitations per ACI ITG-5.1, thereby satisfying the validation criteria. Based on the general similarities between the overall load-displacement behaviors of Specimens HW3 and HW4 [see Figures 6.3(c) and 6.3(d)], the presence of the panel perforations did not significantly impact the global behavior of the structure, thus validating the design of the panel reinforcement around the perforations. The increased flexibility and reduced energy dissipation of Specimen HW4 as compared with Specimen HW3 (visible in Figure 6.3) were likely due to the increased shear deformations of the perforated wall panels as discussed in Section 7.6.

As shown in Figure 6.4(d), both the fiber element and finite element analytical models matched the envelope of the measured V_b-Δ_w behavior quite well. However, the fiber element results did not accurately predict the individual hysteretic loops. The degradation of the loading stiffness (i.e., the decrease in the lateral stiffness of the wall during the large displacement cycles as compared to the stiffness during the earlier cycles) was underestimated by the fiber element model. This discrepancy was likely due to the inability of the model to capture the nonlinear shear deformations of the perforated wall panels. In addition, the unloading portion of the predicted V_b-Δ_w behavior had no residual displacement while some residual displacement was measured in the test specimen. Similar to Specimen HW3, this discrepancy was related to the PT stress losses that occurred during the test (described in Chapter 7) due to a small amount of nonlinear straining of the strand-anchorage system. Note that despite the PT losses, the measured residual drift of the wall at the end of the test was still negligible.

6.6 SPECIMEN HW5: PERFORATED HYBRID WALL

Specimen HW5 incorporated longer perforations [43-cm (17-in.) long by 51-cm (20-in.) tall] than in Specimen HW4 [36-cm (14-in.) by 51-cm (20-in.)]. In addition, the ratio of PT steel area to E.D. steel area was reduced to investigate the contribution of the E.D. steel to the total base moment strength of the structure. To partially compensate for the loss of restoring force due to the reduced PT steel area, a larger external axial load was applied to Specimen HW5 [534-kN (120-kips)] than the load on the other test specimens [325-kN (73-kips)]. The larger axial load represented an increased gravity load applied to the prototype wall, which was possible by considering an alternate location for the interior gravity columns (thus increasing the tributary area for the prototype wall). Finally, the E.D. bars were distributed along the length of the wall rather than concentrated near the wall centerline in an attempt to explore the range of possible locations for the reinforcement.

Failure of Specimen HW5 occurred during the 1st cycle of Δ_w=-2.30% as the wall sustained a strength loss greater than 20% [see Figure 6.3(e)]. The failure occurred due to the reduced PT steel and increased E.D. steel in the wall. Upon unloading of the wall from significant tensile yielding of the E.D. steel, the axial (i.e., vertical) restoring force was not sufficient to yield the E.D. bars back in compression and close the gap at the base joint. This resulted in a residual gap along the entire length of the joint when the wall was returned back to Δ_w=0% (i.e., the wall was uplifted from the foundation at the Δ_w=0% position). As described in Section 7.7, the amount of uplift increased rapidly during successive loading/unloading cycles with increased displacement. Ultimately, upon unloading from the 1st cycle of Δ_w=-2.30%, the wall failed through large out-of-plane displacements at the base and buckling of the E.D. bars in compression.

Figure 6.4(e) shows that the analytical models provided a reasonable match to the measured behavior. Similar to Specimen HW4, the fiber element model underestimated the degradation of the loading stiffness in Specimen HW5, which was likely due to the inability of the model to capture the nonlinear shear deformations of the perforated wall panels. As described in Section 7.8, Specimen HW5 also experienced increased in-plane horizontal shear slip along the base joint, which was not modeled.

Prior to failure, the observed concrete cracking in Specimen HW5 was similar to that in Specimen HW4 [see Figure 6.2(e)]. The damage was mostly concentrated in the base panel, consisting of distributed cracks predominately in the horizontal chord members (both above and below the perforations) and in the center vertical chord (in between the perforations). Limited cracking in the upper panel was observed, concentrated at the corners of the perforations. Cover spalling was observed at both wall toes; however, crushing of the confined concrete was not observed (as the confinement reinforcement detailing used in Specimen HW5 was similar to the improved detailing in Specimen HW4). No significant slip or gap opening was observed in the upper panel-to-panel joint.

6.7 SPECIMEN EW: SOLID EMULATIVE WALL

The emulative Specimen EW, which was tested to provide a baseline comparison for the hybrid walls, failed after only three drift cycles to Δ_w=±1.15% [see Figure 6.3(f)]. The strength loss from the overall peak base shear strength to the peak resistance during the 3rd cycle to Δ_w=+1.15% was 32.5%, which was larger than the 20% strength loss limit prescribed by ACI ITG-5.1. The loss in the base shear resistance in the negative loading direction was smaller (11.1%). Until the tensile yielding of the E.D. bars crossing the base joint, the emulative wall behaved similar to the hybrid walls (with the exception of more widespread hairline cracking in

the emulative system). However, failure of the emulative specimen occurred relatively early due to the uplift of the wall from the foundation (similar to but larger than that observed in Specimen HW5). Upon unloading from tensile yielding of the E.D. bars, the re-centering capability of the emulative wall was limited. Without the PT force, the restoring effect of the 325-kN (73-kips) tributary gravity load applied at the top of the wall and the 37.8-kN (8.5-kips) self-weight of the specimen was not sufficient to yield the bars back in compression and close the gap at the base joint. This resulted in a residual gap along the entire length of the joint when the wall returned to Δ_w=0%. Upon reloading, the nonlinear behavior and failure of the specimen was dominated by excessive in-plane horizontal shear slip at the base joint, with relatively small gap opening as compared to the hybrid specimens. The behavior of the wall in the positive and negative directions was somewhat unsymmetrical, which occurred due to different amounts of slip in the two directions.

While the crack widths in the wall panels generally remained small [see Figure 6.2(f)], the cracking in Specimen EW was considerably more extensive than in the solid hybrid walls and extended high into the upper panel. Cracking of the wall initiated during the 1st cycle to Δ_w=+0.13%, which is well before the design-level drift of Δ_{wd}=0.60% and prior to the cracking of the hybrid specimens. The initiation of cover concrete spalling did not occur until the 1st cycle to Δ_w=+1.15%, but significant deterioration to the concrete at the wall toes progressed rapidly (and earlier than in the hybrid specimens), resulting in large strength and stiffness degradation [see Figure 6.3(f)]. Under load reversal with increasing slip, the concrete around the E.D. bars began to deteriorate due to the shear force transfer from the bars to the surrounding concrete, eventually resulting in localized splitting of the base panel around the bars. Similar to the hybrid specimens, no significant slip or gap opening was observed in the upper panel-to-panel joint.

The fiber element analytical model of the emulative Specimen EW [shown in Figure 6.6(a)] was subjected to a monotonic lateral pushover analysis rather than the fully-reversed cyclic displacement history used during the experiment. The cyclic loading history could not be replicated in the analysis due to the residual gap (uplift) that formed along the base joint, resulting in numerical convergence problems. Since the horizontal shear slip at the base-panel-to-foundation joint of the emulative wall was significantly larger than the slip in the hybrid walls (discussed in Section 7.8), a zero-length connection element was incorporated into the fiber element model to allow for slip to occur along the base [see Figure 6.6(b)]. An idealized bilinear shear force-slip relationship was used in the connection element based on the measured shear force-slip behavior of Specimen EW. Figure 6.4(f) shows that the analytical results provided a reasonable match to the envelope of the measured V_b-Δ_w behavior of the structure.

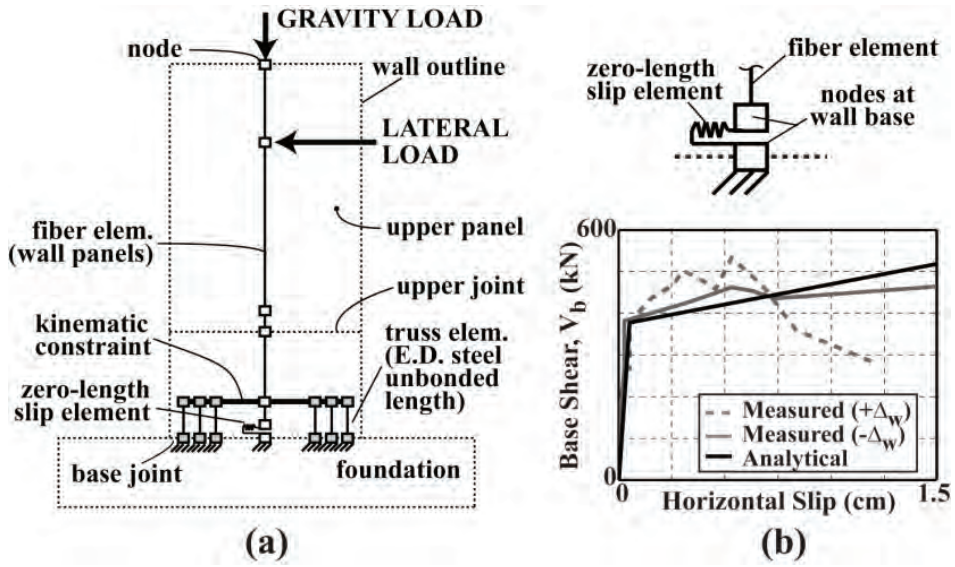

Figure 6.6 Fiber Element (DRAIN-2DX) Modeling of Emulative Specimen EW: (a) Model Elevation; (b) Zero-Length Slip Element at Wall Base

CHAPTER 7

COMPARISON OF SELECTED SPECIMEN RESPONSE PARAMETERS

This chapter summarizes and compares important response parameters for the test specimens, specifically the energy dissipation, E.D. steel bar strains, PT steel stresses, vertical gap opening displacements and neutral axis length (i.e., contact length) along the base-panel-to-foundation joint, panel shear deformations, residual wall uplift, horizontal shear slip along the base-panel-to-foundation joint, and the effect of the panel perforations on the wall surface strains. Additional comparisons are provided between the ACI ITG-5.1 (2007) validation requirements and the observed performance of each wall. Comparisons between the design predictions and the measured behaviors of the test specimens can be found in Chapter 8.

7.1 ENERGY DISSIPATION

The primary source of energy dissipation in the walls was the yielding of the mild steel reinforcement (i.e., E.D. bars) over the unbonded length of the bars at the base joint. To quantify the amount of energy dissipation, ACI ITG-5.1 uses the relative energy dissipation ratio, β, as shown in Figure 2.2. ACI ITG-5.1 requires that β be not less than 0.125 at the validation-level drift, Δ_{wc}. The measured and analytical β ratios of the six specimens are plotted against the wall drift in Figures 7.1(a) and 7.1(b), respectively. The last cycle at each drift level was used to calculate β. It can be seen that all specimens except for Specimen HW2 satisfied the ACI ITG-5.1 minimum β requirement at moderate drift levels and continued to exceed the minimum limit until the end of the test. Due to the E.D. bar pullout, the energy dissipation of Specimen HW2 rapidly decreased after the drift cycles to Δ_w=±1.15% and did not satisfy the ACI ITG-5.1 minimum β at the end of the test.

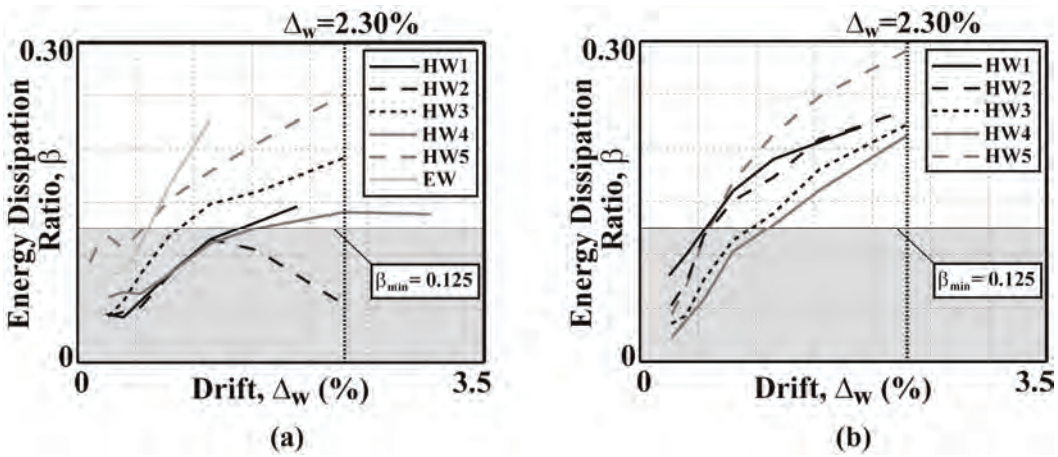

Figure 7.1 Relative Energy Dissipation Ratio: (a) Measured; (b) Fiber Element Analytical Model

As may be expected, the perforated Specimen HW4 demonstrated smaller energy dissipation than the solid hybrid walls. This can be attributed to the increased shear deformations of the wall due to the presence of the panel perforations, resulting in smaller gap opening displacements across the base joint (i.e., vertical size of gap at the location of the E.D. bars) and, in turn, less E.D. steel deformations and strains as compared to the solid walls. Note that while the other perforated Specimen HW5 (with larger perforations) demonstrated larger energy dissipation than the solid hybrid walls, this was related to the increased E.D. steel area crossing the base joint.

Also as expected, Specimen EW demonstrated considerably larger energy dissipation than the hybrid specimens. In Specimens HW1, HW2, HW3, and HW4, approximately 40% of the base moment strength was provided by the unbonded PT steel, which remained mostly linear-elastic during the test and did not contribute to the energy dissipation. In Specimen HW5, the PT steel contribution to the base moment strength was reduced to approximately 27%. The emulative wall (designed for a similar base moment strength) replaced all of the PT steel with additional E.D. bars, resulting in larger energy dissipation but smaller self-centering.

In general, the fiber element analytical results provided a reasonable match for the measured energy dissipation of the solid hybrid walls. An exception occurred in Specimen HW2 due to the premature failure of the wall and the inability of the model to capture the pullout of the E.D. bars. A large discrepancy also occurred in the perforated walls (Specimens HW4 and HW5), primarily due to the inability of the model to predict the nonlinear shear behavior of the walls. Note that the analytical model of Specimen EW was subjected to a pushover analysis; and thus, the energy dissipation could not be calculated.

7.2 E.D. BAR STRAINS

Since the E.D. bars crossing the base joint serve as the main energy dissipater for a hybrid wall, it is essential for these bars to yield well before the design-level drift, Δ_{wd}, but not fracture before the maximum-level drift, Δ_{wm}. Each E.D. bar in the test specimens utilized a plastic-wrapped unbonded length [as shown in Figures 4.5(a) and 4.5(b)] to reduce the steel strains, and thus, prevent low-cycle fatigue fracture as the wall was displaced. Additionally, the bars were typically located near the wall centerline to further reduce the strains and, in turn, reduce the required unbonded length. An exception occurred in Specimen HW5, where the bars were more evenly distributed along the length of the wall, and in Specimen EW, where the bars were placed at the ends of the panel. The location, wrapped length, and material properties for the E.D. bars in each specimen are summarized in Tables 4.1 and 4.2 and shown in Figures 4.2 through 4.7.

Figure 7.2 shows the measured (using strain gauges placed within the wrapped unbonded length) and predicted (using the fiber element and finite element analytical models) steel strains for the north intermediate E.D. bar in the test specimens. The differences in the steel strains for the positive and negative drift directions are due to the different elongations of the bar as the wall

was displaced laterally in each direction. For clarity, the measured and fiber model strains are shown at the peak of the 3rd cycle of each drift increment instead of the full cyclic strain history. Due to gauge failure, measurements could only be taken up to a drift level of Δ_w=±1.15% or Δ_w=±1.55%, depending on the specimen. The shaded regions in Figure 7.2 show the yield strain of the E.D. bars demonstrating that as designed, the bars yielded relatively early in the loading history.

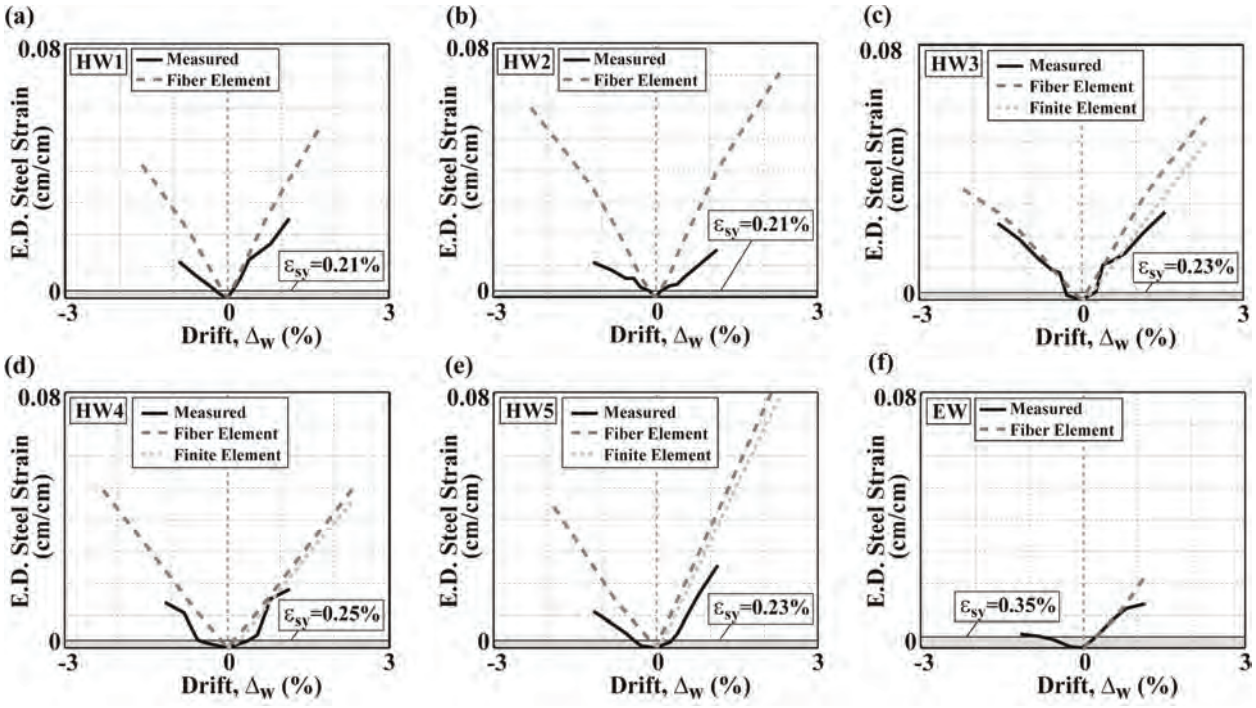

Figure 7.2 Selected E.D Steel Bar Strains: (a) Specimen HW1; (b) Specimen HW2; (c) Specimen HW3; (d) Specimen HW4; (e) Specimen HW5; (f) Specimen EW

The E.D. bar strains predicted by the fiber element analytical model significantly overestimated the measured strains for Specimen HW2 [see Figure 7.2(b)] since the pullout of the bars was not included in the model. The E.D. bar strains for Specimen HW5 [see Figure 7.2(e)] were also considerably overestimated, which could be due to the inability of the fiber and finite element models to capture the nonlinear shear displacements of the wall. Note that while an undesirable out-of-plane mechanism formed in the E.D. bars of Specimen HW5 (see Section

6.6), this occurred after gauge failure and, as a result, did not affect the measured results in Figure 7.2(e). The measured and predicted strains for the other test specimens generally compared better.

In Specimen EW, since the E.D. bar reinforcement was placed at the ends of the panel rather than near the centerline, larger bar elongations were expected. Therefore, longer unbonded lengths were used to limit the maximum bar strains. Again, these bars were designed to yield relatively early. However, because horizontal shear slip at the base joint contributed significantly to the total wall drift (as described in Section 7.8), the gap opening displacements at the base of the wall were smaller than in the hybrid specimens, and thus, the E.D. bar strains also remained relatively small. The fiber element analytical model, which included the effect of the horizontal shear slip displacements at the base (see Figure 6.6), provided a good match to the measured strains.

7.3 PT STEEL STRESSES

The PT steel provides the main restoring force for the hybrid wall system, allowing the structure to return to its initial undisplaced position upon removal of the lateral loads. Figure 7.3 depicts the measured restoring force for each hybrid specimen by plotting the normalized average stress in each of the north and south tendons [calculated as the sum of the measured individual strand forces divided by $A_p f_{pu}$, where A_p is the total area of the strands in each tendon and f_{pu}=1862 MPa (270 ksi)]. Figure 7.4 displays the analytical results from the fiber and finite element models. Similar to the E.D. steel reinforcement, the differences in the north and south tendon stresses are due to the different elongations of the north and south tendons as the wall was displaced laterally.

Consistent with the design expectations, the PT strands remained essentially linear-elastic until about Δ_w=±1.55%, which was possible since the strands were unbonded over their length. Losses in the PT steel stresses, which occurred primarily due to a small amount of nonlinear behavior in the strand-anchorage system, can be seen in the large displacement cycles, initiating during the Δ_w=±1.90% cycles in Specimen HW1 and clearly visible during the Δ_w=±2.30% cycles in Specimens HW2, HW3, HW4, and HW5 (note the initial and final stresses shown in Figure 7.3). Despite these losses, the residual drift of each hybrid wall (with the exception of Specimen HW5) at the end of the test was negligible (see Chapter 6). The analytical models matched the measured PT steel behavior reasonably well; however, the PT stress losses were not fully captured by the fiber element model. Similarly, discrepancies occurred in the finite element model during the large drift levels, due to the inability of the monotonic pushover analysis to fully capture the nonlinear behavior of the PT strands.

To prevent premature yielding of the PT steel and maintain a sufficient restoring force for the structure, ACI ITG-5.1 requires that at one half the validation-level drift (i.e., at Δ_w= $0.5\Delta_{wc}$), the stress in the tendons be less than 90% of the monotonic material stress at a strain of 0.01-cm/cm (0.01-in./in.). Based on material testing, the limiting 90% stress at 0.01-cm/cm (0.01-in./in.) for the strands used in the test specimens was $0.9f_{p@0.01}$=1514-MPa (219.6-ksi). For the hybrid specimens, the maximum measured PT stresses at $0.5\Delta_{mc}$=±1.15% ranged between 1329-MPa (192.8-ksi) and 1433-MPa (207.9-ksi), thus satisfying the ACI ITG-5.1 requirement.

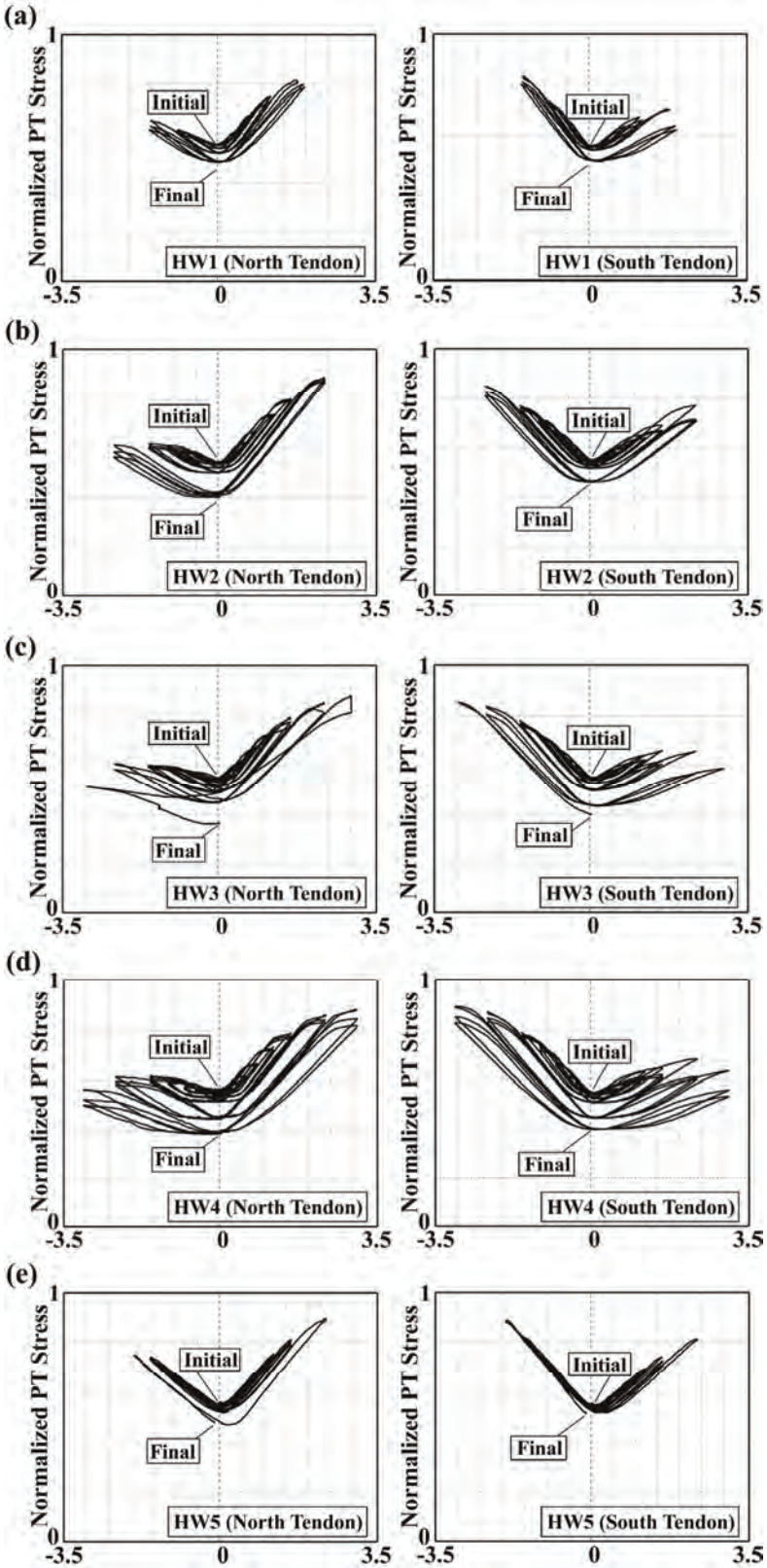

Figure 7.3 Measured PT Steel Tendon Stresses: (a) Specimen HW1; (b) Specimen HW2; (c) Specimen HW3; (d) Specimen HW4; (e) Specimen HW5

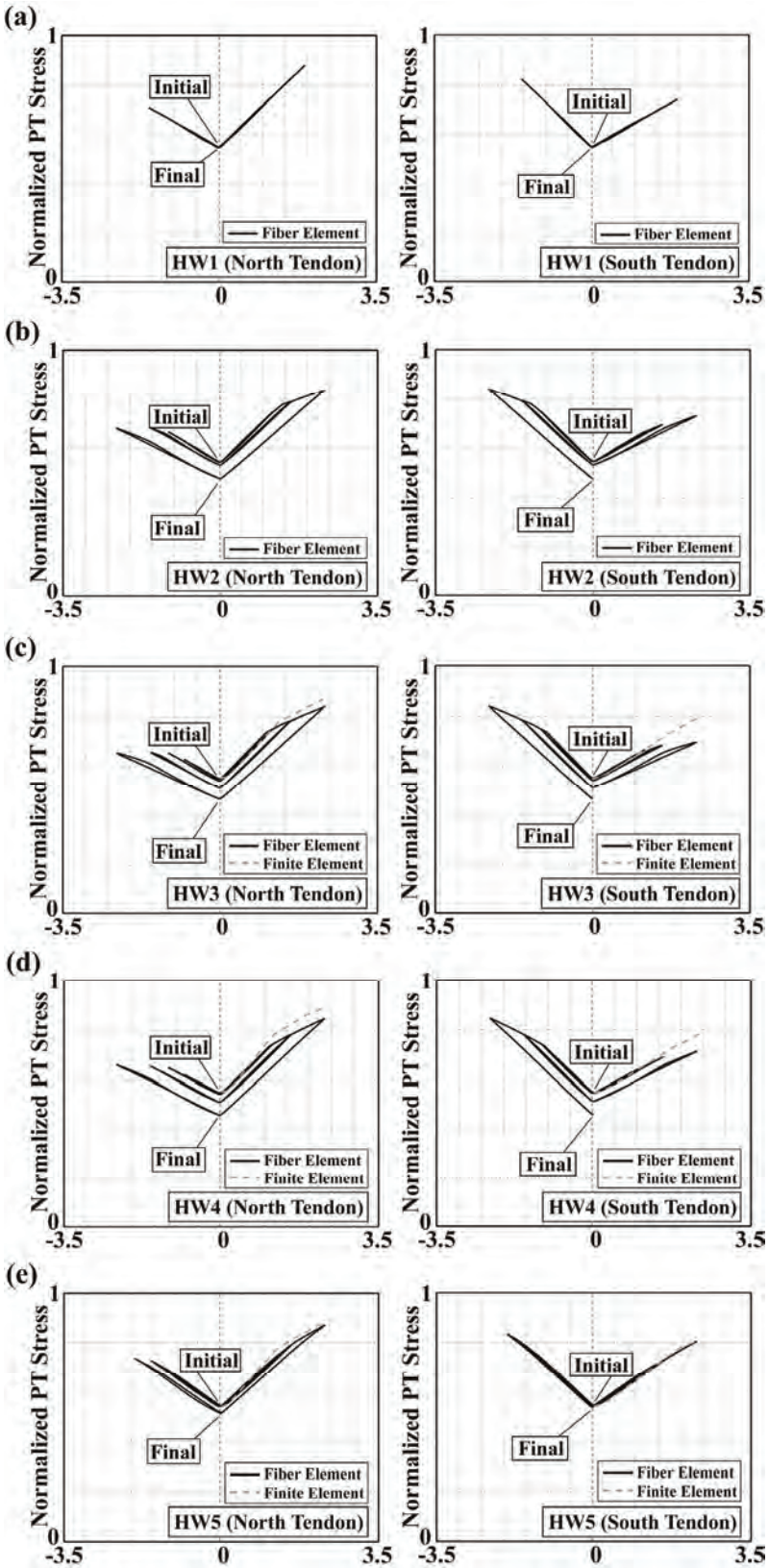

Figure 7.4 Fiber Element and Finite Element Analytical PT Steel Tendon Stresses: (a) Specimen HW1; (b) Specimen HW2; (c) Specimen HW3; (d) Specimen HW4; (e) Specimen HW5

7.4 GAP OPENING DISPLACEMENTS

Consistent with the expected behavior of the precast wall system, each test specimen opened a significant gap at the base-panel-to-foundation joint. As designed, the gap opening at the upper panel-to-panel joint was negligible. Figure 7.5 shows the measured vertical (upward positive) maximum gap opening displacements across the base joint (i.e., vertical size of gap) at the extreme north and south ends of the walls as determined by using five LVDTs plus a rotation transducer placed at the wall base. Figure 7.6 displays the analytical gap opening displacements from the fiber and finite element models.

In general, all of the hybrid specimens demonstrated similar gap opening behavior and displacements. Increased panel shear distortions (discussed in Section 7.6) and the distributed placement and increased area of the E.D. bars in the perforated Specimen HW5 resulted in slightly smaller gap opening along the base joint than in the solid hybrid walls. While the gap opening in the other perforated Specimen HW4 was similar to the solid hybrid specimens at the panel ends, the gap opening was smaller at the centerline of Specimen HW4 near the location of the E.D. steel bars (note that this result is not shown in Figure 7.5), which may indicate that the bottom of the base panel over the gap length did not remain straight (unlike the design assumption in Figure 3.4). It can also be seen that the emulative Specimen EW formed a smaller gap than the hybrid specimens. This is due to the excessive horizontal shear slip displacements that occurred at the base joint of the emulative wall, resulting in a much smaller contribution from gap opening to the total wall lateral displacements. As shown in Figure 7.6, the analytical results generally provided an excellent match with the measured gap opening displacements. An exception occurred in Specimen HW5, where the models overpredicted the gap opening displacements, likely because of the inability of the models to capture the nonlinear shear deformations of the wall panels.

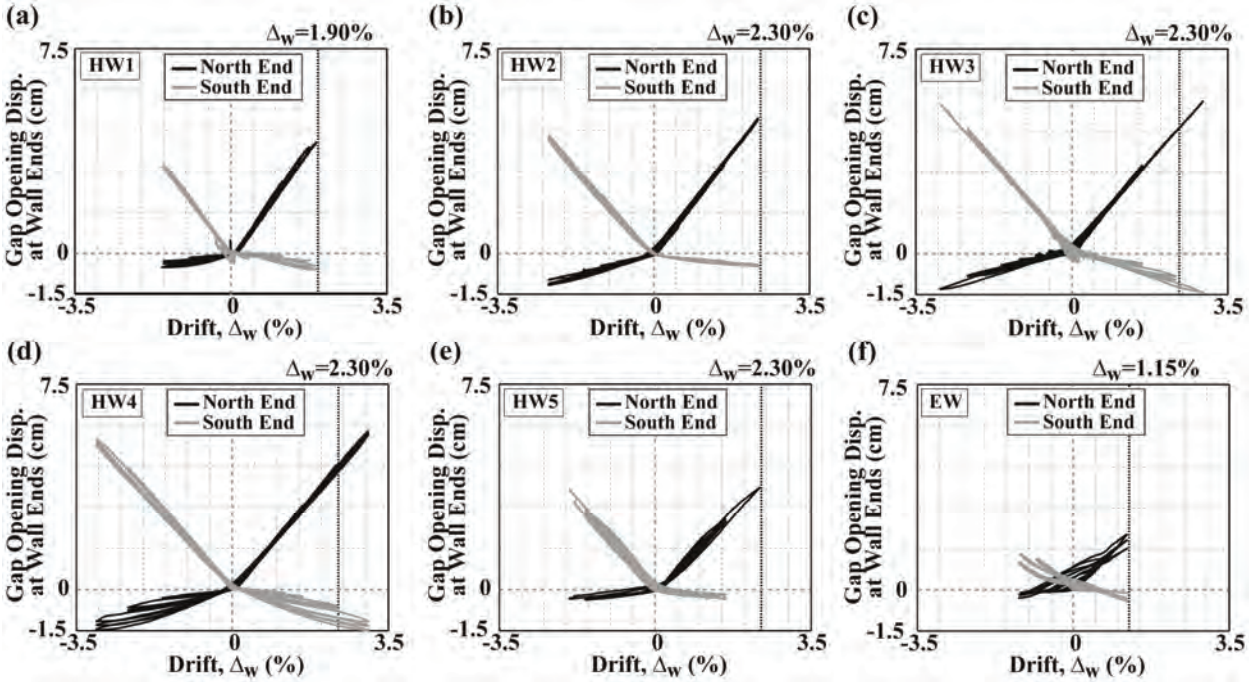

Figure 7.5 Measured Gap Opening Displacement at Wall Ends: (a) Specimen HW1; (b) Specimen HW2; (c) Specimen HW3; (d) Specimen HW4; (e) Specimen HW5; (f) Specimen EW

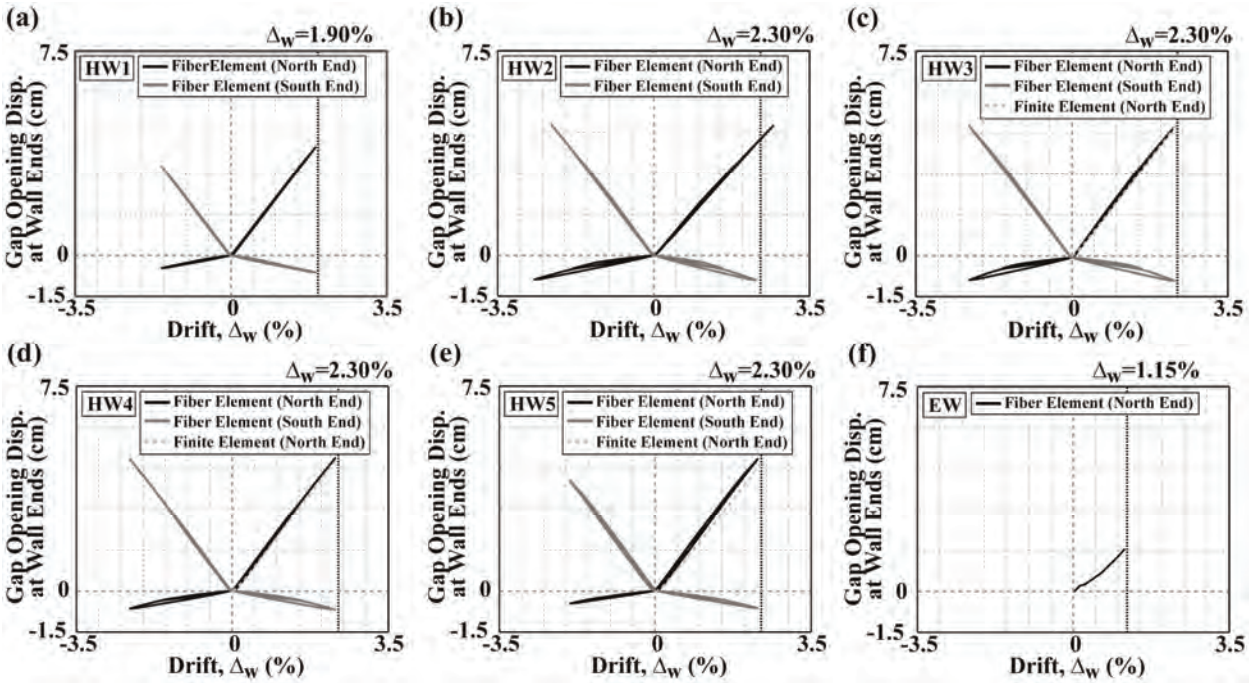

Figure 7.6 Fiber Element and Finite Element Analytical Gap Opening Displacements at Wall Ends: (a) Specimen HW1; (b) Specimen HW2; (c) Specimen HW3; (d) Specimen HW4; (e) Specimen HW5; (f) Specimen EW

7.5 NEUTRAL AXIS LENGTH

Using the 3D-DIC data, Figure 7.7(a) plots the measured neutral axis length (i.e., "contact length") across the base-panel-to-foundation joint at the south end of the wall (since 3D-DIC was only used to monitor the south end). The results are shown for the peak of the 1st cycle in each drift series, except for the last series where all three cycles are shown. In general, the neutral axis plots for all six specimens display many similarities. During the small displacements of each wall, the neutral axis length went through a rapid decrease associated with gap opening at the base. Due to the compression forces from the PT steel, the neutral axis length was larger in the hybrid specimens as compared to the emulative specimen during the early cycles. As each wall was displaced further, the neutral axis length continued to decrease but at a much slower pace. Once deterioration of the concrete at the wall toes initiated, the neutral axis length began to elongate to satisfy equilibrium with the reduced concrete stresses. This effect is particularly evident during the final drift series for Specimens HW1, HW3, and EW. In Specimens HW4 and HW5, the neutral axis remained stable over a much larger drift range, as the elongation of the neutral axis length was not observed in Specimen HW5 and was evident in Specimen HW4 only after achieving the validation-level drift, Δ_{wc}=+2.30%. This was primarily due to the confinement steel detailing improvements incorporated into these specimens as discussed in Chapter 6. Note that the elongation of the neutral axis length did not occur in Specimen HW2 since damage to the concrete was small due to the pullout of the E.D. bars (i.e., smaller tension forces in the E.D. steel led to smaller concrete compressive forces at the wall toes).

The analytical predictions of the neutral axis length are displayed in Figures 7.7(b) and 7.7(c) for the fiber element and finite element models, respectively. The models generally predicted a smaller neutral axis length throughout the displacement history, particularly during the smaller displacement cycles. This could be related to the inability of the models to accurately

determine the concrete compression stresses at the wall toes as gap opening occurred. In addition, the models for Specimens HW1 and HW3 underpredicted the elongation of the neutral axis length during the larger displacement cycles. This is related to the confined concrete damage that occurred in these walls (discussed in Chapter 6), which was not captured by the analyses, especially using the finite element model. The models more accurately predicted the neutral axis length for Specimens HW4 and HW5, which featured improved confinement details resulting in more stable concrete behavior. The discrepancy in Specimen HW2 was due to the premature pullout of the E.D. bars, which was not included in the models.

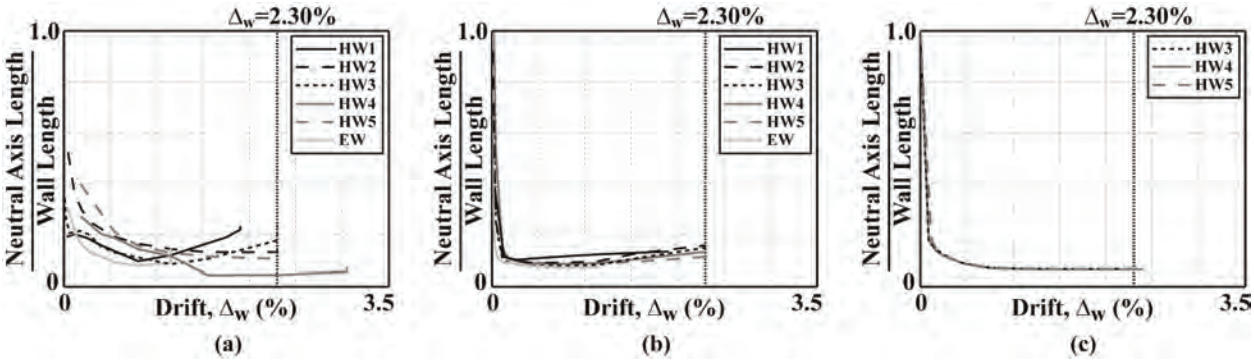

Figure 7.7 Neutral Axis Length along Base-Panel-to-Foundation Joint: (a) Measured; (b) Fiber Element Analytical Model; (c) Finite Element Analytical Model

7.6 PANEL SHEAR DEFORMATIONS

Figure 7.8(a) shows the shear distortion angle, γ of the base panel (at the peak of the 3rd cycle in each drift series) measured using two diagonally placed string potentiometers (calculated as described in Oesterle et al. 1976). In general, the shear distortions were small, which becomes more obvious when, in Figure 7.8(b), the distortion angle of the base panel is plotted as a percentage of the total drift angle to the top of the base panel, Δ_{bp} (defined as the relative lateral displacement between the top of the base panel and the top of the foundation divided by the height to the top of the base panel). Note that Δ_{bp} was nearly equal to Δ_w since the lateral

displacements of the walls were largely governed by rigid body rotations through the gap opening at the base. The measured results in Figure 7.8 demonstrate that the solid walls (both hybrid and emulative specimens) underwent generally small shear deformations despite the relatively low M_{wd}/V_{wd} ratio of $1.5L_w$, as the maximum contribution of the shear distortion to the total base panel drift at the end of the test was typically less than 5%. As would be expected, the shear distortions of the emulative wall were larger than those in the solid hybrid walls. The perforated hybrid Specimens HW4 and HW5 experienced larger shear distortions than the solid specimens, particularly during the early drift series and especially for Specimen HW5 with the larger perforations. The contribution of the shear deformations to the total base panel drift in Specimen HW5 was approximately 19% at Δ_w=+2.30%.

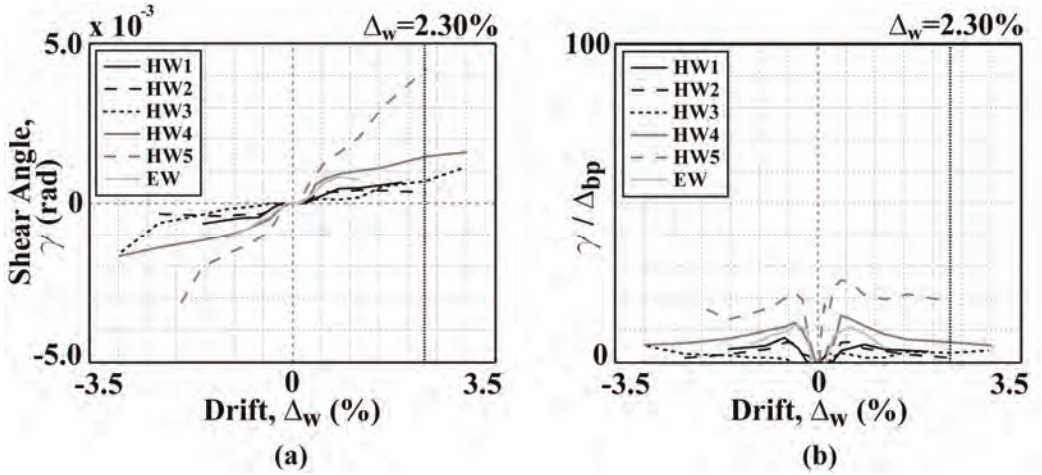

Figure 7.8 Measured Shear Deformations: (a) Shear Distortion of Base Panel; (b) Shear Distortion Normalized by Total Base Panel Drift

7.7 RESIDUAL WALL UPLIFT

The vertical displacement at the top of the wall, which is related to the gap opening along the horizontal joints, can be used to determine the residual uplift of the test specimens (i.e., residual axial elongation or heightening of the wall upon unloading from a lateral displacement). Figure 7.9 shows the residual axial elongation (upwards positive) measured at the centerline of

each wall at the same elevation as the applied lateral load upon unloading to Δ_w=0% from the 3rd cycle in each drift series. The accumulation of this residual axial elongation represents a reduction or loss of the axial restoring force in the system. In Specimens HW1, HW2, HW3, and HW4, the axial elongation did not start to accumulate until the Δ_w=±1.55% drift cycles, which coincided with the initiation of the PT stress losses. Among these four walls, the largest residual elongations occurred in Specimen HW3, where the maximum elongation upon unloading from the validation-level drift of 2.30% was 0.17-cm (0.07-in.). This small amount of uplift did not affect the performance of the wall in any undesirable way.

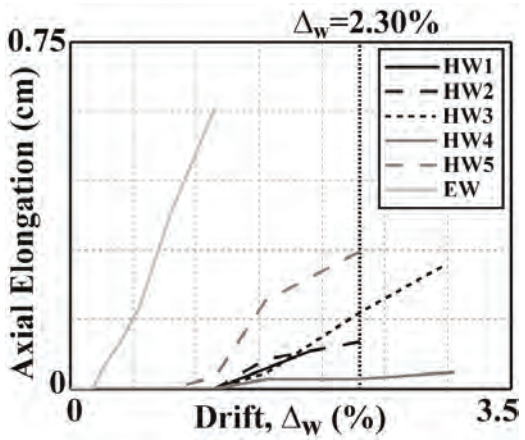

Figure 7.9 Measured Residual Wall Uplift

In Specimen HW5, the residual axial elongation started to accumulate earlier (during the Δ_w=±1.15% drift cycles) and the maximum residual elongation at the validation-level drift was almost twice as large [0.30-cm (0.12-in.)]. This increased uplift is related to the reduced self-centering in the wall (from the PT force plus the gravity load) and the increased contribution of the E.D. steel to the total base moment strength. Once the E.D. bars yielded in tension, the restoring force was not sufficient to yield the bars back in compression and return to essentially zero elongation upon unloading. Over successive loading/unloading cycles with increasing wall drift, the residual tensile deformations in the bars resulted in the complete uplift of the structure,

overcoming the downward restoring force. This undesirable behavior ultimately caused out-of-plane displacements of the wall base during unloading and buckling of the E.D. bars in compression, leading to the failure of the wall.

The emulative wall (Specimen EW) accumulated significantly greater axial elongations as compared to the hybrid walls, beginning from the Δ_w=±0.27% cycles, with a maximum uplift of 0.61-cm (0.24-in.) after the last cycle to Δ_w=±1.15%. The large uplift of the emulative system is related to the lack of PT steel, which resulted in an even smaller restoring force (provided only by the gravity load) than in Specimen HW5. The axial elongations of Specimen EW accumulated very rapidly (see Figure 7.9), ultimately leading to the failure of the wall due to excessive horizontal in-plane slip at the base joint, with large strength and stiffness degradation.

7.8 HORIZONTAL SHEAR SLIP

The horizontal shear slip at the upper panel-to-panel joint of the test specimens was negligible. By examining the 3D-DIC data for the relative horizontal displacements between adjacent points on either side of the base-panel-to-foundation joint, the horizontal slip at the base of each wall was determined. Figure 7.10 shows the measured base slip at the centerline of the walls. For each specimen, only the peak of the 3rd cycle in each drift series is plotted, except for the final drift series where all cycles are plotted.

The slip at the base joint of the hybrid specimens was generally small. For Specimen HW4, the measured slip did not exceed the maximum allowable slip of 0.15-cm (0.06-in.) per ACI ITG-5.1 (shown by the shaded region in Figure 7.10). Specimen HW3 satisfied the ACI slip limit in the positive loading direction but the maximum slip in the negative direction [0.35-cm (0.12 in.)] exceeded this limit towards the end of the test. Specimens HW1 and HW2 also exceeded the ACI slip limit towards the end of each test [maximum measured slip was 0.20-cm

(0.08 in.) and 0.38-cm (0.15 in.) for Specimens HW1 and HW2, respectively]. The measured amount of slip in these specimens did not affect the performance of the walls in any undesirable way, indicating that the slip limit of 0.15-cm (0.06-in.) in ACI ITG-5.1 may be too conservative. Based on the performance of the test specimens, a more reasonable slip limit may be 0.38-cm (0.15 in.).

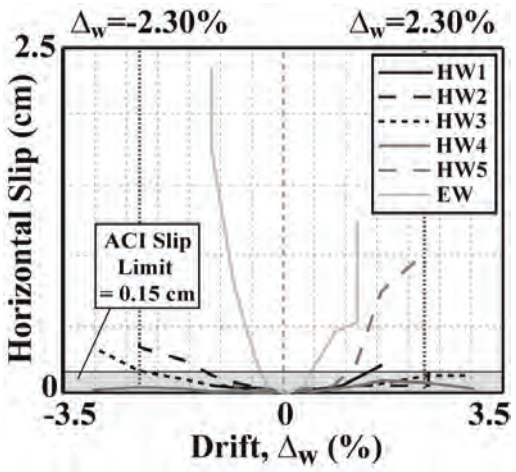

Figure 7.10 Measured Horizontal Slip at Wall Centerline along Base-Panel-to-Foundation Joint

The shear slip at the base joint of Specimen HW5 was significantly larger than in the other hybrid specimens [1.03-cm (0.41-in.)] and accumulated disproportionally in the positive drift direction. The slip displacements began to rapidly increase at Δ_w=±1.15% when, as shown in Figure 7.9, the accumulation of the residual wall uplift also initiated. Upon reloading from complete uplift at the base, the E.D. bars were the only components transferring shear forces from the wall into the foundation until the lateral displacement was large enough to close the gap at the compression toe of the wall. This undesirable in-plane behavior ultimately caused out-of-plane displacements of the wall base and buckling of the E.D. bars in compression, leading to the failure of the wall. The excessive in-plane horizontal slip and subsequent out-of-plane failure of Specimen HW5 was related to the reduced self-centering in the wall (from the PT force plus the

gravity load) due to the reduced PT steel area and increased E.D. steel area. Note that as in the case for the other hybrid specimens, the slip at the upper panel-to-panel joint of Specimen HW5 was negligible.

For Specimen EW, the horizontal slip at the base joint was much larger than the other specimens [2.36-cm (0.93-in.)]. Similar to Specimen HW5, the slip displacements increased rapidly once the accumulation of the residual wall uplift initiated, which began at Δ_w=±0.27% for Specimen EW (see Figure 7.9). Again, upon reloading from complete uplift at the base, the E.D. bars were the only components transferring shear forces from the wall into the foundation until the lateral displacement was large enough to close the gap at the compression toe of the wall. Unlike Specimen HW5, no significant out-of-plane displacements occurred in Specimen EW. Instead, the concrete around the E.D. bars began to deteriorate due to the shear force transfer, ultimately causing failure through localized splitting of the base panel around the bars. As in the case for the hybrid specimens, the slip at the upper panel-to-panel joint of the emulative wall was negligible.

At the point when slip at the base joint started to rapidly accumulate in Specimen EW (i.e., at first loading to Δ_w=+0.27%), an estimate of the coefficient of shear friction can be made by dividing the measured base shear force [374-kN (84.1-kips)] with the compression force transferred through the contact region. This compression force was estimated as the measured gravity load [365-kN (82.1-kips)] plus the total force in the tensile E.D. bars [552-kN (124.1-kips)] using the steel stresses determined from the measured strains and the measured monotonic stress-strain relationship. The resulting coefficient of shear friction was calculated as 0.41, which is considerably smaller than the value of 0.50 recommended by ACI ITG-5.2 for the base-panel-to-foundation joint.

7.9 EFFECT OF PANEL PERFORATIONS

Using the 3D-DIC data, the distribution of surface strains on the wall panels was determined. Figures 7.11 and 7.12 show the *y*-direction (i.e., vertical) and *x*-direction (i.e., horizontal) surface strains, respectively, in Specimens HW3, HW4, and HW5 at the 3rd cycle of Δ_w=+1.15%. A consistent color scale is used to distinguish between the different magnitudes of strains, where -3000 micro-strain (compression) is shown as dark blue, 0 micro-strain is shown as yellow-orange, and 500 micro-strain (tension) is shown as dark red.

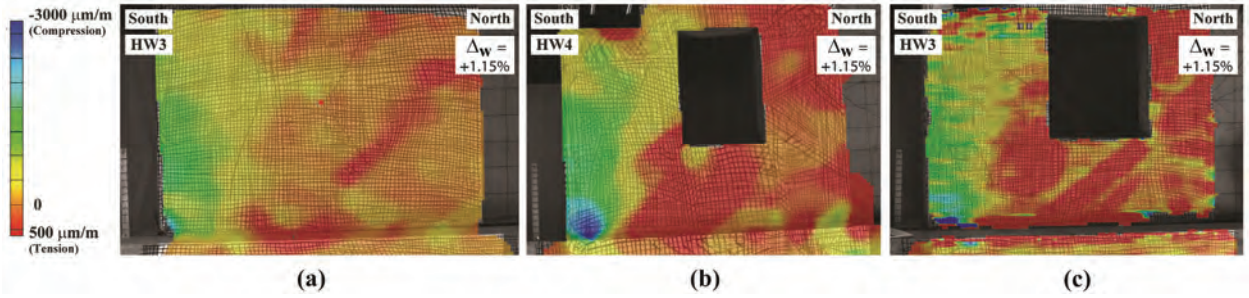

Figure 7.11 Base Panel Surface Strains in Vertical Direction at 3rd Cycle of Δ_w=+1.15%: (a) Specimen HW3; (b) Specimen HW4; (c) Specimen HW5

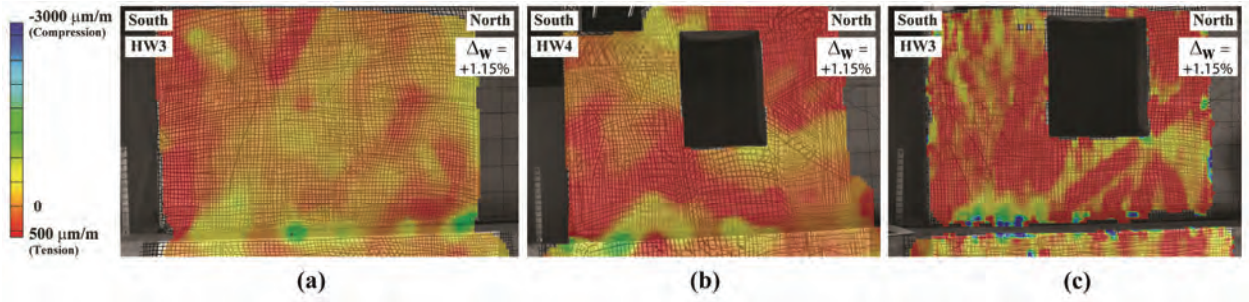

Figure 7.12 Base Panel Surface Strains in Horizontal Direction at 3rd Cycle of Δ_w=+1.15%: (a) Specimen HW3; (b) Specimen HW4; (c) Specimen HW5

By using these images, the impact of the panel perforations can be seen on the surface strain distributions of the walls. In Figures 7.11(a) and 7.12(a) for the solid Specimen HW3, the extent of the tensile regions (i.e., red colored regions) is small. In comparison, in the perforated Specimens HW4 [Figures 7.11(b) and 7.12(b)] and HW5 [Figures 7.11(c) and 7.12(c)], the tensile regions extend over a much larger area. Large tensile strains can be seen around the

corners of the perforations, which correspond to the significantly increased amount of cracking observed in the perforated walls as compared to the solid specimens. This information supports the design of the additional bonded mild steel reinforcement placed in both the horizontal and vertical directions around the perforations.

7.10 COMPARISONS WITH ACI ITG-5.1 VALIDATION REQUIREMENTS

Table 7.1 compares the measured performance of the test specimens according to the ACI ITG-5.1 (2007) validation criteria up to the last drift cycle of the largest sustained drift series during the testing of each specimen (i.e., the drift series where three fully-reversed cycles were applied to the wall with no more than 20% loss in peak lateral resistance as compared to the overall peak strength). The perforated Specimen HW4 satisfied all validation requirements at a drift of ±3.05%, which is greater than the required validation-level drift of Δ_{wc}=±2.30%, demonstrating the use of hybrid shear walls as "special" reinforced concrete shear walls in seismic regions. The solid Specimen HW3 satisfied all of the ACI ITG-5.1 requirements at the validation-level drift of ±2.30%, with the exception of the maximum shear slip limit in the negative direction of loading. However, as stated previously, the measured base slip of this specimen did not affect the performance of the wall in any undesirable way, indicating that the current slip limit in ACI ITG-5.1 may be too conservative.

Specimens HW1, HW2, HW5, and EW did not satisfy the main validation criterion of sustaining three loading cycles at or above the validation-level drift, Δ_{wc}=±2.30% prior to failure. Important design and detailing considerations were learned from the performance of these walls as described in this report. The largest sustained drift level was ±1.55% for Specimens HW1, HW2, and HW5, and ±0.80% for Specimen EW, which demonstrated the worst performance out of the six walls. Due to the pullout of the E.D. bars, the relative energy

dissipation of Specimen HW2 at ±1.55% drift was slightly less than the ACI ITG-5.1 limit of β_{min}=0.125. The performance of Specimen HW5 was negatively affected by the slip displacements as the base joint, which were larger than acceptable during the ±1.55% drift cycles. The base slip displacements in Specimen EW were also not acceptable.

Table 7.1 Comparisons with ACI ITG-5.1 Validation Requirements

ACI ITG-5.1 Validation Criterion	Performance Requirement		Specimen HW1	Specimen HW2	Specimen HW3	Specimen HW4	Specimen HW5	Specimen EW
Largest Sustained Wall Drift Series	Δ_{wc}=±2.30%	$+\Delta_w$	+1.90%	+1.55%	+2.30%	+3.05%	+1.55%	+0.80%
		$-\Delta_w$	-1.55%	-1.55%	-2.30%	-3.05%	-1.55%	-0.80%
Design/Measured Peak Base Shear Strength	0.90-1.20 (range)	$+\Delta_w$	0.94	0.97	1.00	1.04	0.96	1.09
		$-\Delta_w$	0.92	1.08	1.05	1.02	0.98	1.19
Largest Base Shear Strength Loss	20% (maximum)	$+\Delta_w$	20.0%	13.6%	19.9%	18.9%	4.7%	8.0%
		$-\Delta_w$	15.6%	17.2%	13.8%	18.7%	1.7%	6.0%
Energy Dissipation Ratio, β	0.125 (minimum)	n/a	0.15	0.11	0.19	0.14	0.21	0.17
[1]Secant Stiffness, E_w	[2]$0.1E_{wi}$ (minimum)	$+\Delta_w$	$0.31E_{wi}$	$0.38E_{wi}$	$0.13E_{wi}$	$0.13E_{wi}$	$0.20E_{wi}$	$0.19E_{wi}$
		$-\Delta_w$	$0.41E_{wi}$	$0.39E_{wi}$	$0.10E_{wi}$	$0.13E_{wi}$	$0.40E_{wi}$	$0.28E_{wi}$
Largest PT Stress at $0.5\Delta_{wc}$	[3]$0.9f_{p@0.01}$ (maximum)	North Tendon	$0.83f_{p@0.01}$	$0.81f_{p@0.01}$	$0.81f_{p@0.01}$	$0.80f_{p@0.01}$	$0.82f_{p@0.01}$	n/a
		South Tendon	$0.85f_{p@0.01}$	$0.79f_{p@0.01}$	$0.80f_{p@0.01}$	$0.81f_{p@0.01}$	$0.82f_{p@0.01}$	n/a
Largest Shear Slip	0.15-cm (maximum)	$+\Delta_w$	0.20-cm	0.05-cm	0.12-cm	0.09-cm	0.73-cm	0.46-cm
		$-\Delta_w$	0.05-cm	0.23-cm	0.30-cm	0.04-cm	0.05-cm	0.79-cm

[1]E_w=measured secant stiffness of wall during last sustained drift cycle per ACI ITG-5.1; [2]E_{wi}=measured initial secant stiffness of wall at $0.75V_{wd}$; [3]$f_{p@0.01}$=stress in PT strand at 0.01-cm/cm [0.01-in./in.] strain based on monotonic material testing [1682.7-MPa (244-ksi)].

CHAPTER 8

VALIDATION OF DESIGN PROCEDURE

This chapter uses the measured response of the test specimens to summarize the validation of the hybrid wall design procedure described in the Design Procedure Document (Smith and Kurama 2012a). First, the design predictions are compared with the measured performance at both the design-level drift, Δ_{wd} and the maximum-level drift, Δ_{wm} used in the design of the walls. Then, key recommendations from the Design Procedure Document are summarized and evaluated based on the observed behavior of the test specimens. Finally, proposed modifications and additions to ACI ITG-5.2 (2009) and ACI ITG-5.1 (2007) are presented based on the results from the project.

8.1 COMPARISONS WITH DESIGN PREDICTIONS

Tables 8.1 and 8.2 compare key aspects of the measured behavior of the test specimens with the design predictions at the 1st cycle to the design-level drift, Δ_{wd} and the 1st cycle to the maximum-level drift, Δ_{wm}, respectively. The design-level drift, Δ_{wd} differed between the different walls because of variations in the actual compression strength, f_c' of the concrete in each specimen, which affected the concrete Young's modulus, E_c. The maximum-level drift for the test specimens was the same as the ACI ITG-5.1 validation-level drift of Δ_{wc}=±2.30%. However, since Specimens HW1 and EW did not reach this drift level, the comparisons in Table 8.2 for these two walls are made at the 1st cycle to the failure-level drift, $\Delta_{w,failure}$ (i.e., the drift series during which more than 20% loss occurred in peak lateral resistance as compared to the overall peak strength). The range of data for the E.D. bar strains and PT tendon stresses in Tables

8.1 and 8.2 are due to the different elongations of the north and south intermediate E.D. bars and north and south PT tendons when the wall was displaced laterally in one direction.

Note that while the design predictions utilized the measured monotonic stress-strain behavior for the E.D. steel [see Figure 4.10(b)], the modified stress-strain relationship in Figure 5.4(b) was used for the PT steel in order to account for the localized concrete and anchorage deformations at the tendon ends (which could not be otherwise captured by the design predictions). Furthermore, the predictions for the E.D. and PT steel elongations at the wall base excluded the estimated shear deformations and linear-elastic flexural deformations over the wall height. This was done by subtracting the shear deformations and linear-elastic flexural deformations of the wall (estimated using the linear-elastic effective stiffness model in Section 5.1) from Δ_w in Figure 3.4, thus resulting in the steel elongations due to gap opening at the base.

Table 8.1 Comparisons with Design Predictions at Design-Level Drift

Design Parameter	**Specimen HW1** Δ_{wd}**=+0.70%**		**Specimen HW2** Δ_{wd}**=+0.60%**		**Specimen HW3** Δ_{wd}**=+0.54%**		**Specimen HW4** Δ_{wd}**=+0.83%**		**Specimen HW5** Δ_{wd}**=+0.87%**		**Specimen EW** Δ_{wd}**=+0.61%**	
	Design	Measured	Design	Measured	Design	Measured	Design	Measured	Design	Measured	Design	Measured
Applied Lateral Load, V_{bd}	478-kN	507-kN	481-kN	480-kN	467-kN	493-kN	483-kN	490-kN	558-kN	562-kN	514-kN	470-kN
Intermediate E.D. Bar Strains, ε_{sd}	2.1% and 2.5%	1.1% and 1.6%	1.9% and 2.2%	0.6% and 1.0%	1.0% and 1.2%	0.9% and 1.2%	1.4% and 1.7%	1.3% and 1.6%	1.7% and 2.9%	0.9% and 1.8%	0.2% and 1.7%	0.2% and 1.0%
PT Tendon Stresses, f_{pd}	0.60 and 0.64f_{pu}	0.63 and 0.68f_{pu}	0.59 and 0.63f_{pu}	0.60 and 0.65f_{pu}	0.59 and 0.63f_{pu}	0.59 and 0.64f_{pu}	0.61 and 0.67f_{pu}	0.62 and 0.71f_{pu}	0.63 and 0.65f_{pu}	0.65 and 0.69f_{pu}	n/a	n/a
Maximum Gap Opening	13-mm	15-mm	11-mm	12-mm	10-mm	11-mm	15-mm	16-mm	15-mm	16-mm	11-mm	9-mm
Neutral Axis Length, c_d	272-mm	276-mm	239-mm	434-mm	316-mm	322-mm	355-mm	339-mm	378-mm	393-mm	267-mm	210-mm

Table 8.2 Comparisons with Design Predictions at Maximum-Level or Failure-Level Drift

Design Parameter	Specimen HW1 $\Delta_{w,failure}$=+1.75%		Specimen HW2 Δ_{wm}=+2.30%		Specimen HW3 Δ_{wm}=+2.30%		Specimen HW4 Δ_{wm}=+2.30%		Specimen HW5 Δ_{wm}=+2.30%		Specimen EW $\Delta_{w,failure}$=+1.15%	
	Design	Measured	Design	Measured	Design	Measured	Design	Measured	Design	Measured	Design	Measured
Applied Lateral Load, V_{bm}	494-kN	507-kN	533-kN	458-kN	552-kN	507-kN	550-kN	527-kN	613-kN	630-kN	624-kN	534-kN
Intermediate E.D. Bar Strains, ε_{sm}	4.7% and 5.5%	---	6.6% and 7.8%	---	4.6% and 5.5%	---	4.4% and 5.2%	---	4.9% and 8.0%	---	0.5% and 3.2%	0.4% and 1.4%
PT Tendon Stresses, f_{pm}	0.63 and $0.73f_{pu}$	0.70 and $0.82f_{pu}$	0.69 and $0.78f_{pu}$	0.77 and $0.88f_{pu}$	0.70 and $0.80f_{pu}$	0.65 and $0.85f_{pu}$	0.69 and $0.79f_{pu}$	0.68 and $0.86f_{pu}$	0.72 and $0.77f_{pu}$	0.81 and $0.90f_{pu}$	n/a	n/a
Maximum Gap Opening	35-mm	39-mm	48-mm	50-mm	49-mm	59-mm	48-mm	58-mm	46-mm	37-mm	24-mm	20-mm
Neutral Axis Length, c_m	323-mm	467-mm	269-mm	306-mm	231-mm	436-mm	248-mm	110-mm	284-mm	260-mm	160-mm	218-mm

It can be seen from Table 8.1 that the design predictions at the design-level drift, Δ_{wd}, generally compared reasonably well with the measured behaviors of the walls, especially for Specimens HW3 and HW4. The premature failure of Specimen EW led to inaccuracies in the predictions, particularly for the neutral axis length. Other considerable differences can be seen for the E.D. bar strains, where the measured strains for some of the hybrid walls (Specimens HW1, HW2, and HW5) were significantly smaller than the corresponding design predictions. The predictions provided good estimates for the gap opening displacements and neutral axis lengths, with the exception of the neutral axis length for Specimen HW2.

The design predictions at the maximum-level drift, Δ_{wm} (Table 8.2) were generally greater than those at Δ_{wd}. With the exception of Specimens HW2 and EW, which suffered from premature failures, the applied lateral load, V_{bm}, was predicted reasonably well. Discrepancies between the predicted and measured PT tendon stresses were increased at Δ_{wm}, more so for the tension-side tendon. Note that no E.D. bar strain measurements were possible at this drift level due to gauge failure. The discrepancies for the maximum gap opening and the neutral axis length were also considerably increased for some of the hybrid walls, which are likely related to the

inability of the design predictions to accurately model the concrete compression stresses at the wall toes.

8.2 KEY DESIGN RECOMMENDATIONS

This section summarizes key recommendations from the Design Procedure Document (Smith and Kurama 2012a). When appropriate, experimental evidence is provided to support these recommendations.

8.2.1 Reinforcement Crossing Base Joint

The κ_d ratio used in design should not exceed 0.80 to ensure sufficient self-centering and should not be less than 0.50 to ensure sufficient energy dissipation. Specimens with κ_d ratios close to both of these limits were tested (see Table 4.1), with the actual κ_d ratios ranging from 0.50 to 0.90. Figure 7.1 shows the relative energy dissipation ratio, β of the six specimens as a function of wall drift. Specimen HW4, with design κ_d=0.50 and actual κ_d=0.54, satisfied the minimum β_{min}=0.125 requirement prescribed by ACI ITG-5.1 with a small margin, leading to the recommended lower limit of κ_d=0.50 for design. It should be noted that Specimen HW4 was a perforated wall, which increased the shear deformations in the wall panels resulting in reduced energy dissipation (as discussed in Section 6.5). While it may be possible to use a reduced value for the lower κ_d limit of solid hybrid walls, this was not investigated by this research.

The recommended upper limit of κ_d=0.80 was selected based on the premature failure of Specimen HW5 (with design κ_d=0.85 and actual κ_d=0.90) prior to sustaining three loading cycles at the validation-drift of 2.30%. As discussed in Section 6.6, this specimen suffered from a loss of restoring and failed due to the uplift of the wall from the foundation, which resulted in the subsequent out-of-plane displacements of the wall base and buckling of the E.D. bars in

compression. Wall uplift and excessive out-of-plane displacements (or in-plane slip as was observed in Specimen EW) across the base joint can develop quickly and lead to failure with little warning. Figure 6.3(e) shows the measured base shear force, V_b versus wall drift, Δ_w behavior of Specimen HW5 where the loss of restoring force can be seen by the unloading curves that do not return through the origin. Figure 8.1 shows the observed out-of-plane displacements and buckling of the E.D. bars at the base joint of the wall. The goal of the recommended upper limit on κ_d is to prevent this type of behavior.

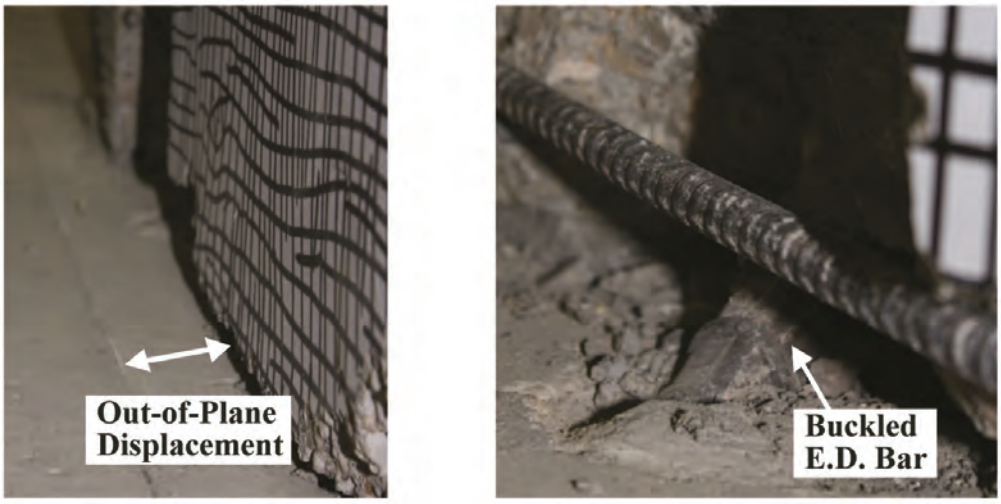

Figure 8.1 Ultimate Failure of Specimen HW5

8.2.2 Vertical Extent of Confinement Reinforcement at Wall Toes

Based on the extent of the cover concrete spalling in the test specimens, the confined concrete region at the wall toes should extend vertically over a height of the base panel not less than the plastic hinge height, defined as h_p=0.06H_w per ACI ITG-5.2. Figure 8.2 shows the north toe at the base of Specimens HW3 and HW4 [where h_p=33-cm (13-in.)] at the conclusion of each test. The observed extent of vertical cover spalling in Specimens HW3 and HW4 was approximately 35.5-cm (14-in.) and 30.5-cm (12-in.), respectively, supporting the design recommendation.

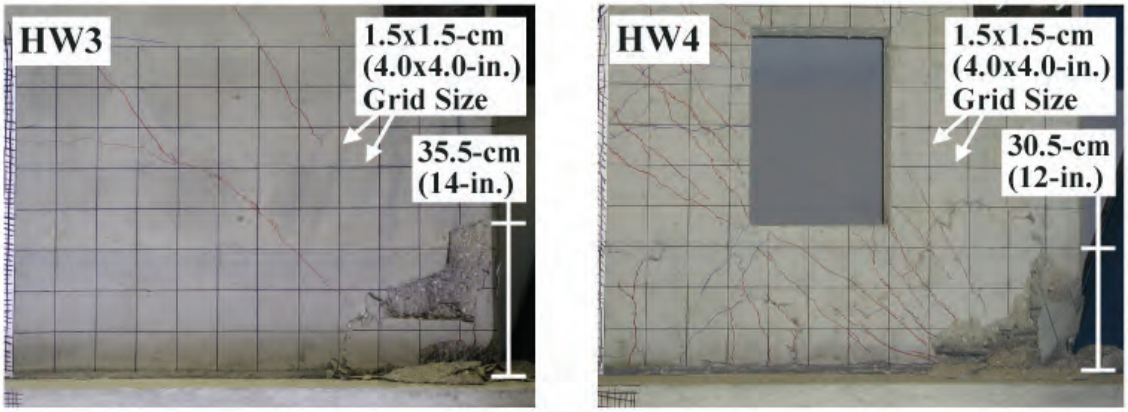

Figure 8.2 North Toe at Base of Specimens HW3 and HW4

8.2.3 Location of First Confinement Hoop at Wall Toes

The design and detailing of the confinement reinforcement should satisfy the applicable requirements for special boundary regions as well as the bar spacing and concrete cover requirements in ACI 318 (2011). The first confinement hoop should be placed at a distance from the bottom of the base panel no greater than the minimum required concrete cover. This recommendation was not satisfied in Specimen HW1 (see Table 4.1), resulting in premature confined concrete crushing as shown in Figure 8.3.

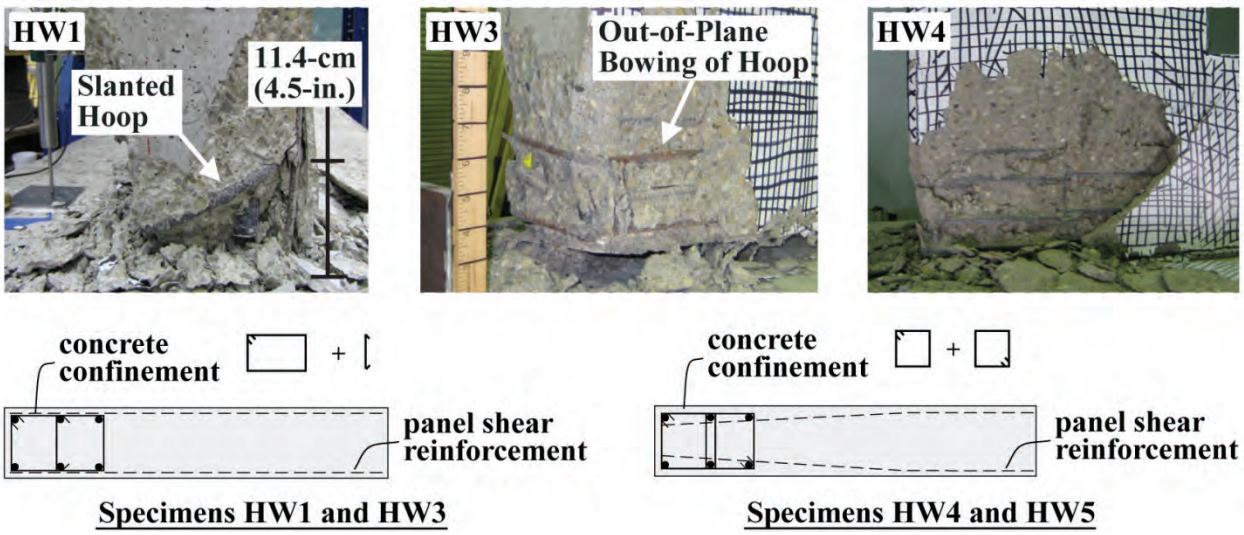

Figure 8.3 Performance and Detailing of Confined Concrete Region in Specimens HW1, HW3, HW4, and HW5.

8.2.4 Aspect Ratio of Rectangular Confinement Hoops at Wall Toes

The length-to-width aspect ratio (measured center-to-center of bar) for rectangular hoops should not exceed 2.50. This requirement is slightly more conservative than but similar to past seismic code specifications for boundary region confinement, which have since been removed from the current code requirements in the U.S. [e.g., Section 1921.6.6.6 of the Uniform Building Code (ICBO 1997)]. As observed from the performance of Specimen HW3 (see Figure 8.3), a large length-to-width ratio for the hoops can cause the bowing of the longer hoop legs in the out-of-plane direction, reducing the confinement effectiveness. Further, intermediate crossties were ineffective in preventing the bowing of the longer hoop legs, since in typical construction the crossties do not directly engage the hoop steel (rather, the crossties engage the vertical reinforcement within the hoops). For comparison, Specimens HW4 and HW5 followed all of the recommendations in Sections 8.2.3 and 8.2.4, resulting in excellent behavior of the confined concrete at the wall toes (discussed in Chapters 6 and 7). The performance of Specimen HW4 and the confinement detailing differences between the specimens are depicted in Figure 8.3.

8.2.5 Unbonded Length of E.D. Steel

The plastic-wrapped unbonded length of the E.D. bars should be designed such that the maximum strains of the bars at the maximum-level drift, Δ_{wm} are greater than $0.5\varepsilon_{su}$ to ensure sufficient energy dissipation but do not exceed $0.85\varepsilon_{su}$ to prevent low-cycle fatigue fracture, where ε_{su} is the monotonic strain capacity of the steel at peak strength. Strain limits of up to $0.85\varepsilon_{su}$ were used in the design of the test specimens (see Table 4.1), with no bar fracture observed during the experiments. The coefficient used to estimate the additional debonded length at Δ_{wm} (discussed in Section 3.1.2) can be assumed as α_s=2.0. Cores were taken through the

thickness of the base panel around the end of the unbonded length in two of the specimens tested as part of this project, supporting this α_s value.

8.2.6 Anchorage Detailing of E.D. Steel

Due to the large cyclic steel strains expected through Δ_{wm}, Type II mechanical splices specified in Section 21.1.6 of ACI 318 (2011) and permitted by Section 5.4.2 of ACI ITG-5.2 (2009) should not be used for the E.D. bars in hybrid precast walls in seismic regions unless the splices have been tested and validated under cyclic loading up to a steel strain of at least $0.85\varepsilon_{su}$. As discussed in Section 6.3, pullout of the E.D. bars from the foundation occurred in Specimen HW2 due to the failure of the grout within Type II splice connections prior to Δ_{wm} (see Figure 8.4). While the splices satisfied all ACI 318 and AC133 (2010) requirements for Type II mechanical connectors and the grout used inside the splices satisfied the splice manufacturer's specifications, the E.D. bars were subjected to greater strains and over a significantly larger number of cycles than required to classify a Type II connection per ACI 318 and AC133, resulting in the pullout of the bars.

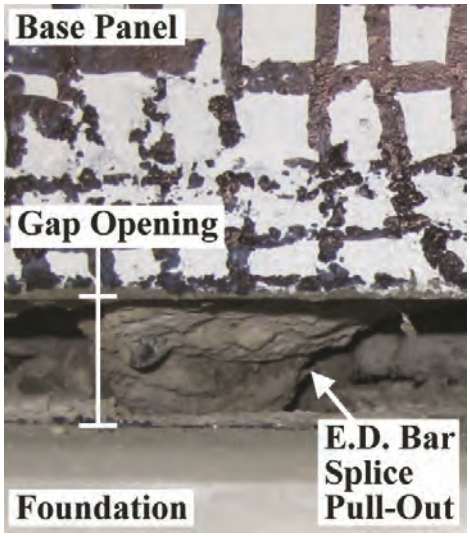

Figure 8.4 E.D. Bar Splice Pullout in Specimen HW2

In validating Type II connectors for use in E.D. bar splices of hybrid precast shear walls, the bars should first be subjected to 20 loading cycles through +0.95ε_{sy} and -0.5ε_{sy}, where ε_{sy}=yield strain of the steel, as required by AC133. Beyond this point, 6 cycles should be applied at each load increment, with the compression strain amplitude kept constant at -0.5ε_{sy} and the tension strain amplitude increased to a value not less than 5/4 times and not more than 3/2 times the strain amplitude from the previous load increment. Testing should continue until the tension strain amplitude reaches or exceeds +0.85ε_{su} over 6 cycles. These requirements would result in similar cyclic loading conditions during the validation testing of the splices as the loading conditions that develop during the validation testing of hybrid shear walls based on ACI ITG-5.1 (2007). The requirement to subject the splices to 6 cycles at each load increment assumes that the E.D. bars will be placed near the wall centerline [as recommended in the Design Procedure Document (Smith and Kurama 2012a)]; and thus, the bars will undergo tensile strains in each of the positive and negative directions of lateral wall displacements.

In lieu of Type II splices, the full development length of the E.D. bars can be cast or grouted (during the construction process) into the base panel and the foundation. This connection technique was successfully used in this project, with no observed pullout of the bars from the concrete.

8.2.7 PT Steel Strain Limitation

The anchorage system for the PT steel tendons should be capable of allowing the strands to reach the predicted stresses and strains at Δ_{wm} without strand wire fracture or wire slip. Unless the PT anchors have been qualified for greater strand strains under cyclic loading, the total maximum strand strains (including prestrain) should be limited to 0.01-cm/cm (0.01-in./in.). As discussed in detail by Walsh and Kurama (2010, 2012), strand wire fractures can occur if the

tendon strains exceed 0.01-cm/cm (0.01-in./in.). With this strain limit, which was used in the design of the specimens tested as part of this project, no strand wire fracture or slip was observed and the tendons remained mostly in the linear-elastic range through Δ_{wm}. Significant nonlinear straining of the PT steel should be prevented to limit the prestress losses at Δ_{wm}.

8.2.8 Flexural Design of Upper Joints

As discussed in Section 3.1.2, the tension steel strain of the mild steel bars crossing the upper panel-to-panel joints should be limited to ε_{sy} (to limit gap opening) and the maximum concrete compressive stress should be limited to $0.5f_c'$ (to keep the concrete linear-elastic). These material limits were used in the design of the wall test specimens, with no undesirable behavior developing in the upper joints. To prevent strain concentrations in the steel, a short prescribed length of the bars [about 10 to 15 cm (4 to 6 in.)] should be unbonded at each joint.

8.2.9 Distributed Reinforcement in Wall Panels

Based on the performance of the specimens tested in this project, the base panel of a hybrid precast shear wall is expected to develop diagonal cracking; and thus, distributed vertical and horizontal reinforcement should be designed following the applicable requirements in Sections 21.9.2 and 21.9.4 of ACI 318 (2011). The specimens satisfied these requirements and developed well distributed hairline cracking in the base panel, as shown in Figure 6.2 (note that the cracks visible in the photographs were highlighted with markers during each test for enhanced viewing). The upper panels of the solid walls developed no cracking; and thus, the distributed reinforcement in these panels can be reduced to satisfy the requirements in Section 16.4.2 of ACI 318.

Section 21.9.6.4(e) of ACI 318 (2011) should be satisfied for the development of the base panel horizontal reinforcement within the confined boundary regions at the wall toes. As shown in Figure 8.3, the horizontal bars in Specimens HW1, HW2, and HW3 were not developed inside the boundary regions, reducing the effectiveness of these bars and causing increased spalling and delamination of the cover concrete at the base (see Figures 6.2 and 8.2.)

8.2.10 Edge Reinforcement in Wall Panels

As required by ACI ITG-5.2, the reinforcement along the bottom edge of the base panel should provide a nominal tensile strength of not less than 87.6-kN per horizontal meter (6000-lbs per horizontal foot) along the length of the panel. The objective of this reinforcement is to control concrete cracking initiating from the bottom of the base panel (Allen and Kurama 2002); and thus, the bars should be placed as close to the bottom of the panel as practically possible, while also satisfying the ACI 318 concrete cover requirements. The bottom edge reinforcement in the wall test specimens was designed using this approach. Strain gauges placed on the bars indicated strains reaching around $0.85\varepsilon_{sy}$ at Δ_{wm}, supporting the design requirement (e.g., see Figure 8.5 for the measured strains in Specimen HW5).

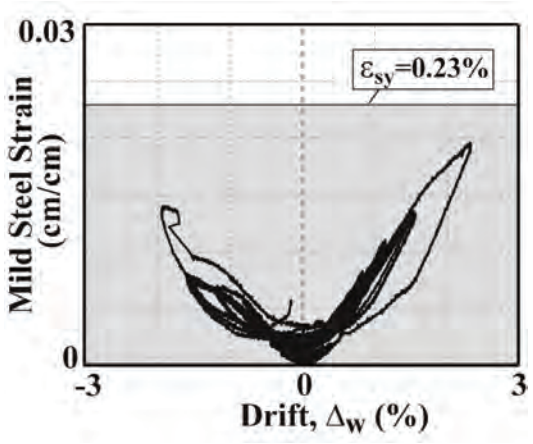

Figure 8.5 Bottom Edge Reinforcement Strains in Specimen HW5

8.2.11 Wall Restoring Force

Hybrid precast walls must maintain an adequate amount of axial restoring force to ensure that the gap at the base joint is fully closed upon removal of the lateral load after tensile yielding of the E.D. bars. This restoring force, which is comprised of the gravity axial force and the total PT force (including losses) at Δ_{wm}, should be greater than $A_s(f_{sm}+f_{sy})$, where A_s=total area of the E.D. steel, f_{sm}=E.D. steel stress at Δ_{wm}, and f_{sy}=yield strength of E.D. steel. This is demonstrated in Figure 8.6, which shows an idealized stress-strain relationship for the E.D. steel. As the wall is displaced from the initial position (close to Point A), the E.D. bars yield in tension (Point B) and reach the maximum strain, ε_{sm} (Point C) at Δ_{wm}. Upon unloading of the wall, the restoring force must be able to yield the tensile E.D. bars back in compression (Point D) and return the bars to essentially zero strain (Point E), resulting in a total force reversal of approximately $A_s(f_{sm}+f_{sy})$ such that no significant plastic tensile strains accumulate in the steel.

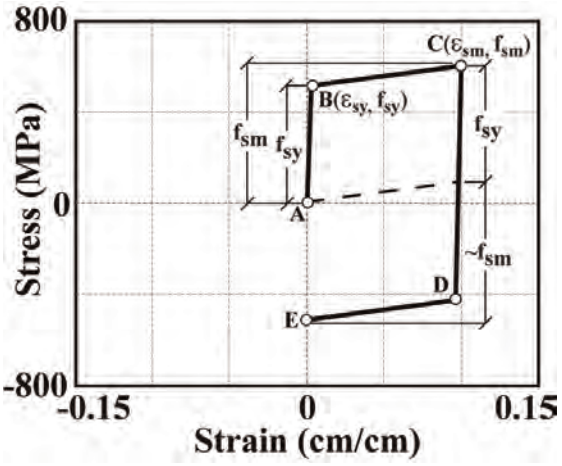

Figure 8.6 Idealized E.D. Steel Stress-Strain Relationship

Specimens HW5 and EW did not satisfy this restoring force requirement, which is more demanding than that recommended in ACI ITG-5.2 (2007). The restoring force in Specimen HW5 was close to the ACI ITG-5.2 limit, but was not sufficient to overcome $A_s(f_{sm}+f_{sy})$.

Failure of this wall occurred suddenly (as discussed in Sections 6.6, 7.7, and 7.8), resulting in the out-of-plane displacements of the wall base and buckling of the E.D. bars (see Figure 8.1). Specimen EW included no PT force; and thus, had an even smaller restoring force. Failure of the wall occurred rapidly (see Sections 6.7, 7.7, and 7.8), leading to excessive in-plane shear slip and localized splitting of the base panel, as shown in Figure 8.7.

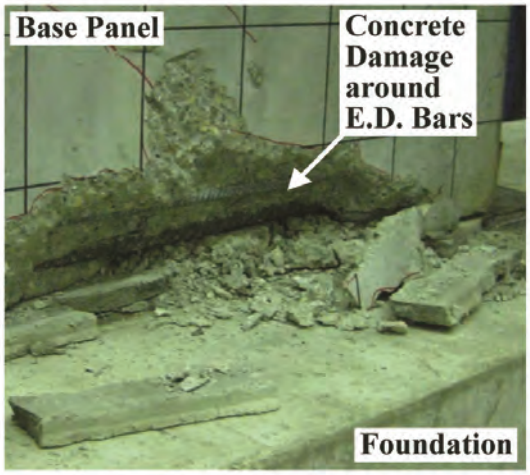

Figure 8.7 Base Panel Damage in Specimen EW

8.2.12 Design of Perforated Wall Panels

The general design philosophy for the panel perforations is to provide an adequate amount of mild steel reinforcement in the vertical and horizontal chords around each perforation such that the presence of the perforations does not negatively affect the performance of the wall through Δ_{wm}. The design approach uses a simplified finite element model as described in the Design Procedure Document (Smith and Kurama 2012a). Based on the observed behavior of the solid and perforated hybrid specimens tested as part of this project, the panel perforations did not significantly affect the global response of the walls (e.g., see the V_b-Δ_w behaviors in Figure 6.3), thus validating the design approach. While the perforations did result in increased shear deformations of the wall panels, reduced energy dissipation, and increased concrete cracking

extending into the upper panel, overall, these effects did not result in any unacceptable behavior. Note that the requirements for coupling beams in Section 21.9.7 of ACI 318 do not apply to the reinforcement around the perforations since the bars placed around the perforations are designed not to yield.

8.3 SUMMARY OF PROPOSED MODIFICATIONS AND ADDITIONS TO ACI ITG-5.2

Tables 8.3 and 8.4 summarize the proposed modifications and additions, respectively, to the design recommendations in ACI ITG-5.2 (2009) based on the results from this project. Full details of these recommendations can be found in the Design Procedure Document (Smith and Kurama 2012a).

Table 8.3 Proposed Modifications to ACI ITG-5.2

ACI ITG-5.2 (2009)		**Design Procedure Document (Smith and Kurama 2012a)**	
Section	**Recommendation**	**Section**	**Recommendation**
Sect. 3.3.2	Energy-dissipating reinforcement shall have the rib deformation heights, yield strength, ultimate elongation, and stress-strain properties required by ASTM A706. Instead of using ASTM A706, reinforcement-specific test data on the stress-strain properties of the energy-dissipating reinforcement shall be obtained before design and construction. In such cases, the tensile strength shall be taken as the specified minimum tensile strength f_{su}. The strain ε_{su} at the tensile strength shall be taken as a strain 0.02 less than the strain at the minimum elongation specified in ASTM A706 for the given bar size. Stress-strain properties of energy-dissipating reinforcement for each bar size used for the wall system shall be obtained from tension tests as specified in ASTM A706. The average strain ε_{su} of reinforcement at its average tensile strength f_{su} shall be obtained. Averages shall be based on the results of a minimum of three tension tests for each bar size for every steel heat used in the wall system.	Sect. 4.4.4	The stress-strain properties of the E.D. steel shall be defined accurately for design. The E.D. reinforcement shall satisfy Section 21.1.5 of ACI 318 (2011). In general, the E.D. steel shall comply with ASTM A706, Grade 60 reinforcement specifications. However, ASTM A615, Grade 60 reinforcement shall be permitted for the E.D. bars if, for all the reinforcement in the precast wall panels and present on the jobsite, "(a) the actual yield strength (i.e., measured yield strength, f_{sy}) based on mill tests does not exceed the specified yield strength (i.e., 60 ksi design yield strength) by more than 18,000 psi; and (b) the ratio of the actual tensile strength (i.e., measured ultimate strength, f_{su}) to the actual yield strength (i.e., measured f_{sy}) is not less than 1.25."
Sect. 3.3.3	Prestressing tendons used to post-tension shear walls shall be unbonded. Calculated strains in prestressing steel shall not exceed 0.01 at Δ_{wd}.	Sect. 4.4.6	Unless the PT anchors have been qualified for greater strand strains under cyclic loading, the total strand strains shall be limited to a maximum of 0.01-in./in. at Δ_{wm}. Significant nonlinear straining of the PT steel shall be prevented to the limit prestress losses at Δ_{wm}.

Sect. 5.3	The minimum prestress force shall be: $A_p f_{pi} + 0.9N_{DL} = A_s f_{su}$ where, $A_s f_{su}$ is the ultimate tensile strength of all the energy-dissipating reinforcement, and N_{DL} is the self-weight of the wall plus any dead loads acting on it, including the self-weight of any components directly attached to the wall. *Note: The minimum prestress force, $A_p f_{pi}$, shall include allowances for all prestress losses.*	Sect. 4.8.1	The following equation shall be satisfied to provide an adequate amount of axial restoring force through the maximum-level drift, Δ_{wm}: $\phi_r[A_p(f_{pm} - 0.5f_{p,loss}) + N_w] > A_s(f_{sm} + f_{sy})$ *Note: The variables used in this equation are defined in the Design Procedure Document (Smith and Kurama 2012a).*
Sect. 5.4.1	The energy-dissipating reinforcement provided at the base of the wall shall provide at least 25% of the nominal flexural strength of the wall at the wall-foundation interface.	Sect. 4.4.1	The κ_d ratio used in design shall not exceed 0.80 (to ensure sufficient self-centering) and shall not be less than 0.50 (to ensure sufficient energy dissipation). *Note: The required minimum κ_d ratio of 0.50 corresponds to a minimum 33% of the nominal flexural strength of the wall at the base joint to be provided by the E.D. steel. This lower κ_d limit was determined based on the measured behavior of a perforated wall. It may be possible to use a reduced value for the lower κ_d limit of solid walls.*
Sect. 5.4.2	The energy-dissipating reinforcement shall be anchored by: (1) being cast into the concrete of the foundation or wall panel during the placement of that concrete; (2) being grouted in ducts positioned in the foundation or wall panel prior to the placement of the concrete for those members; or (3) use of a Type II splice that connects energy-dissipating reinforcement cast separately in the wall panel and the foundation.	Sect. 4.4.5	Type II mechanical splices specified in Section 21.1.6 of ACI 318 (2011) shall not be used for the E.D. bars unless the splices have been tested and validated under cyclic loading up to a steel strain of at least $0.85\varepsilon_{su}$. In lieu of using Type II mechanical splices, the full development length of the E.D. bars shall be cast or grouted (during the construction process) into the wall panels and the foundation.
Sect. 5.6.3.2	The value of α_s shall not be taken as greater than 5.5 nor less than 2.0.	Sect. 4.4.4	The coefficient used to estimate the additional debonded length of the bars shall be assumed as α_s=0 and α_s=2.0 at Δ_{wd} anΔ_{wm}d, respectively.
Sect. 5.6.3.3	At M_{wm}, the E.D. steel strains shall be not greater than $0.85\varepsilon_{su}$.	Sect. 4.4.4	The E.D. steel strains, ε_{sm} shall be greater than $0.5\varepsilon_{su}$ to ensure sufficient energy dissipation but not exceed $0.85\varepsilon_{su}$ to prevent bar fracture.

Table 8.4 Proposed Additions to ACI ITG-5.2

Design Procedure Document (Smith and Kurama 2012a)	
Section	**Recommendation**
Sect. 4.4.3	The confined concrete region at the wall toes shall extend vertically over a height of the base panel not less than the plastic hinge height, h_p.
Sect. 4.4.3	The first hoop shall be placed at a distance from the bottom of the base panel no greater than the minimum concrete cover required by ACI 318 (2011). Additionally, for rectangular confinement hoops, the length-to-width aspect ratio of the hoop (measured center-to-center of bar) shall not exceed 2.50. In general, crossties not engaging the hoop steel shall be considered ineffective in providing confinement to the concrete.
Sect. 4.4.3	The design 28-day compressive strength of the grout shall be within ±20% of the design 28-day strength of the unconfined concrete in the base panel to provide a matching bearing bed for the wall. The placement of the grout at each joint shall be completed in a single application. The E.D. bars and PT tendons shall be isolated from the grout so that the deformations of the steel do not deteriorate the integrity of the grout pad.
Sect. 4.4.5	The development length of bars cast inside the concrete shall be designed according to Section 21.9.2.3(c) of ACI 318.

Sect. 4.5	For the flexural design of the upper panel-to-panel joints, the tension steel stress, $f_{s,u}$ shall be limited to f_{sy} (to limit gap opening) and the maximum concrete compressive stress, $f_{c,u}$ shall be limited to $0.5f_c'$ (to keep the concrete linear elastic). The upper joint reinforcement shall be symmetric at both ends of the wall and be placed as close to the panel edges as possible with adequate concrete cover. To prevent strain concentrations in the steel, a short prescribed length of the bars (approximately 4 to 6 in.) shall be unbonded at each joint.
Sect. 4.7.1	The distributed reinforcement in the base panel shall be designed following the applicable requirements in Sections 21.9.2 and 21.9.4 of ACI 318. In addition, the requirements in Section 21.9.6.4(e) of ACI 318 shall be satisfied for the development of the wall horizontal reinforcement in the confined boundary regions at the wall toes. The distributed reinforcement in the upper panels shall be permitted to be reduced following the requirements in Section 16.4.2 of ACI 318.

8.4 PROPOSED MODIFICATION TO ACI ITG-5.1

For the test specimens that satisfied the restoring force requirement in Section 8.2.10 (Specimens HW1, HW2, HW3, and HW4), only a small amount of horizontal shear slip occurred along the base joint. As shown in Figure 7.10, in some instances, base slip of up to 0.38 cm (0.15 in.) was measured, exceeding the allowable limit of 0.15 cm (0.06 in.) per Section 7.1.4(3) of ACI-ITG-5.1. However, this slip did not result in any undesirable behavior of the structures. Therefore, the shear slip limit in ACI-ITG-5.1 can be increased to 0.38 cm (0.15 in.) without affecting the wall performance. This proposed modification is summarized in Table 8.5.

Table 8.5 Proposed Modification to ACI ITG-5.1

ACI ITG-5.1 (2007) Section 7.1.4(3)	Proposed Modification
The maximum relative displacement between the base of a wall and the adjacent foundation (shear slip) and the maximum relative displacement along the horizontal joints between precast panels over the height of the wall shall not exceed 0.06-in. (1.5-mm).	The maximum relative displacement between the base of a wall and the adjacent foundation (shear slip) and the maximum relative displacement along the horizontal joints between precast panels over the height of the wall shall not exceed 0.15-in. (3.8-mm).

CHAPTER 9

POST-EARTHQUAKE EVALUATION AND REPAIR OF HYBRID WALLS

The post-earthquake evaluation and subsequent repair of hybrid precast concrete shear walls are important aspects to the practical implementation of this new type of structural system in seismic regions. After a large earthquake, the damage in a well-designed hybrid wall should be limited to E.D. bar yielding, minor concrete cracking, and cover spalling at the toes of the base panel. The damage to the concrete can be addressed through localized repairs, such as epoxy crack injections or local concrete and grout patches.

The PT tendons and anchorages should not sustain any significant damage, as the steel is designed to remain mostly linear-elastic under the maximum considered earthquake (MCE). Nevertheless, the PT steel should be inspected at the anchorage locations. Any observed damage to the PT tendons or anchors (e.g., strand wire fracture or slip) can be addressed by individually removing and replacing the damaged strands, tendons, and anchorages.

Assessing the extent of yield or possible fracture of the E.D. steel is a more difficult task. If the inspecting engineer has reason to believe that excessive yielding or fracture has occurred to the E.D. bars, it may be challenging to locally remove and replace these bars within the base panel and foundation. In lieu of replacement, extra E.D. bars can be placed but not anchored during the original construction of the wall (e.g., by placing the bars inside ungrouted oversized ducts cast within the foundation or the base panel). If the need for E.D. bar replacement arises, the damaged bars can be locally cut along the base-panel-to-foundation joint (thereby fully eliminating their contribution to the lateral strength of the wall) and the “replacement” bars can be grouted inside the ducts essentially activating these bars to contribute to the lateral strength of the structure.

Note that post-earthquake inspection and repair of hybrid precast concrete shear walls was outside of the scope of this research project; and thus, none of the above recommendations has been validated experimentally.

CHAPTER 10

SUMMARY AND CONCLUSIONS

The broad objective of this research project was to advance innovations in building design and construction by validating the classification of hybrid precast concrete walls as "special" reinforced concrete shear walls according to ACI 318 (2011). To accomplish this objective, the project conducted experimental, analytical, and design studies for the new system based on the requirements and guidelines prescribed in ACI ITG-5.1 (2007). The specific research objectives were to develop: (1) a high-performance precast concrete seismic shear wall system with practical construction details; (2) a validated, practical seismic design procedure for the new system described in a Design Procedure Document (Smith and Kurama 2012a); (3) validated, practical analytical models and design tools that can accurately predict performance; (4) sufficient experimental and analytical evidence demonstrating the classification of the structure as a "special" reinforced concrete shear wall system per ACI 318; and (5) practical seismic application and detailing guidelines and recommendations.

The research provided new information in accordance with and directly addressing the ACI ITG-5.1 requirements as well as information regarding the behavior of hybrid precast walls featuring multiple wall panels (i.e., multiple horizontal joints) and panel perforations, both common features in building construction. The experimental results demonstrated that properly designed and detailed hybrid walls can satisfy all requirements for special reinforced concrete shear walls in seismic regions while also revealing important considerations to prevent undesirable failure mechanisms. The following observations and conclusions were made based on the project:

- The hybrid wall test specimens demonstrated capability for full re-centering while also providing considerable energy dissipation due to the combination of unbonded post-tensioning (PT) steel with yielding mild energy dissipating (E.D.) steel reinforcement across the horizontal base-panel-to-foundation joint.
- Damage to the solid hybrid walls was limited to the base panel, consisting of the yielding of the E.D. bars, crushing of the concrete at the wall toes, and minor cracking.
- The use of ACI 318 (2011) Type II splice connectors for the E.D. bars is not recommended for seismic regions. In comparison, hybrid walls with fully-developed E.D. bars through grouted connections into the foundation were able to sustain the prescribed lateral drift demands.
- For the concrete confinement to be effective, the first hoop at the wall toes should be placed as close to the bottom of the base panel as permitted by the cover requirements of ACI 318. Furthermore, the length/width aspect ratio of the hoops should be limited and crossties not directly engaging the hoop steel should not be considered as an effective component of the confinement reinforcement.
- The horizontal distributed panel reinforcement should be embedded into the confinement regions at the toes of the base panel to maintain the effectiveness of these bars and minimize the extent of the concrete damage (i.e., concrete cracking, and cover concrete spalling and delamination).
- As a result of the added mild steel reinforcement in the horizontal and vertical chords, the panel perforations did not negatively affect the global lateral load behavior of the perforated wall test specimens.
- The damage to the perforated specimens was mostly concentrated in the base panel, consisting of E.D. bar yielding, concrete crushing at the wall toes, and distributed

cracking in the horizontal chords and vertical chords (predominantly the central chord) around the perforations. Minor concrete cracking extended into the upper panel, primarily at the corners of the perforations.

- While the emulative precast wall test specimen demonstrated increased energy dissipation, the lack of post-tensioning resulted in unsatisfactory re-centering, leading to excessive uplift, horizontal slip, and lateral strength and stiffness degradation. These walls are not recommended for high seismic regions unless a reliable amount of tributary gravity load exists to fully close the gap at the base.
- The ratio of the PT steel to E.D. steel area is a very important design property in hybrid walls. Undesirable behavior similar to the emulative wall that was tested can occur in hybrid walls if the axial restoring force from the PT steel and gravity load is not sufficient to fully close the gap at the base.
- The analytical modeling tools, which incorporated simplifying assumptions appropriate for the design office, provided a reasonable match to the experimental data. These models should aid in the seismic design of hybrid precast concrete shear walls including walls with panel perforations.

Utilizing the experimental data, the project developed: (1) a validated seismic design procedure, summarized within a Design Procedure Document (Smith and Kurama 2012a), to achieve the desired behavior from hybrid precast walls; (2) validated analytical models and design tools that can accurately predict performance; and (3) practical application guidelines and recommendations. The Design Procedure Document also provides a validation for, and where necessary, recommended changes and additions to the applicable requirements and guidelines in ACI ITG-5.2 (2009). Ultimately, these project deliverables empower precast producers and design engineers to adopt hybrid wall structures as special reinforced concrete shear walls in

moderate and high seismic regions of the U.S., without the need to carry out additional approval studies.

REFERENCES

1. ACI. (2007). “ACI ITG-5.1-07 Acceptance Criteria for Special Unbonded Post-Tensioned Precast Structural Walls Based on Validation Testing and Commentary.” ACI Innovation Task Group 5.

2. ACI. (2009). “ACI ITG-5.2-09 Design of a Special Unbonded Post-Tensioned Precast Shear Wall Satisfying ACI ITG-5.1 Requirements.” ACI Innovation Task Group 5.

3. ACI. (2011). “ACI 318-11 Building Code Requirements for Structural Concrete (ACI 318-11) and Commentary.” ACI Committee 318.

4. Ajrab, J., Pekcan, G., and Mander, J. (2004). “Rocking Wall-Frame Structures with Supplemental Tendon Systems.” *ASCE Journal of Structural Engineering*, 130(6), 895-903.

5. Allen, M. and Kurama, Y. (2002). “Design of Rectangular Openings in Precast Walls Under Combined Vertical and Lateral Loads.” *PCI Journal*, 47(2), 58-83.

6. ANSYS, Inc. (2009). “ANSYS LS-DYNA User's Guide.” ANSYS, Inc.

7. ASCE. (2010). “Minimum Design Loads for Buildings and Other Structures.” ASCE/SEI 7-10.

8. Corr, D., Accardi, M., Graham-Brady, L., and Shah, S. (2007). “Digital Image Correlation Analysis of Interfacial Debonding Properties and Fracture Behavior in Concrete.” *Engineering Fracture Mechanics*, 74(1-2), 109-121.

9. CSI. (2008). “CSI Analysis Reference Manual for SAP2000, ETABS, and SAFE.” Computer and Structures, Inc.

10. Fleischman, R., Naito, C., Restrepo, J., Sause, R., Ghosh, S., Wan, G., Schoettler, M., and Cao, L. (2005a). “Precast Diaphragm Seismic Design Methodology (DSDM) Project, Part 2: Research Program.” *PCI Journal*, 50(6), 14-31.

11. Fleischman, R., Naito, C., Restrepo, J., Sause, R., and Ghosh, S. (2005b). “Precast Diaphragm Seismic Design Methodology (DSDM) Project, Part 1: Design Philosophy and Research Approach.” *PCI Journal*, 50(5), 68-83.

12. Hibbitt, Karlsson, and Sorenson. (2009). “ABAQUS User's Manual - Version 6.9.” Hibbitt, Karlsson & Sorenson, Inc.

13. Holden, T., Restrepo, J., and Mander, J. (2001). “A Comparison of the Seismic Performance of Precast Wall Construction: Emulation and Hybrid Approaches.” University of Canterbury, Research Report 2001-4.

14. Holden, T., Restrepo, J., and Mander, J. (2003). “Seismic Performance of Precast Reinforced and Prestressed Concrete Walls.” *ASCE Journal of Structural Engineering*, 129(3), 286-297.

15. ICBO. (1997). “Uniform Building Code, Volume 2: Structural Engineering Design Provisions.” International Conference of Building Officials.

16. ICC. (2010). “AC133: Acceptance Criteria for Mechanical Connector Systems for Steel Reinforcing Bars.” ICC Evaluation Services.

17. Kurama, Y. (2000). “Seismic Design of Unbonded Post Tensioned Precast Walls with Supplemental Viscous Damping.” *ACI Structural Journal*, 97(4), 648-658.

18. Kurama, Y. (2001). “Simplified Seismic Design Approach for Friction Damped Unbonded Post Tensioned Precast Walls.” *ACI Structural Journal*, 98(5), 705-716.

19. Kurama, Y. (2002). “Hybrid Post-Tensioned Precast Concrete Walls for Use in Seismic Regions.” *PCI Journal*, 47(5), 36-59.

20. Kurama, Y. (2005). “Seismic Design of Partially Post-Tensioned Precast Concrete Walls.” *PCI Journal*, 50(4), 100-125.

21. Kurama, Y., Pessiki, S., Sause, R., and Lu, L.W. (1999a). “Seismic Behavior and Design of Unbonded Post-Tensioned Precast Concrete Walls.” *PCI Journal*, 44(3), 72-89.

22. Kurama, Y., Sause, R., Pessiki, S., and Lu, L.W. (1999b). “Lateral Load Behavior and Seismic Design of Unbonded Post-Tensioned Precast Concrete Walls.” *ACI Structural Journal*, 96(4), 622-632.

23. Kurama, Y., Sause, R., Pessiki, S., and Lu, L.W. (2002). “Seismic Response Evaluation of Unbonded Post-Tensioned Precast Walls.” *ACI Structural Journal*, 99(5), 641-651.

24. Mackertich, S., and Aswad, A. (1997). “Lateral Deformations of Perforated Shear Walls for Low and Mid-Rise Buildings.” *PCI Journal*, 42(1), 30-41.

25. Mander, J., Priestley, M., and Park, R. (1988). “Theoretical Stress-Strain Model for Confined Concrete.” *ASCE Journal of Structural Engineering*, 114(8), 1804-1826.

26. Mazzoni, S., McKenna, F., Scott, M., and Fenves G. (2007). “OpenSees Command Language Manual.” University of California, Berkeley.

27. McGinnis, M., Pessiki, S., and Turker, H. (2005). “Application of 3D Digital Image Correlation to the Core-Drilling Method.” *Experimental Mechanics*, 45(4), 359-367.

28. McGinnis, M., Smith, B., Holloman, M., Lisk, M., Kurama, Y., and O’Donnell, A. (2012). “3-D Digital Image Correlation: An Underused Asset for Structural Testing.” *Proceedings of the 2012 ASCE Structures Congress*, Chicago, IL.

29. Nagae, T., Tahara, K., Matsumori, T., Shiohara, H., Kabeyasawa, T., Kono, S., Nishiyama, M., Wallace, J., Ghannoum, W., Moehle, J., Sause, R., Keller, W., and Tuna, Z. (2011). "Design and Instrumentation of 2010 E-Defense Four-Story Reinforced Concrete and Post-Tensioned Concrete Buildings." University of California, Berkeley, Pacific Earthquake Engineering Research Center (PEER) Report 2011/103.

30. Oesterle, R., Fiorato, A., Johal, L., Carpenter, J., Russell, H., and Corley, W. (1976). "Earthquake Resistant Structural Walls – Tests of Isolated Walls." Portland Cement Association, Research and Development Report 1571, 24-27.

31. Orteu, J. (2009). "3-D Computer Vision in Experimental Mechanics." *Optics and Lasers in Engineering*, 47(3-4), 282-291.

32. Perez, F., Pessiki, S., Sause, R., and Lu, L.W. (2003). "Lateral Load Tests of Unbonded Post-Tensioned Precast Concrete Walls in Large-Scale Structural Testing." *ACI Special Publication*, SP-211.

33. Perez, F., Pessiki, S., and Sause, R. (2004a). "Seismic Design of Unbonded Post-Tensioned Precast Concrete Walls with Vertical Joint Connectors." *PCI Journal*, 49(1), 58-79.

34. Perez, F., Pessiki, S., and Sause, R. (2004b). "Lateral Load Behavior of Unbonded Post-Tensioned Precast Concrete Walls with Vertical Joints." *PCI Journal*, 49(2), 48-64.

35. Perez, F. J., Sause, R., and Pessiki, S. (2007). "Analytical and Experimental Lateral Load Behavior of Unbonded Post-Tensioned Precast Concrete Walls." *ASCE Journal of Structural Engineering*, 133(11), 1531-1540.

36. Prakash, V., Powell, G., and Campbell, S. (1993). "DRAIN-2DX Base Program Description and User Guide; Version 1.10." University of California, Berkeley, Research Report UCB/SEMM-93/17.

37. Priestley, M., Sritharan, S., Conley, J., and Pampanin, S. (1999). "Preliminary Results and Conclusions from the PRESSS Five-Story Precast Concrete Test Building." *PCI Journal*, 44(6), 42-67.

38. Rahman, A. and Restrepo, J. (2000). "Earthquake Resistant Precast Concrete Buildings: Seismic Performance of Cantilever Walls Prestressed Using Unbonded Tendon." University of Canterbury, Research Report 2000-5.

39. Restrepo, J. (2003). "Self-Centering Precast Post-Tensioned Cantilever Walls – Theory and Experimental Work." *Proceeding of the 2003 ASCE Structures Congress*, Seattle, WA.

40. Smith, B., and Kurama, Y. (2009). "Design of Hybrid Precast Concrete Walls for Seismic Regions." *Proceedings of the 2009 ASCE Structures Congress*, Austin, TX.

41. Smith, B., and Kurama, Y. (2010a). "Analytical Model Validation of a Hybrid Precast Concrete Wall for Seismic Regions." *Proceedings of the 2010 ASCE Structures Congress*, Orlando, FL.

42. Smith, B., and Kurama, Y. (2010b). "Seismic Behavior of a Hybrid Precast Concrete Wall Specimen: Measured Response versus Design Predictions." *Proceedings of the 9th U.S. National and 10th Canadian Conference on Earthquake Engineering*, Toronto, ON, Canada.

43. Smith, B., and Kurama, Y. (2012a). "Seismic Design Guidelines for Special Hybrid Precast Concrete Shear Walls." University of Notre Dame, Research Report No. NDSE-2012-02, June, Notre Dame, IN.

44. Smith, B., and Kurama, Y. (2012b). "Validated Seismic Design Guidelines for Solid and Perforated Hybrid Precast Shear Walls." *Proceedings of the 2012 PCI Annual Convention and Exhibition*, Nashville, TN.

45. Smith, B., McGinnis, M., and Kurama, Y. (2010). "Full-Field Lateral Response Investigation of Hybrid Precast Concrete Shear Walls." *Proceedings of the 3rd International Congress and fib Exhibition Incorporating the PCI Annual Convention and Bridge Conference*, Washington D.C.

46. Smith, B., Kurama, Y., and McGinnis, M. (2011a). "Comparison of Hybrid and Emulative Precast Concrete Shear Walls for Seismic Regions." *Proceedings of the 2011 ASCE Structures Congress*, Las Vegas, NV.

47. Smith, B., Kurama, Y., and McGinnis, M. (2011b). "Design and Measured Behavior of a Hybrid Precast Concrete Wall Specimen for Seismic Regions." *ASCE Journal of Structural Engineering*, 137(10), 1052-1062.

48. Smith, B., Kurama, Y., and McGinnis, M. (2011c). "Design and Measured Behavior of a Perforated Hybrid Precast Concrete Shear Wall for Seismic Regions." *Proceeding of the 2011 PCI Annual Convention and Exhibition,* Salt Lake City, UT.

49. Smith, B., Kurama, Y., and McGinnis, M. (2012a). "Behavior of Precast Concrete Shear Walls for Seismic Regions: Comparison of Hybrid and Emulative Specimens." *ASCE Journal of Structural Engineering, In-Review*.

50. Smith, B., Kurama, Y., and McGinnis, M. (2012b). "Comparison of Solid and Perforated Precast Concrete Shear Walls for Seismic Regions." *Proceeding of the 2012 ASCE Structures Congress*, Chicago, IL.

51. Smith, B., Kurama, Y., and McGinnis, M. (2012c). "Hybrid Precast Concrete Shear Walls for Seismic Regions: Solid and Perforated Walls." *Proceedings of the 9th International Conference on Urban Earthquake Engineering and 4th Asia Conference on Earthquake Engineering*, Tokyo, Japan.

52. Walsh, K. and Kurama, Y. (2010). “Behavior of Unbonded Post-Tensioning Monostrand Anchorage Systems Under Monotonic Tensile Loading.” *PCI Journal*, 55(1), 97-117.

53. Walsh, K. and Kurama, Y. (2012). “Effects of Loading Conditions on the Behavior of Unbonded Post-Tensioning Strand-Anchorage Systems.” *PCI Journal*, 57(1), 76-96.